LIÈGE université Library

https://lib.uliege.be https://matheo.uliege.be

Master thesis : Computational Analysis of Lidocaine-Induced Modulations on the Excitability of Two Heterogeneous DRG Neuron States Connected to a Projection Neuron (including introduction to research methodology)

Auteur : Pagano, Thomas
Promoteur(s) : Sacré, Pierre; Drion, Guillaume
Faculté : Faculté des Sciences appliquées
Diplôme : Master en ingénieur civil biomédical, à finalité spécialisée
Année académique : 2025-2026
URI/URL : http://hdl.handle.net/2268.2/27040

Avertissement à l'attention des usagers :

Tous les documents placés en accès ouvert sur le site le site MatheO sont protégés par le droit d'auteur. Conformément aux principes énoncés par la "Budapest Open Access Initiative"(BOAI, 2002), l'utilisateur du site peut lire, télécharger, copier, transmettre, imprimer, chercher ou faire un lien vers le texte intégral de ces documents, les disséquer pour les indexer, s'en servir de données pour un logiciel, ou s'en servir à toute autre fin légale (ou prévue par la réglementation relative au droit d'auteur). Toute utilisation du document à des fins commerciales est strictement interdite.

Par ailleurs, l'utilisateur s'engage à respecter les droits moraux de l'auteur, principalement le droit à l'intégrité de l'oeuvre et le droit de paternité et ce dans toute utilisation que l'utilisateur entreprend. Ainsi, à titre d'exemple, lorsqu'il reproduira un document par extrait ou dans son intégralité, l'utilisateur citera de manière complète les sources telles que mentionnées ci-dessus. Toute utilisation non explicitement autorisée ci-avant (telle que par exemple, la modification du document ou son résumé) nécessite l'autorisation préalable et expresse des auteurs ou de leurs ayants droit.

UNIVERSITE DE LIEGE
FACULTE DES SCIENCES APPLIQUEES

Computational Analysis of Lidocaine-Induced Modulations on the Excitability of Two Heterogeneous DRG Neuron States Connected to a Projection Neuron

Pagano Thomas

Thesis presented to obtain the degree of :
Master of Science in Biomedical Engineering

Thesis supervisors:
Drion Guillaume
Sacré Pierre

Academic year: **2025 - 2026**

Abstract

Neuronal excitability is a neuron's ability to respond to a stimulus by generating an electrical signal known as an action potential. These electrical pulses form the foundation of neuronal communication, with the information encoded in pulse trains depending on both their frequency and duration. Hyperexcitability is a specific state in which a neuron responds abnormally to weak stimuli, exaggerates its responses, or exhibits spontaneous firing.

Pain serves as the body's warning system, triggering an unpleasant sensation that draws attention to harmful stimuli. These stimuli may involve acute threats, such as intense heat or high pressure capable of causing tissue damage, or minor contact with an existing injury to safeguard the healing process. This latter scenario occurs through sensitization, a phenomenon that affects both the peripheral nervous system (at the level of the dorsal root ganglion) and the central nervous system (at the level of the dorsal horn) by inducing neuronal hyperexcitability as an adaptive response to a vulnerable injury site.

Pathological states arise when sensitization occurs without a functional trigger, generating false alarms that offer no protective benefit. To manage these unwanted pain sensations, modulating the system to reverse, or at least attenuate, the underlying hyperexcitability represents a promising therapeutic approach. Crucially, because this state can severely impact patients in their daily lives, treatments must effectively alleviate chronic discomfort while preserving everyday sensory function, such as normal touch and the vital ability to feel acute, protective pain.

The primary focus of this work is the analysis of distinct pharmacological modulations aimed at treating both peripheral and central sensitization, with particular emphasis on how peripheral modulation influences central neuronal responses, a framework demonstrated through the application of lidocaine as a representative therapeutic agent.

To do so, this thesis investigates the effects of lidocaine in treating hyperexcitability by targeting two primary mediators of sensitization: voltage-gated sodium channels, which play a key role in peripheral neuronal excitability, and NMDA receptors, which serve as key mediators of central sensitization. To achieve this, a conductance-based model is implemented, featuring a dorsal root ganglion neuron connected to a dorsal horn neuron. The dorsal root ganglion neuron incorporates two parameter sets corresponding to healthy and hyperexcitable states, each characterized by distinct profiles of voltage-gated sodium channels. The various types of modulations induced by lidocaine are first simulated individually and then in combination on the peripheral neuron, allowing for an evaluation of their indirect consequences on the postsynaptic dorsal horn neuron. Finally, lidocaine's modulation of NMDA receptors in the central neuron is evaluated, culminating in an assessment of combined peripheral and central modulations. This work also introduces a visual methodology to illustrate drug mechanisms, representing a pharmacological agent as a trajectory across a modulation space.

Acknowledgments

Firstly, I would like to express my sincere gratitude to my supervisors, Professor Guillaume Drion and Professor Pierre Sacré, for their guidance and expertise during this work.

Secondly, I would like to extend a huge thank-you to Anaëlle De Worm for her availability, supervision, and kindness throughout the year.

Thirdly, I would like to express special thanks to Haiyin, Matteo, Océane, and Florian, who took the time to proofread, and to Bart for his unwavering support and company throughout the writing process.

Finally, I am deeply grateful to my family for supporting me, and to my friends for their help, encouragement, and the precious moments we shared throughout my studies.

Liège, 20th August 2026

Thomas Pagano

Contents

1 Introduction **1**
1.1 Motivations . . . 1
1.2 Structure . . . 2

I Background **3**

2 Electrophysiology **4**
2.1 The electrical signaling of the nervous system . . . 4
2.1.1 The neuron . . . 4
2.1.2 The ion channels . . . 5
2.1.3 The generation of the action potential . . . 7
2.2 Modeling of a neuron: the conductance-based model . . . 8
2.2.1 Electrical Equivalent Circuit . . . 8
2.2.2 The Ionic Currents . . . 9

3 Pain Processing and Management **12**
3.1 Pain Processing . . . 12
3.1.1 Definition of pain . . . 12
3.1.2 The pain pathway . . . 14
3.1.3 Sensitization . . . 16
3.2 Potential targets to reduce pain . . . 17
3.2.1 Voltage-gated sodium channels . . . 17
3.2.2 Synaptic receptors . . . 19
3.3 Degeneracy . . . 20
3.3.1 Definition . . . 20
3.3.2 The impact of degeneracy in therapy . . . 22
3.4 Lidocaine . . . 23
3.4.1 Mechanism of action . . . 23
3.4.2 Effect on voltage-gated sodium channels . . . 24
3.4.3 Effect on NMDA receptors . . . 25

II Computational model **26**

4 Model of a DRG neuron connected to a projection neuron **27**
4.1 The first component: the dorsal root ganglion neuron . . . 27
4.1.1 The context of the model . . . 27
4.1.2 Considered ion channels . . . 27
4.1.3 Two sets of parameters . . . 29

4.1.4 Simulation example . . . 30
4.2 The second component: the projection neuron . . . 30
4.2.1 Considered ion channels . . . 30
4.2.2 Calcium dynamics . . . 32
4.2.3 Simulation example . . . 33
4.3 The third component: the synapse . . . 33
4.3.1 AMPAR and NMDAR response . . . 33
4.3.2 Distinction between AMPAR and NMDAR . . . 34
4.3.3 Connection with the projection neuron . . . 34
4.3.4 Simulation example . . . 35
4.4 Experimental protocol . . . 35
4.4.1 Highlighted lidocaine effect . . . 36
4.4.2 Typical simulation . . . 37

III Computational experiments 38

5 Unmodulated model analyses 39
5.1 The role of NaV channels in the DRG neuron . . . 39
5.1.1 Initiation of the first spike . . . 39
5.1.2 Initiation of spiking . . . 41
5.2 The role of synaptic receptors in the response of the projection neuron . . . 44
5.2.1 Projection neuron in stand-alone . . . 44
5.2.2 The response to a single afferent spike . . . 44
5.2.3 The response to afferent spiking . . . 45

6 Impact of NaV channel modulations on excitability 48
6.1 Modulations in DIV0 context . . . 48
6.1.1 The impact of NaV1.7 loss . . . 48
6.1.2 Impact of modulations of NaV1.8 on the rheobase . . . 49
6.1.3 Impact of NaV1.8 modulations on spiking presence and related firing frequency . . . 50
6.1.4 The combination of lidocaine-induced modulations on NaV1.8 . . . 52
6.2 Impact of DIV4–7 channel modulations on rheobase . . . 54
6.2.1 The negligible contribution of NaV1.8 . . . 54
6.2.2 Impact of NaV1.3 modulation . . . 54
6.2.3 Impact of NaV1.7 modulation . . . 55
6.2.4 Combined effect . . . 56
6.3 Indirect impact of the modulation on projection neuron . . . 57
6.3.1 Afferent frequency in case of a spiking pattern . . . 57
6.3.2 Responses to afferent transient versus sustained spiking patterns . . . 59

7 Effect of NMDA receptor inhibition 60
7.1 NMDAR inhibition alone . . . 60
7.2 Combination with NaV1.8 modulation . . . 62
7.2.1 Functional combination with NaV1.8 inhibition during afferent spiking . . . 62
7.2.2 NMDAR inhibition reduces response bursts . . . 63

IV Synthesis and Outlook **64**

8 Discussion, Limitations, and Perspectives **65**
8.1 Discussion . . . 65
8.1.1 Excitability differences between DIV0 and DIV4–7 . . . 65
8.1.2 Contribution of the different NaV modulations . . . 66
8.1.3 The impact of the afferent firing pattern on the postsynaptic response . . . 67
8.1.4 Contribution of NMDAR inhibition . . . 68
8.2 Limitations . . . 69
8.2.1 The omitted modulations . . . 69
8.2.2 The complexity of quantifying drug effects . . . 69
8.2.3 A qualitative study . . . 69
8.3 Perspective . . . 69
8.3.1 Exploring other combinations of VGSCs . . . 69
8.3.2 Adding other modulations . . . 69
8.3.3 Constructing several multi-drug trajectories and evaluating their potential combinations . . . 70
8.3.4 Bifurcation and bistability analyses . . . 70

9 Conclusions **71**

V Appendix **72**

10 Appendix **73**
10.1 Dorsal root ganglion neuron model . . . 73
10.2 Projection neuron model . . . 75
10.3 Synapse . . . 78
10.4 Lidocaine . . . 80
10.5 Numerical tools . . . 81
10.5.1 Solver . . . 81
10.5.2 Spike detection . . . 81
10.5.3 Instantaneous frequency and global frequency . . . 81
10.5.4 Pattern distinction . . . 81

References **83**

List of Abbreviations

AMPAR AMPA Receptor

DHN Dorsal Horn Neuron

DRG Dorsal Root Ganglion

DRGN DRG Neuron

DIV0 DRG neurons that were evaluated after 0 Days In Vitro

DIV4-7 DRG neurons that were evaluated after 4-7 Days In Vitro

IASP International Association for the Study of Pain

NMDAR NMDA Receptor

PrjN Projection Neuron

TTX Tetrodotoxin

TTX-S TTX-sensitive

TTX-R TTX-resistant

VGCC Voltage-Gated Calcium Channel

VGKC Voltage-Gated Potassium Channel

VGSC Voltage-Gated Sodium Channel

WDR Wide Dynamic Range

Chapter 1

Introduction

1.1 Motivations

Pain is a universal experience; although unpleasant, it serves as an essential alarm system that protects the body from harm and facilitates healing. In pathological cases, however, this system can generate false alarms, resulting in persistent discomfort that offers no protective value. While the precise origins of these unwanted pains are sometimes unknown, they are consistently linked to a phenomenon within the pain pathway known as sensitization. Occurring in both the peripheral and central nervous systems, sensitization involves complex, interacting mechanisms that ultimately render neurons hyperexcitable.

This hyperexcitability heightens neuronal sensitivity, causing affected neurons to generate stronger responses to weaker stimuli. However, this state is not inherently pathological; in most cases, it is an adaptive response to protect a vulnerable area following an injury. Nevertheless, modulating this hyperexcitability offers a promising therapeutic strategy for individuals suffering from unwanted pain. Furthermore, targeting these mechanisms expands fundamental understanding of this neuronal state and of sensitization more broadly.

This thesis explores how drug-induced modulations alter neuronal excitability to suppress hyperexcitability. Specifically, it investigates the effects of lidocaine on voltage-gated sodium channels and NMDA receptors, two key elements of nociceptive signaling. Methodologically, this work uses a conductance-based model representing a simplified, two-neuron network, allowing for the direct study of modulatory impacts on an individual neuron and their cascading effects on the connected one.

More specifically, this study contains:

- An evaluation of individual lidocaine effects on voltage-gated sodium channels and their impact on excitability across two distinct DRG neuron subtypes, representing healthy and inflamed states.
- An investigation into how these modulations propagate to a projection neuron, incorporating the specific effects on NMDA receptors.
- The construction of modulation spaces to visualize combined drug effects, highlighting specific lidocaine profiles as trajectories within these spaces.

1.2 Structure

This thesis is divided into four main parts:

Part I establishes the biological context and introduces the primary mathematical framework. Chapter 2 outlines neuronal structure and signaling, detailing the signal from both a physiological perspective and via a foundational mathematical approach: the conductance-based model. Chapter 3 explores the concept of pain and its physiological pathway, before examining therapeutic targets and a key drug candidate, lidocaine, alongside the crucial concept of degeneracy.

Part II details the conductance-based models used in this work. The proposed model represents a simplified pain pathway comprising two interconnected neurons.

Part III presents a computational study of the various modulations induced by lidocaine on its therapeutic targets. Chapter 5 details the baseline characteristics of the model and the function of the targets without modulation. Subsequently, Chapter 6 and Chapter 7 examine how these characteristics evolve under modulation in the first and second neurons, respectively.

Part IV discusses the results in relation to their physiological context. It addresses the limitations of the model and approach while providing directions for future work.

Part I

Background

Chapter 2

Electrophysiology

Electrophysiology is the study of the electrical properties of biological cells. This chapter will cover its fundamentals within the nervous system, starting with a biological description of the key elements involved and concluding with their mathematical representation using a conductance-based model.

2.1 The electrical signaling of the nervous system

2.1.1 The neuron

An excitable cell is defined by its ability to undergo a specific physiological action when triggered by electrical or chemical stimuli. A **neuron** is a specialized type of excitable cell whose function is to communicate rapidly and precisely with other cells of its kind, playing a central role in the body's fast signaling. The receiving cell can either be another neuron, which processes and propagates the information further through the body, or a non-neuronal cell, such as a muscle cell, which contracts to generate movement.

Structurally, most human neurons exhibit an asymmetrical morphology that enables unidirectional signaling, with signal reception carried out by **dendrites** and transmission by an **axon** (Figure 2.1). Dendrites are short branching extensions originating from the cell body, whereas the axon is a single long projection that conducts signals away from it. Although each neuron possesses only one main axon leaving the cell body, this axon can split into multiple branches to communicate with numerous target cells. The connection between two neurons is called a **synapse**, which forms a tiny junctional gap between the axon terminal and the receiving dendrite. The plasma membrane of a neuron is a phospholipid bilayer that is permeable primarily to water and small, uncharged molecules. Because charged ions cannot cross this lipid barrier directly, specialized membrane proteins called **ion channels** provide selective permeability, allowing specific ions to pass. The resulting movement of ions across the membrane generates the electrical signal used by neurons to communicate: the **action potential**, a rapid electrical pulse that propagates along the axon by temporarily altering the local membrane potential.

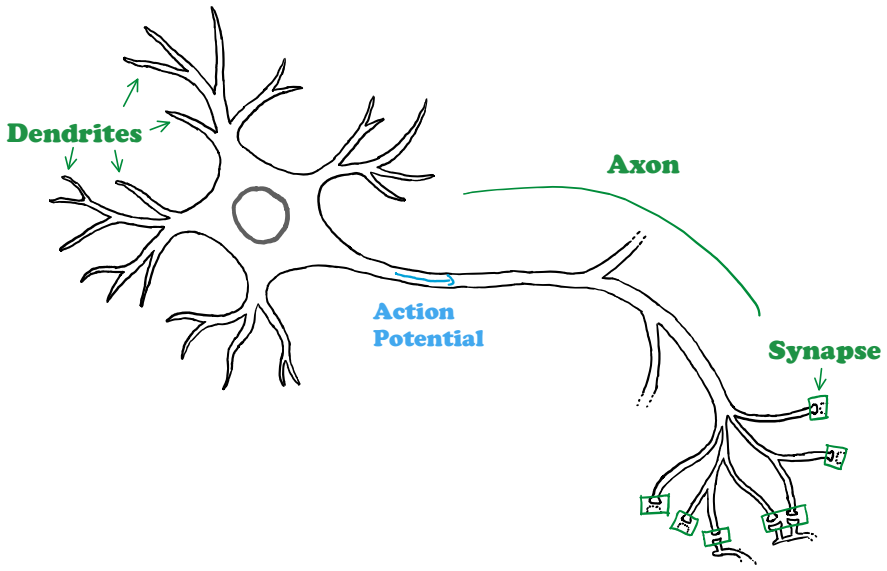

Figure 2.1: Diagram of a neuron. Illustration of signal transmission: dendrites act as receptors, receiving inputs that travel down the axon as an action potential to trigger output at the synapse, transmitting the signal to an excitable cell.

2.1.2 The ion channels

Ion channels are specific proteins that act as selective pores in the cell membrane. Each type of ion channel conducts specific ions across the membrane in response to specific signals (electrical, chemical, or mechanical). For example, voltage-gated channels are affected by changes in membrane potential, phosphorylation-gated channels by phosphorylation, mechanically-gated channels by membrane stretch, and ligand-gated channels by the binding of a chemical transmitter (Figure 2.2). In the context of the nervous system, chemical transmitters are referred to as **neurotransmitters**, and their corresponding ion channels are referred to as **receptors** [1]. The term *gated* refers to the channels' molecular **gates**, which act like cellular doors that regulate the ion channel opening in response to those specific signals.

The combination of the type of stimulus and the targeted ion allows ion channels to be categorized into different families, which can further be divided into subfamilies. For example, there exists a voltage-gated channel family, with the subfamily of voltage-gated sodium channels, which is finally composed of nine distinct types (NaV1.1 to NaV1.9) [2]. These nine share a common overall structure; however, they are encoded by different genes, are expressed in different regions, and have different functions and pharmacological signatures [3].

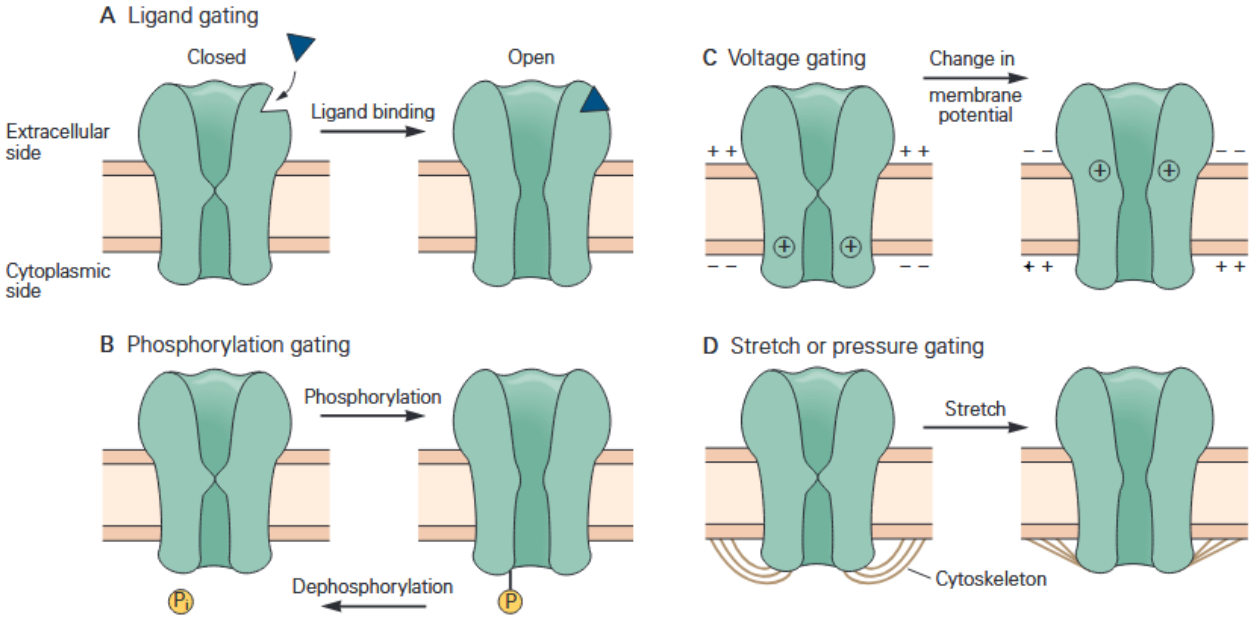

Figure 2.2: Different types of ion channels. **A.** Ligand-gated channel opens when a ligand binds a receptor site on the external surface of the channel protein. **B.** Phosphorylation-gated channel opening is regulated by protein phosphorylation and dephosphorylation. **C.** Voltage-gated channels open and close with changes in the electrical potential difference across the membrane. **D.** Mechanically gated channels open in response to membrane stretch or pressure, either directly through deformation of the membrane or indirectly through forces transmitted by the cytoskeleton or surrounding tissues. The figure comes from [1]

Depending on the presence of its specific stimulus, a gate can be in one of two possible states: *permissive* or *non-permissive*.[1]. An ion channel operates in three distinct states determined by its gates: *open*, *closed*, or *inactivated*. Ions can only pass through when the channel is open, which requires all of its gates to be in a permissive state; if any gate is non-permissive, the channel is closed. Channel inactivation usually follows opening, introducing a period during which the channel is non-conducting and cannot be reopened even if the activation stimulus is present.

Macroscopically, a population of ion channels can be viewed as a **conductance** and the resulting flux of ions as a current, with distinct types of conductances defined by the specific channels involved. Microscopically, an increase in this collective conductance arises from the opening of individual channels, whereas a decrease stems from their closing or inactivation.

The flux of ions through ion channels is passive and requires no metabolic energy, with its direction determined solely by the electrochemical gradient across the membrane. Consequently, action potential generation depends not only on the channels themselves but also on this electrochemical environment, i.e., the ion concentrations inside and outside the cell. These concentration gradients are maintained by transporters and pumps. Unlike channels, these proteins mediate active transport, utilizing metabolic energy to move ions against their gradients. This process relies on a series of conformational changes, resulting in a rate of ion flow that is 100 to 100,000 times slower than that of ion channels.

[1]Permissive and non-permissive are equivalent to open and closed. These words are chosen to distinguish more easily between gates (permissive or non-permissive) and ion channels (open or closed).

2.1.3 The generation of the action potential

The **action potential**, also called a **spike** or nerve impulse, is generated by diffusion and electrostatic gradients acting on sodium and potassium ions crossing the cell membrane and regulated by different ion channels. Before an action potential, the outer side of the membrane is positively charged and contains a high concentration of Na^+ ions. In contrast, the inner side is negatively charged and contains a high concentration of K^+ ions. This is considered the resting state, where there is a K^+ diffusion gradient toward the outside, an Na^+ diffusion gradient toward the inside, and an electrostatic gradient bringing the cations to the inside, but closed ion channels prevent ions from flowing. Knowing all the conditions, the action potential generation can be divided into a succession of events as follows (Figure 2.3):

1. A **stimulus** activates the corresponding receptors and/or ion channels, which leads to an influx of Na^+, increasing the intracellular potential. An example could be mechanically gated sodium channels activated by stretching, or receptors opened by the release of neurotransmitters in the synapse.

2. The intracellular potential reaches a specific **threshold** value that opens voltage-gated sodium channels (VGSCs). A large influx of Na^+ occurs, driven by electrostatic and diffusion forces. This large increase in potential is called **depolarization**.

3. Voltage-gated potassium channels activate (VGKCs), while VGSCs become inactivated. This generates a large efflux of K^+ that produces a decrease in the inner membrane potential, the **repolarization**, toward a smaller potential than that of the resting state.

4. Finally, the VGKCs inactivate, and the pumps use metabolic energy to restore resting conditions. This is the **hyperpolarization** phase.

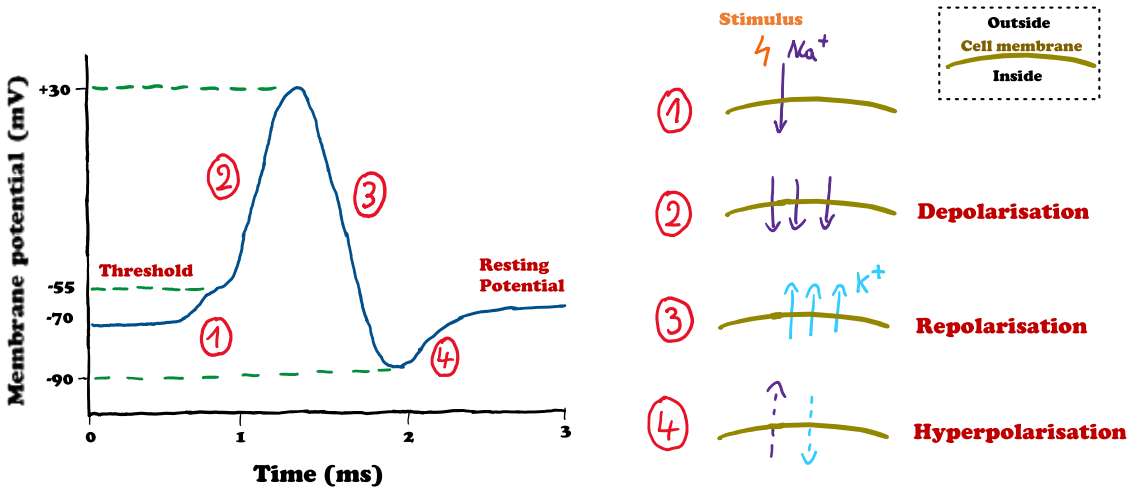

Figure 2.3: Phases of an Action Potential and Corresponding Ion Movements. The graph (left) plots changes in membrane potential (mV) over time (ms), while the corresponding diagrams (right) illustrate the movement of ions across the cell membrane during each numbered phase: **(1)** An initial stimulus causes a small influx of Na^+, driving the membrane potential toward the threshold. **(2)** Upon reaching the threshold, rapid depolarisation occurs as VGSCs open and a massive influx of Na^+ spikes the potential up. **(3)** Repolarisation takes place as VGSCs close and VGKCs open, allowing an efflux of K^+ to restore the negative internal charge. **(4)** Hyperpolarisation occurs because potassium channels are slow to close, causing the potential to temporarily undershoot below the resting potential before the pumps restore it to its resting potential.

Regarding how it is generated, different properties can be extracted. Firstly, the action potential is initiated only when the membrane voltage reaches a threshold and is an all-or-nothing event. The amplitude produced by depolarization is the same for a stimulus that barely surpasses the threshold and a stimulus corresponding to a large current. Secondly, the action potential is followed by a refractory period, which begins during the hyperpolarization phase, meaning that a neuron cannot immediately fire again and requires a recovery time before generating another impulse.

These two properties lead to a third: the unidirectional and self-regenerative propagation of the spike along the axon. This propagation occurs sequentially, with each membrane segment triggering the adjacent one. For instance, as a spike moves from left to right, the depolarization causes a portion of the influxed Na^+ to spread to neighboring segments. Because the segment to the left has just fired, it remains in a refractory period and cannot be re-excited. Conversely, the segment to the right has not yet fired, allowing this lateral sodium spread to act as the initiating stimulus that triggers the next action potential.

Since this self-regenerative mechanism maintains a constant amplitude, signal intensity cannot be conveyed by the size of individual spikes. Instead, stimulus strength is encoded by **firing frequency**: a stronger stimulus triggers a higher number of action potentials per second.

2.2 Modeling of a neuron: the conductance-based model

In 1952, Hodgkin and Huxley developed the first conductance-based model, which describes the excitability of the neuronal membrane [4]. To achieve this, they modeled the membrane using an analogy to an electrical circuit, thereby establishing a mathematical model of action potential generation.

2.2.1 Electrical Equivalent Circuit

A conductance-based model represents the electrical properties of a segment of nerve membrane, as shown in Figure 2.4. In this circuit, two major currents flow across the membrane: one associated with the charging of the membrane capacitance of the phospholipid bilayer ($C_m \frac{dV}{dt}$), and one associated with the movement of different ions across the membrane through ion channels (I_{ion}). In the case of the Hodgkin-Huxley model, the ionic current is subdivided into three distinct currents: the sodium current (I_{Na}), the potassium current (I_K), and the leakage current (I_L).

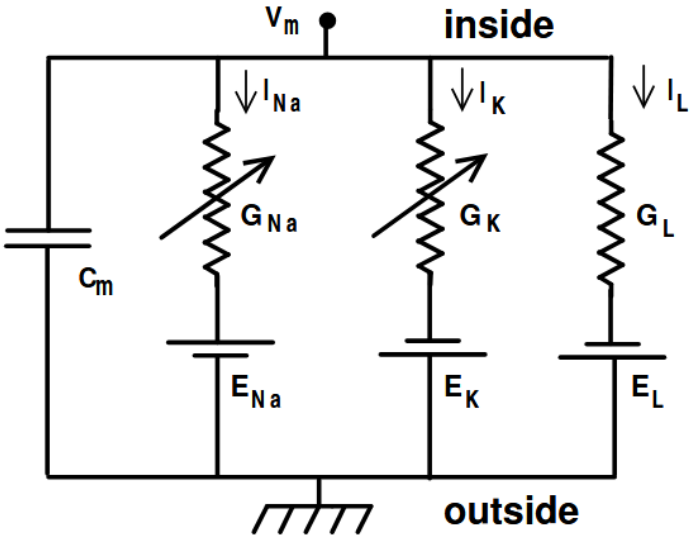

Figure 2.4: Electrical circuit representing a membrane segment [4]. Here, C_m is the membrane capacitance, E_i is the equilibrium potential, and G_i is the voltage-dependent conductance associated with the current I_i.

Considering an extra external applied current (I_{ext}), which can be seen as a stimulus, the membrane capacitance (C_m), and the membrane potential (V). From Kirchhoff's law, it can be written as the differential equation:

$$C_m \frac{dV}{dt} + I_{ion} = I_{ext} \tag{2.1}$$

Convention

In Equation 2.1, the convention is "inward negative", which means that an inward flow of positive ions is considered a negative current; i.e., a positive I_{ion} will make V more negative, unlike a positive I_{ext}, which will make V more positive. The convention used is not important in itself, but one must ensure consistency when implementing the model and interpreting the results.

2.2.2 The Ionic Currents

General Formulation

The total ionic current I_{ion} is the algebraic sum of the individual contributions from all participating ion types, with an associated conductance value G_j and equilibrium potential E_j

$$I_{ion} = \sum_j I_j = \sum_j G_j(V - E_j). \tag{2.2}$$

Hodgkin and Huxley postulated that these ion conductances are functions of the membrane potential. Recall from subsection 2.1.2 that these macroscopic conductances result from the combined effects of a large number of ion channels and that each ion channel can be in an open, closed, or inactivated state; i.e., ions can or cannot flow through the channel. This state is regulated by gates; for a channel to be open, all its gates must be in the permissive state and none in the non-permissive state.

Defining p_i as the probability of an individual gate of type i being in the permissive state, and α_i and β_i as the transition rates from "non-permissive to permissive" and from "permissive to non-permissive", respectively, the evolution of the gate variable can be written as

$$\frac{dp_i}{dt} = \alpha_i(V)(1 - p_i) - \beta_i(V)p_i. \tag{2.3}$$

By considering a large number of voltage-gated channels, p_i can also be interpreted as the proportion of gates in the permissive state, and $(1 - p_i)$ as the proportion in the non-permissive state, with α_i and β_i that are functions of the membrane potential. If the voltage is fixed at some value V, p_i can reach a steady-state value ($p_{i,\infty}$) (i.e., $\frac{dp_i}{dt} = 0$ as $t \to \infty$), where the time required to reach this steady state is described by the time constant τ_i.

$$p_{i,\infty}(V) = \frac{\alpha_i(V)}{\alpha_i(V) + \beta_i(V)}, \tag{2.4}$$

$$\tau_i(V) = \frac{1}{\alpha_i(V) + \beta_i(V)}. \tag{2.5}$$

Knowing Equation 2.4 and Equation 2.5, Equation 2.3 can also be rewritten in terms of these two introduced functions:

$$\frac{dp_i}{dt} = \frac{p_{i,\infty} - p_i}{\tau_i}. \tag{2.6}$$

The proportion of channels in the open state is proportional to the probability that the corresponding gates are in the permissive state. The macroscopic conductance (G_j) due to channels of type j, with constituent gates of type i, is proportional to the product of the individual gate probabilities (p_i), referred to as channel **availability**. Defining $\bar{g}_j$ as the maximum possible conductance when all channels are open, the expression is given by:

$$G_j = \bar{g}_j \prod_i p_i. \tag{2.7}$$

Example with the Hodgkin-Huxley model

In the Hodgkin-Huxley model, sodium conductance uses three gates of type m and one gate of type h, while potassium conductance uses four gates of type n. Using the notation $p_i \equiv i$ (e.g., $p_m \equiv m$), Equation 2.7 become:

$$G_{Na} = \bar{g}_{Na} m^3 h,$$

$$G_K = \bar{g}_K n^4.$$

The leakage current is considered to be directly proportional to the difference from the equilibrium potential, without any gates. In other words, the corresponding conductance is constant ($G_L = \bar{g}_L$). Since all macroscopic conductances are known, the ionic current is defined as (using Equation 2.2)

$$\begin{aligned} I_{ion} &= I_{Na} + I_K + I_L \\ &= G_{Na}(V - E_{Na}) + G_K(V - E_K) + G_L(V - E_L) \\ &= \bar{g}_{Na} m^3 h (V - E_{Na}) + \bar{g}_K n^4 (V - E_K) + \bar{g}_L (V - E_L). \end{aligned}$$

Finally, using Equation 2.1 and Equation 2.6, the resulting system of differential equations is

$$\begin{aligned} \frac{dV}{dt} &= \frac{I_{ext} - I_{ion}}{C_m}, \\ \frac{dm}{dt} &= \frac{m_\infty - m}{\tau_m}, \\ \frac{dh}{dt} &= \frac{h_\infty - h}{\tau_h}, \\ \frac{dn}{dt} &= \frac{n_\infty - n}{\tau_n}. \end{aligned}$$

Here, V, m, h, and n are variables. I_{ext}, C_m, and the different $\bar{g}_j$ are parameters. The different $p_{i,\infty}$ and τ_i are functions of the membrane potential and are usually derived from experimental data.

Gate variables as inactivation and activation gate variables

The gates can be divided into two categories: *activation* and *inactivation* gates. The *activation* gate steady state ($p_{act,\infty}$) is a sigmoid with a positive slope, so that if the function is considered from left to right (negative to positive values), $p_{act,\infty}$ is first zero (deactivated) and then equal to one (activated). In contrast to $p_{act,\infty}$, the *inactivation* gate steady state ($p_{inact,\infty}$) is first equal to one (deinactivated) and then equal to zero (inactivated) (see Figure 2.5).

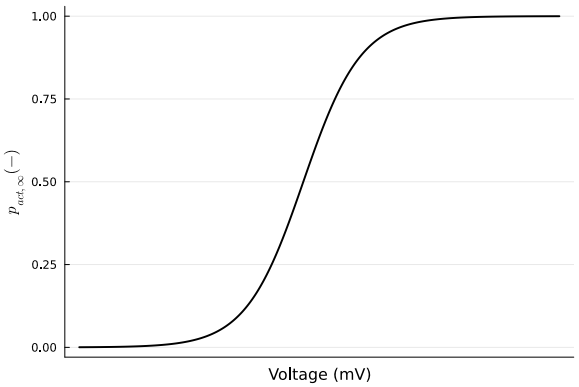

(a) Example of an activation gate steady-state function ($p_{act,\infty}$). It is a sigmoid with a positive slope, taking a value of 0 at low membrane potentials (deactivated) and a value of 1 at high membrane potentials (activated).

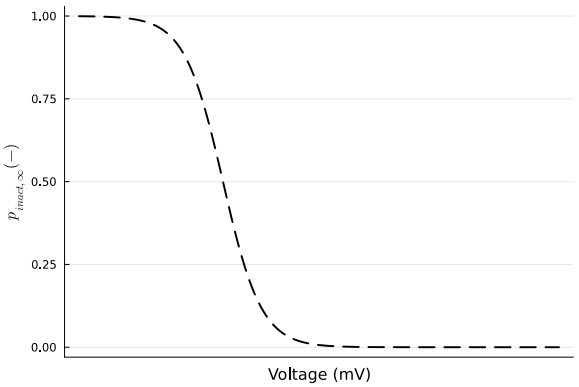

(b) Example of an inactivation gate steady-state function ($p_{inact,\infty}$). It is a sigmoid with a negative slope, taking a value of 1 at low membrane potentials (deinactivated) and a value of 0 at high membrane potentials (inactivated).

Figure 2.5

Example of simulation

Figure 2.6 shows subthreshold and suprathreshold simulations using the Hodgkin-Huxley model. Both n and m act as activation gates with low values before the spike, whereas h acts as an inactivation gate that is initially at a higher value. During the spike upstroke, m activates to drive depolarization (corresponding to Na^+ influx), whereas h inactivates (terminating Na^+ influx) and n activates (corresponding to K^+ efflux) to drive repolarization.

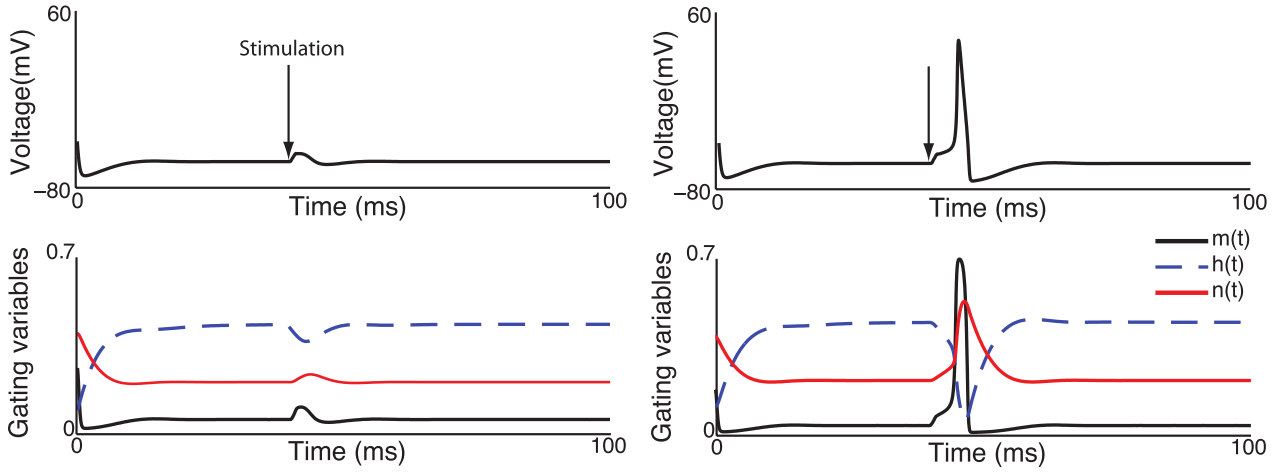

Figure 2.6: Simulation of the Hodgkin-Huxley model showing the traces of both the voltage and the gating variables under subthreshold and suprathreshold stimulation [5].

Chapter 3

Pain Processing and Management

This chapter explains what pain is and how it originates in the body, tracing its pathway from nociceptors to the spinal cord while omitting higher-level processing in the brain. Subsequently, to explore strategies for managing unwanted pain, key potential drug targets and the phenomenon of degeneracy will be presented alongside a representative drug candidate, lidocaine.

3.1 Pain Processing

3.1.1 Definition of pain

According to the International Association for the Study of Pain (IASP), **pain** is defined as: *An unpleasant sensory and emotional experience associated with, or resembling that associated with, actual or potential tissue damage*. In each case, pain is accompanied by an unpleasant sensation, so anyone experiencing pain instinctively wants to remove the source of the signal. Under healthy conditions, pain is typically elicited by stimuli that can cause or aggravate tissue injury. The pain signal acts as a protective alarm for the organism. Protective pain is broadly split into two distinct categories: nociceptive and inflammatory. Conversely, when pain serves no adaptive or protective purpose, it is classified as a third category known as pathological pain (Figure 3.1) [6].

- **Nociceptive pain** concerns intense noxious stimuli to prevent injury. Since intense stimulation is more likely to rapidly lead to significant damage, it is considered urgent for the body and leads to a fast reaction, a withdrawal reflex, to avoid danger. An example would be removing a hand from the fire, corresponding to an intense thermal stimulus that could lead to burning.
- The purpose of **inflammatory pain** is to promote healing and prevent further damage. Intuitively, an injured area is likely to be more fragile and could therefore be damaged by less intense stimuli. To account for this, the pain is associated with a pain sensation of greater intensity than expected from a normally painful stimulus and an appearance of pain for a normally non-painful stimulus. These two phenomena are referred to as **hyperalgesia** and **allodynia**, and result from adaptations that are activated by the immune system at the site of injury.
- **Pathological pain** results from abnormal functioning of the nervous system and can be divided into two subtypes: neuropathic pain and dysfunctional pain. **Neuropathic pain** occurs after damage to the nervous system. Dysfunctional pain refers to a situation where there is no such damage or inflammation.

Unlike inflammatory pain, neuropathic pain is not linked to inflammation at the site where pain is perceived and does not convey useful protective information. However, similarly to inflammatory pain, it is characterized by allodynia, hyperalgesia, and even spontaneous pain [7, 8]. In both inflammatory and neuropathic pain, these changes can be understood as part of a broader phenomenon known as **sensitization**.

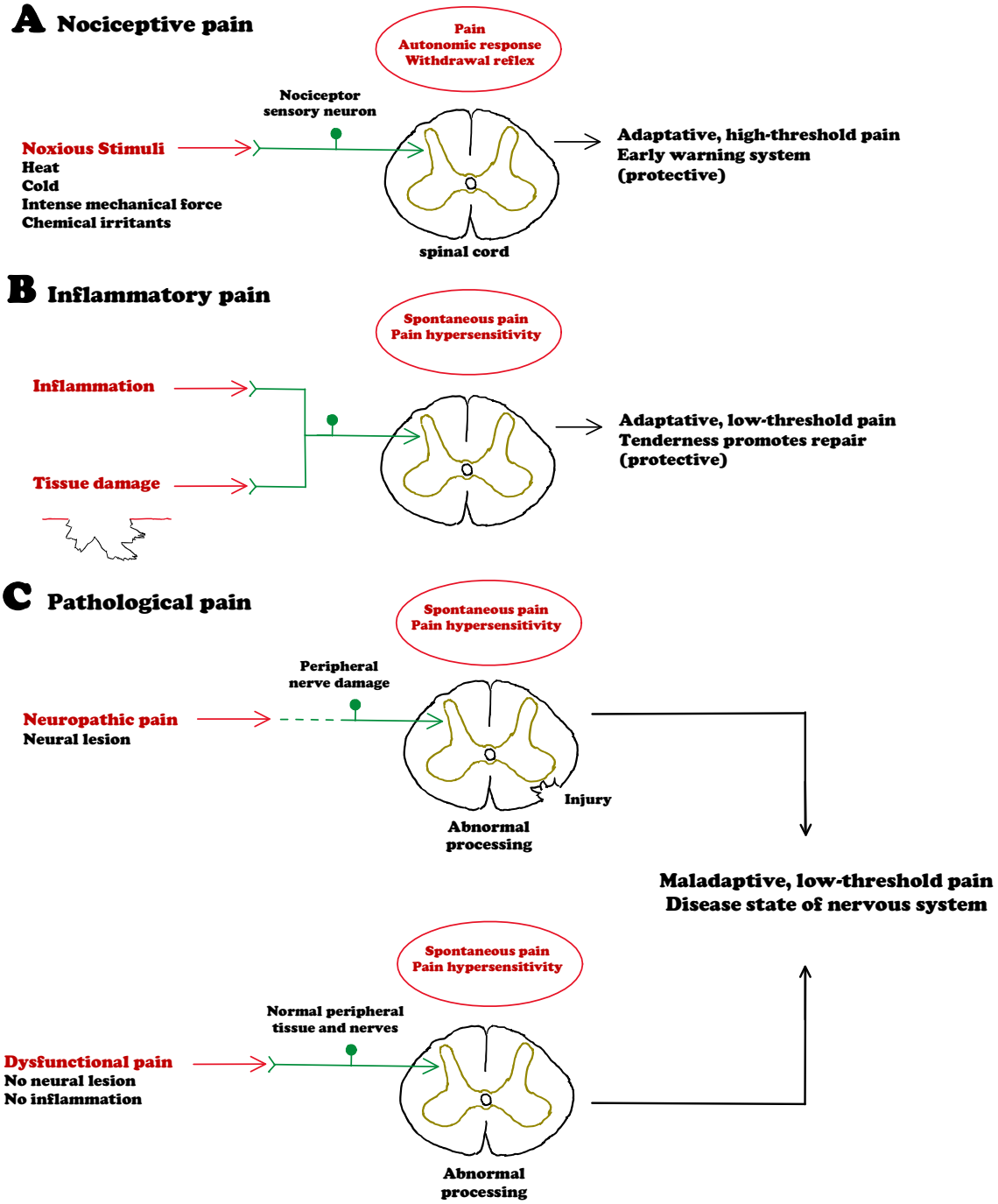

Figure 3.1: The three types of pain. **A.** Nociceptive pain is a protective sensation triggered by the detection of noxious, potentially tissue-damaging stimuli. **B.** Inflammatory pain is associated with tissue damage and the infiltration of immune cells. It promotes healing by causing temporary hypersensitivity until recovery is complete. **C.** Pathological pain is a disease state that can result either from direct damage to the nervous system (neuropathic) or from its abnormal functioning (dysfunctional) [6].

3.1.2 The pain pathway

The pain pathway begins at the origin of the signal within nociceptors, detailing how this signal is transmitted through peripheral nerve fibers to the dorsal horn of the spinal cord. Although the signal is subsequently transmitted to and processed by higher brain centers, this final stage falls outside the scope of this work.

Nociceptors

A **nociceptor** is a sensory neuron specialized for noxious stimuli, i.e., one that detects potentially damaging or harmful stimuli. Four classes of nociceptors can be distinguished: mechanical, thermal, polymodal, and silent.

Mechanical nociceptors are activated by intense pressure that stretches the membrane, which also includes incisions that break the skin surface. Similarly, **thermal nociceptors** are activated by extremely low (less than 5 $°C$) or high (higher than 45 $°C$) temperatures. The conversion of mechanical and thermal stimuli into electrical stimuli is carried out, respectively, by mechanically gated ion channels and a family of so-called transient receptor potential (TRP) ion channels. **Polymodal nociceptors** can be activated by high-intensity mechanical, chemical, or thermal stimuli. **Silent nociceptors** do not respond to any stimuli under normal conditions because of their very high threshold; they are activated by inflammation and contribute to sensitization [1].

In fact, the cell bodies of nociceptors are not located at the skin's surface where an injury occurs; instead, they are safely housed inside the **dorsal root ganglion** (DRG), just outside the spinal cord. What actually senses the noxious stimuli are the peripheral nerve endings, which convert the stimuli into electrical signals that travel along specific nerve fibers.

Nerve fibers

Regulating action potential speed in different nerve fibers allows the nervous system to accelerate urgent signals relative to non-urgent ones. This distinction is achieved because certain nerve fibers are *myelinated*, meaning their axons are insulated by myelin sheaths. Produced by non-excitable glial cells, this myelination optimizes communication by increasing signal propagation speed by up to a factor of 100.

When you stub your little toe against a chair, you first feel a sharp pain, the *first pain*, and then a more diffuse and less intense pain, the *second pain*. These two pains are transmitted by two different types of nerve fibers. The first is induced by thinly myelinated fibers, $A\delta$ **fibers**, that conduct action potentials at speeds of 5 to 30 m/s. The second is conducted by unmyelinated fibers, C **fibers**, with action-potential conduction speeds below 1 m/s [1]. The different types of nociceptors are also associated with specific fibers; mechanical and thermal nociceptors mainly include $A\delta$ fibers, whereas polymodal and silent nociceptors mainly consist of C fibers.

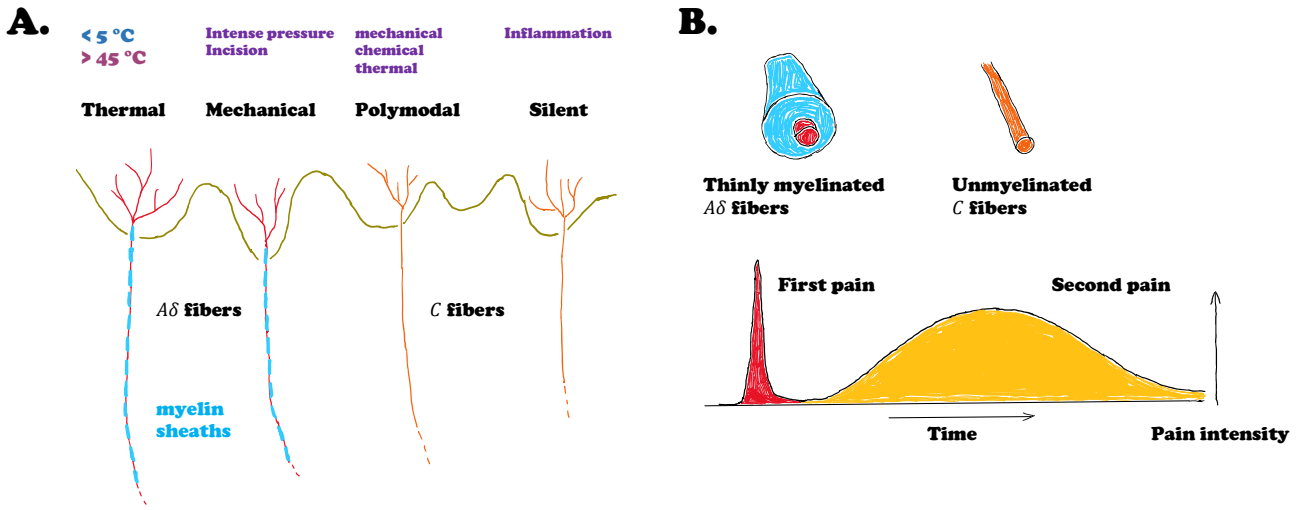

Figure 3.2: **A.** Four primary classes of peripheral nociceptors and their associated nerve fibers. Peripheral nociceptors fall into four main categories: thermal, mechanical, polymodal, and silent. Thermal and mechanical nociceptors transmit signals via $A\delta$ fibers for rapid transmission, whereas polymodal and silent nociceptors transmit via C fibers [1]. **B.** Nociceptive signals are processed in two sequential phases: *first pain*, carried by thinly myelinated $A\delta$ fibers, is sharp and precisely localized, and *second pain*, transmitted via unmyelinated C fibers, arrives later and is characterized as a duller, more diffuse sensation [1].

In the context of nociception, there is a last notable fiber type, the **$A\beta$ fibers**, which are thicker, myelinated fibers with an action potential speed of up to 75 m/s. These fibers are associated with all cutaneous mechanoreceptors, including those specialized for the detection of vibration, and are additionally crucial for proprioception. Even though these are non-nociceptive fibers, $A\beta$ fibers interact with the pain pathway at the level of the dorsal horn.

Dorsal Horn Neurons

The **dorsal horn** serves as the primary relay center for nociceptive information. C and $A\delta$ nerve fibers synapse with dorsal horn neurons (DHNs), which comprise both interneurons and projection neurons. Specifically, $A\delta$ fibers connect predominantly to projection neurons, whereas C fibers primarily target interneurons, even though both neuron types can receive inputs from both afferent types:

- **Projection neurons** process and transmit nociceptive information to higher centres in the brain. Note that the brain will still process the signal, meaning that receiving a nociceptive signal does not necessarily induce a pain sensation.
- **Interneurons** allow modulation of the signal received by projection neurons, as well as modulation of their excitability. They synapse onto other interneurons that further process the signal and/or onto projection neurons.

Interneurons can either be excitatory or inhibitory, depending on the neurotransmitter released. Inhibitory interneurons release GABA, which binds to GABA receptors. Excitatory interneurons release glutamate, the main excitatory neurotransmitter, which binds to several receptors, including AMPA and NMDA. Inhibitory interneurons can be stimulated by $A\beta$ fibers, which can be illustrated by someone shaking their hand after being hit to reduce the pain sensation. Higher centers can also influence pain transmission at the dorsal horn via a descending modulatory system by inducing excitatory or inhibitory inputs [9].

3.1.3 Sensitization

The IASP defines **sensitization** as: *Increased responsiveness of nociceptive neurons to their normal input, and/or recruitment of a response to normally subthreshold inputs*. This can include a drop in threshold and an increase in suprathreshold response, spontaneous discharges, and increases in receptive field size.

Roughly speaking, sensitization can be seen as hyperexcitability in the context of nociception. **Hyperexcitability** refers to a neuron that spikes excessively. "Excessive" means that the neuron exhibits abnormal spiking activity in response to stimuli that should not normally elicit such a response, amplifies normal evoked spiking, and can display spontaneous spiking [7] (Figure 3.3). However, sensitization does not involve only isolated nociceptive neurons; it involves both nociceptors and dorsal horn neurons. These two components are distinguished as peripheral and central sensitization.

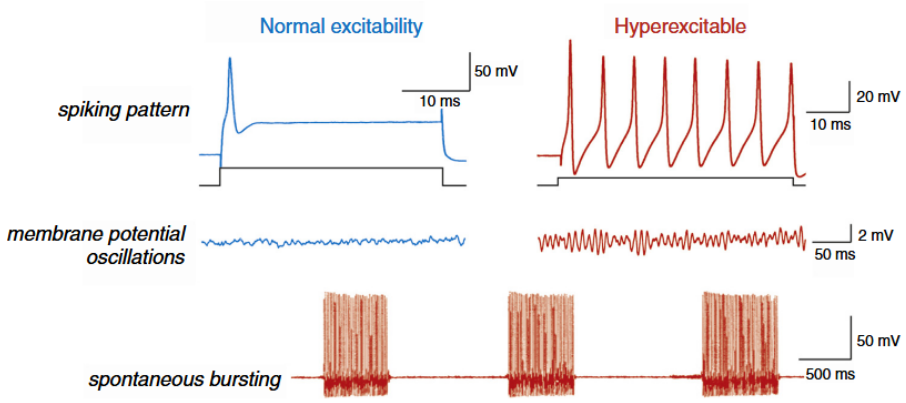

Figure 3.3: Hyperexcitability in primary afferent neurons. Nerve injury induces qualitative changes in somatic excitability, driving hyperexcitability characterized by altered spiking patterns, pronounced membrane potential oscillations, and spontaneous burst firing [7].

Peripheral sensitization

Peripheral sensitization is triggered by changes in the local chemical environment at the injured site. Sensory nerve fibers and inflammatory cells release inflammatory chemicals; some directly activate peripheral nociceptors, while others have a more modulatory role by decreasing neuronal thresholds. Silent nociceptors are among the most affected, since they are exclusively activated under such conditions. All of this leads to an increase in afferent signals coming from *C* and *Aδ* fibers, which causes **primary hyperalgesia**. Hyperalgesia means increased pain from a stimulus that usually provokes pain, and the term *primary* specifies that it occurs at the site of injury [10, 11].

Central sensitization

In **central sensitization**, the dorsal horn neurons' interpretation of afferent stimuli is altered. A major cause of these alterations is the activity dependence of central sensitization. The large sensory inflow resulting from peripheral sensitization provokes an increase in the excitability of DHNs. This increase includes both homosynaptic and heterosynaptic facilitation [12]:

- **Homosynaptic facilitation**, also called **wind-up**, describes the increase in action potential output during repetitive firing of an identical input. In other words, when a DHN receives repetitive firing from an identical C-fiber, even though the intensity and frequency of the afferent input do not change, the resulting DHN response becomes greater and greater.
- **Heterosynaptic facilitation** is the increase in a DHN's response to an afferent input caused by activity in a different afferent pathway. For instance, if a DHN is connected to afferent fibers 1 and 2, stimulation of fiber 1 will potentiate the DHN's response to inputs from fiber 2.

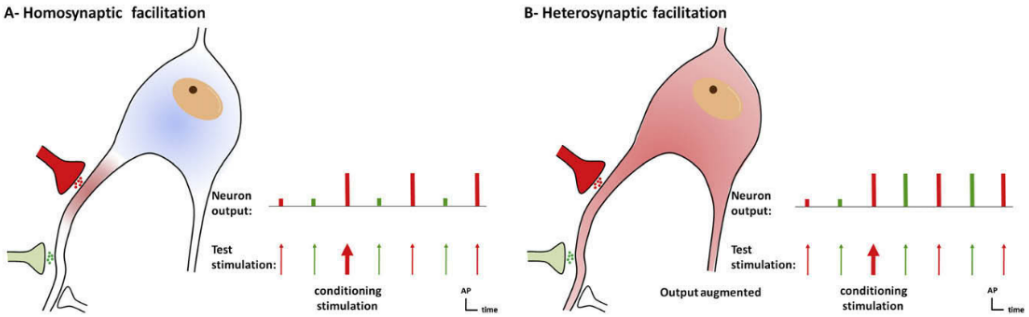

Figure 3.4: Illustration of homosynaptic and heterosynaptic facilitation. **A.** Homosynaptic facilitation: An increase in the response to a stimulus at a synapse resulting from its own activation. **B.** Heterosynaptic facilitation: A global increase in the responses of a neuron following the activation of one of its synapses. [13]

These changes can alter how inputs from $A\beta$ fibers are interpreted, enabling innocuous mechanical stimuli to result in pain (**allodynia**) and allowing this hypersensitivity to spread to stimuli originating outside the area of injury (**secondary hyperalgesia**) [11]. Physiologically, these mechanisms arise from a complex cascade of molecular interactions within synapses, including glutamate-NMDA interactions. The release of these different substances cannot be maintained indefinitely without afferent activity. In the absence of further nociceptor inputs, these facilitations typically last from tens of minutes to several hours and are therefore considered short-term. Long-term changes are partially caused by alterations in neuronal gene expression, where these alterations are induced by maintaining the short-term mechanisms over a prolonged period [10].

3.2 Potential targets to reduce pain

To influence biological processes such as sensitization, drugs can aim to inhibit specific targets that cause the unwanted behavior by using channel blockers. A **channel blocker** is a specific type of inhibitor molecule that prevents ions from flowing through ion channels, either by physically obstructing the ion pathway or by inducing a structural change that keeps the channel closed. A blocker can target one specific type of ion channel or act on several types; for example, **tetrodotoxin** (TTX) is a blocker that specifically targets voltage-gated sodium channels. TTX therefore leads to muscle paralysis and is more commonly known for its presence in fugu fish, requiring careful preparation by the chef when the fish is cooked.

To explore the use of channel blockers to manage unwanted hyperexcitability, this section focuses on two targets: VGSCs at the nociceptor level and NMDA receptors within the dorsal horn neurons.

3.2.1 Voltage-gated sodium channels

In the context of peripheral nociception, four sodium channels are mainly considered potential therapeutic targets: **NaV1.7**, **NaV1.8**, and **NaV1.9**, which play a crucial role in peripheral neurons, and **NaV1.3**, which is not present in the DRG under naive conditions but is newly expressed after nerve injury. A further advantage is that these channels are not essential for central nervous system neurons or cardiac muscle cells [14].

NaV1.7 is activated at potential values close to the resting potential, facilitating the reaching of the action potential threshold; it sets the gain of the nociceptor. Also, its slow inactivation kinetics sustain depolarization and generate longer-lasting effects. All these properties make it important in nociception. In fact, the significant role of this channel was demonstrated in genetic studies, where loss-of-function mutations lead to loss of pain sensation and gain-of-function mutations to pain hyperexcitability [15, 14, 16, 17].

NaV1.8 produces most of the sodium current responsible for the AP upstroke and repetitive firing because of its activation at depolarized potentials. The increase in NaV1.8 current in the presence of inflammatory mediators suggests that it has a crucial role in maintaining inflammatory pain [15, 14, 16, 17].

NaV1.9 induces a small non-inactivating current around the resting potential. It results in a persistent current with slow kinetics that does not contribute to the action potential upstroke. Its contribution to increased excitability comes from its constant presence, which prolongs and enhances small depolarizations. The NaV1.9 current is increased by inflammatory mediators, suggesting a role in maintaining inflammation-induced hyperalgesia [17, 14].

Since **NaV1.3** is exclusively expressed in the peripheral nervous system during nerve injury, this channel has attracted attention as a potential therapeutic target. NaV1.3 has activation and inactivation properties similar to those of NaV1.7 but at even lower potentials; thus, it amplifies small inputs. Also, its fast kinetics and rapid repriming allow it to create a persistent[1] current reacting in response to small depolarizations. This channel is likely to contribute to hyperexcitability and the generation of spontaneous spiking [18, 17].

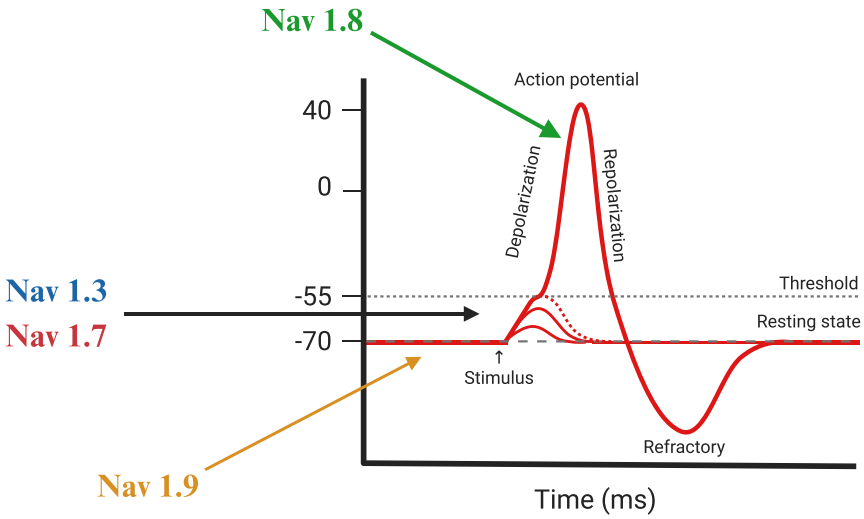

Figure 3.5: Contribution of NaV1.7, NaV1.8, NaV1.9, and NaV1.3 to the different phases of action potential generation [15].

A common VGSC distinction is to categorize channels as either sensitive or insensitive to TTX. This distinction enables the experimental discrimination between TTX-sensitive (TTX-S) and TTX-resistant (TTX-R) currents and their corresponding sodium channels. This characteristic and the preceding one are summarized in Table 3.1.

VGSC	TTX sensitivity	kinetics	Role in AP generation
NaV1.3	TTX-S	fast	Amplification of small depolarization with a large ramp current, spontaneous firing
NaV1.7	TTX-S	fast	Ramp current that sustain depolarization
NaV1.8	TTX-R	slow	AP upstroke, and repetitive spiking
NaV1.9	TTX-R	ultra slow	Amplifies and prolongation of small depolarization

Table 3.1: Biophysical properties and functional roles of key voltage-gated sodium channel subtypes in peripheral DRG neurons during nociceptive signaling

[1]The persistent current of NaV1.3 comes from the rapid reaction of the current, making it rapidly appear and all the time present. In NaV1.9, it comes from the slow dynamics, making it persistent because it does not disappear.

3.2.2 Synaptic receptors

In the dorsal horn, **AMPA** and **NMDA** receptors are key mediators of neuronal excitability; they are both ligand-gated ion channels sensitive to glutamate. More specifically, AMPA and NMDA receptors are permeable to both Na^+ and K^+, with NMDA receptors having an additional permeability to Ca^{2+}. In comparison to AMPA receptors, NMDA receptors are blocked by magnesium, which induces an indirect voltage dependence, whereby an increase in membrane potential repels Mg^{2+}, leaving the NMDA receptor unblocked [19].

This last property explains one of the key roles of NMDA receptors in central sensitization—specifically, in the **wind-up** phenomenon. The progressive increase in responses to repetitive afferent input stems from sustained membrane depolarization, which expels the Mg^{2+} block from the NMDA channel pore. Another key role arises from its **calcium permeability**. An increase in intracellular Ca^{2+} above a critical threshold triggers activity-dependent processes. Calcium activates several intracellular pathways that induce: phosphorylation of AMPA and NMDA receptors (increasing their activity), activation of voltage-gated calcium channels (VGCCs) to import additional Ca^{2+}, retrograde signaling to upregulate presynaptic neurotransmitter release, and gene transcription to drive long-term structural changes (Figure 3.6) [16, 20, 21]. Aguiar et al. [22] showed that NMDAR alone is not sufficient to exhibit a wind-up pattern. To get a more significant increase in response, the presence of calcium dynamics is needed, as can be seen in Figure 3.7.

Ultimately, these intracellular cascades and diffusible messengers do not remain confined to the active synapse. They can spill over and modulate adjacent, unstimulated pathways, driving **heterosynaptic facilitation** [13].

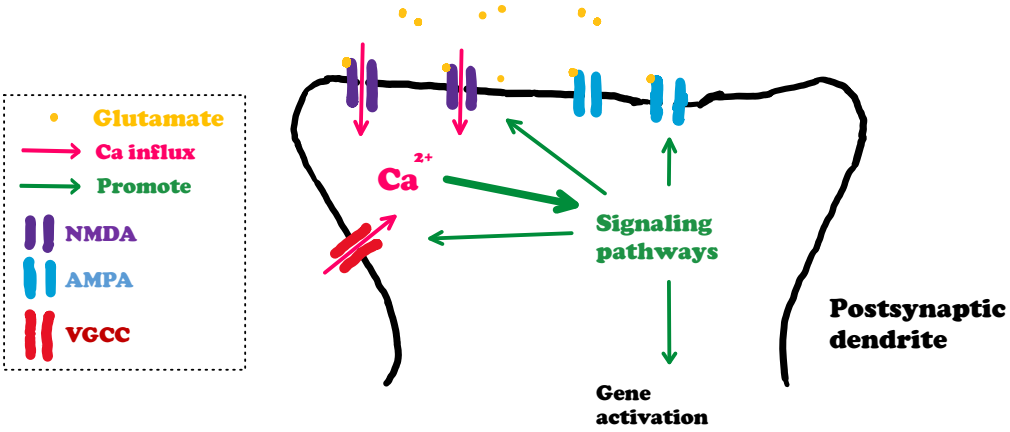

Figure 3.6: Schematic diagram of the NMDA receptor and the role of Ca^{2+} in activity-dependent plasticity. Ca^{2+} influx through NMDA receptors triggers a downstream signaling cascade that promotes gene expression, increases AMPA and NMDA receptor activity, activates voltage-gated calcium channels, and enhances presynaptic neurotransmitter release.

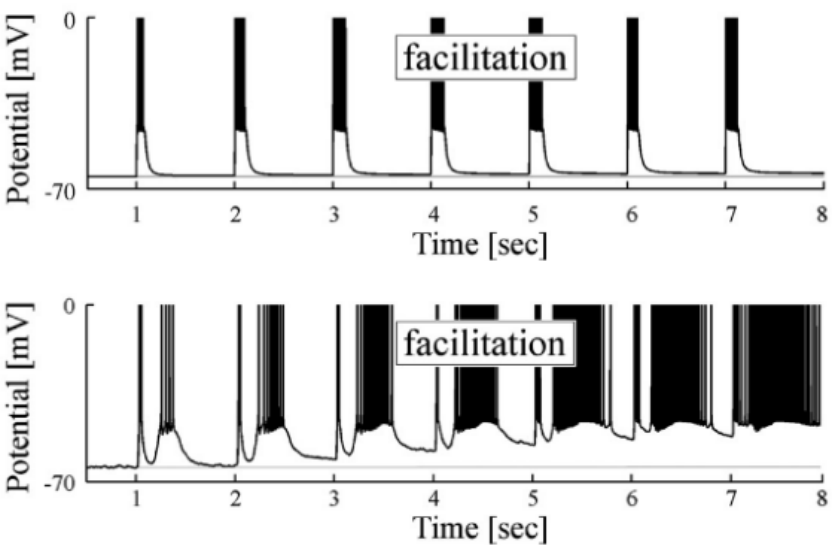

Figure 3.7: **(Top)** Interneuron membrane potential traces, where this neuron does not contain calcium currents. The small cumulative depolarization that can be seen is driven by a long-lasting NK1 receptor that will not be discussed here. **(Bottom)** Wide dynamic range (WDR) neuron membrane potential traces showing cumulative depolarization as multiple mechanisms, including calcium channel and NMDA receptor dynamics, occur simultaneously. Figure adapted from [22].

3.3 Degeneracy

Degeneracy is a broad phenomenon with important implications across several domains. This section defines the concept, its effects on electrophysiology, and its role in therapeutics.

3.3.1 Definition

Degeneracy refers to an outcome that does not have a unique basis [7]. In other words, there exist different elements (or combinations of elements) that can produce a similar result [23]. Both *elements* and *results* are defined broadly here to encompass a wide array of biological components and functional outcomes. Degeneracy should not be confused with redundancy, in which multiple instances of the same element produce the same result. Considering a function A and the two different molecules x and y, redundancy implies that there exist several instances of x, even though a single x is sufficient to ensure A. Degeneracy implies that both x and y exist, even though each of them can individually ensure A (Figure 3.8) [24, 25].

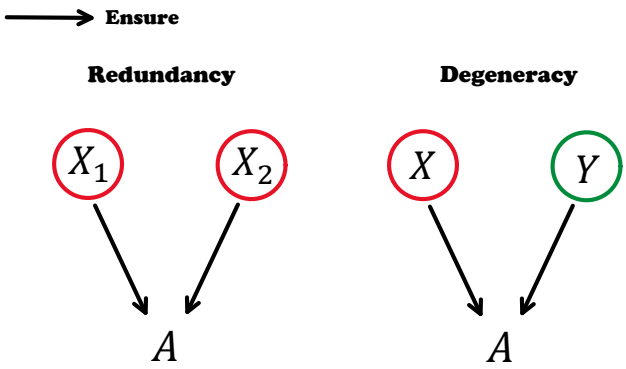

Figure 3.8: Redundancy vs. Degeneracy in Functional Systems [24]. In a redundant system, identical elements (X_1 and X_2) independently execute the same function A. In a degenerate system, distinct elements (X and Y) can execute function A. This structural diversity grants degenerate systems greater robustness against specific disruptions, such as an antagonist that targetedly inhibits X, leaving Y available to preserve function A.

In electrophysiology, degeneracy occurs both during action potential generation and within the overall firing pattern. Where the elements are the different combinations of ion channels, resulting in similar spike shapes or neuronal excitability (e. g., single spike, spiking, ...).

For example, during spike generation, the depolarization phase is driven by sodium current. This current arises from the opening of various types of VGSCs, each of which operates over a specific range of membrane potentials and possesses distinct gating kinetics. Degeneracy occurs when these voltage ranges and gating kinetics overlap (Figure 3.9). Consequently, despite differences in the intrinsic properties of individual channels, these overlaps allow them to substitute for one another [24]; i.e., a change in the conductance of certain ion channels can be compensated for by altering the conductance contributions of others, ultimately maintaining the same overall excitability. This degeneracy can be illustrated using conductance-based models, where different sets of conductances result in similar firing patterns (Figure 3.10).

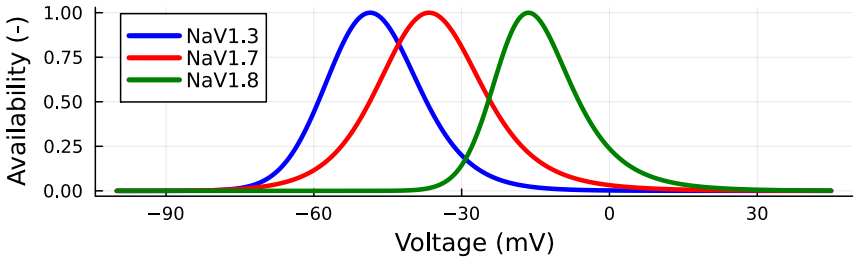

Figure 3.9: Degeneracy of Voltage-Gated Ion Channels. The degeneracy occurs when different channels have overlapping functions. The curves illustrate the overlapping steady-state availability of the three types of VGSCs from the conductance-based model used in this thesis.

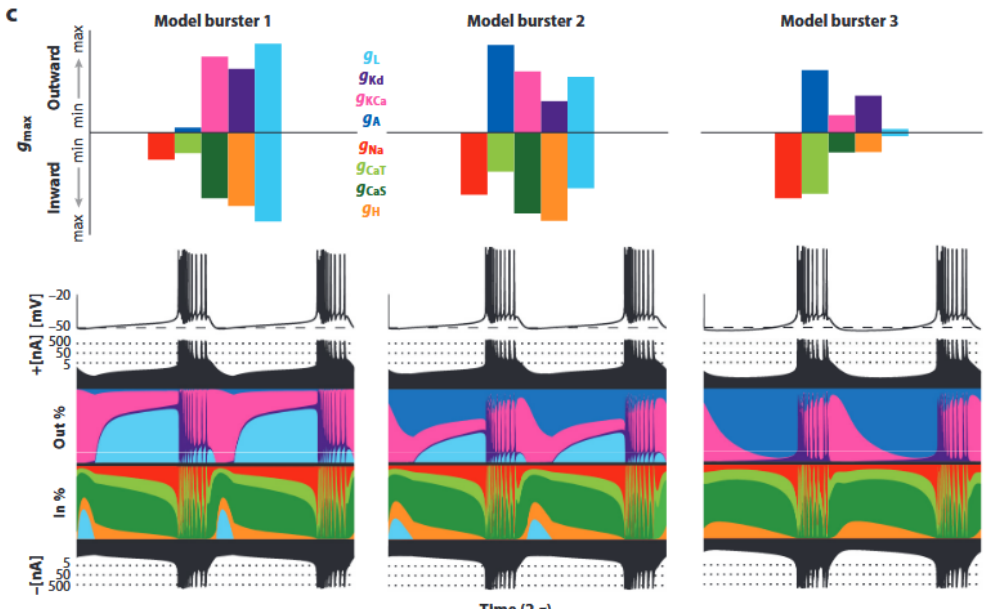

Figure 3.10: Multiple solutions generate similar activity patterns. Model neurons 1, 2, and 3 show similar voltage evolutions (middle black traces) despite having different sets of maximal conductances g_{max} (top row). The bottom graphs (currentscapes) show the total outward and inward currents (black currentscapes) and the contribution of each conductance (colored currentscapes) during one activity cycle [24].

3.3.2 The impact of degeneracy in therapy

From a biological point of view, degeneracy allows biological systems greater flexibility to achieve the same outcome, conferring robustness to impairments in one or more elements. Returning to the context of Figure 3.8, if an antagonist strictly specific to x appears, then with redundancy, all instances of x would be affected, preventing function A, whereas with degeneracy, y would preserve function A.

In healthy conditions, this robustness is an advantage, protecting biological functions from unexpected impairments. However, it becomes problematic when this degeneracy is responsible for a pathological outcome. If the impaired biological element is, in fact, the intended effect of a drug, self-compensation can indirectly cancel the desired therapeutic effect.

In neuropathic pain, the pathological behavior is the persistent hyperexcitability leading to unwanted pain sensations. To reduce the excitability of DRG neurons, one could aim to inhibit NaV1.7 channels, but if compensatory changes occur in direct response, such as the upregulation of other sodium conductances and the downregulation of potassium conductances, targeting only NaV1.7 could become futile.

To explore this degeneracy, Ratte et al. investigated the induction of hyperexcitability by varying both sodium and potassium currents [26, 7]. Figure 3.11 shows the resulting *state space*, where different levels of excitability can arise depending on the K and Na currents. This implies that boundaries exist and that there are many ways to cross them. Another study by Xie et al. [27] experimentally demonstrated this feature by modulating NaV currents and inducing equivalent excitability in one sample composed mainly of TTX-S current and another composed mainly of TTX-R current.

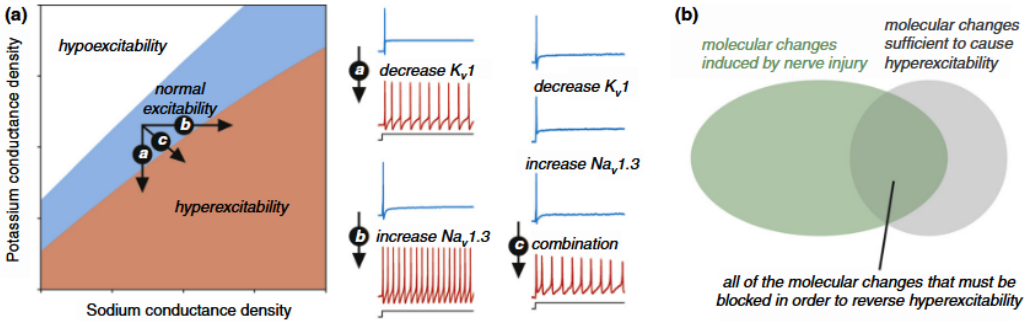

Figure 3.11: Degeneracy of the hyperexcitable state [7]. **(a)** State space showing combinations of potassium (K_V1) and sodium (NaV1.3) conductance densities that yield normal excitability (blue), hypoexcitability (white), or hyperexcitability (red). This state space predicts that a normally excitable cell can become hyperexcitable by decreasing K_V1 (arrow a), increasing NaV1.3 (arrow b), or combining small changes in both (arrow c). **(b)** Venn diagram displaying the set of molecular changes induced by nerve injury (green) and the set sufficient to cause hyperexcitability (grey). The overlap reflects the degeneracy of the hyperexcitable state; all changes within this intersection must be addressed to reliably prevent or reverse hyperexcitability.

Therapeutically, this means that hyperexcitability does not necessarily have to be relieved by focusing specifically on the components that were dysfunctional in the process. Achieving this balance in treatment, however, involves a careful trade-off between drug precision and efficacy. Specific targeting drugs have the advantage of having fewer off-target effects but can be inefficient because they neglect possible adaptive changes that occur in other channels. On the other hand, non-specific drugs could be more efficient but less tolerated because of unwanted side effects. A compromise should be made by combining several specific and/or non-specific drugs to achieve multi-target coverage if needed [7]. To achieve this, a good understanding of the drug's effects is required, which is why a closer look at lidocaine will be presented here.

3.4 Lidocaine

Lidocaine is a channel blocker mainly targeting VGSCs, with additional modulating effects on other targets such as NMDA receptors and potassium channels [28, 29, 30]. In clinical practice, it is primarily used as a local anesthetic, injected locally to block peripheral nerve signals, applied topically (e.g., via patches or gels directly to a specific body surface), or administered intravenously as a systemic analgesic and antiarrhythmic agent [31, 32]. Consequently, lidocaine remains a promising candidate for treating neuropathic pain conditions [33].

3.4.1 Mechanism of action

Lidocaine is a use-dependent blocker, meaning that the intensity of its inhibition depends on the spike frequency. This is due to its high affinity for channels that are open or inactivated, whereas it has a low affinity for those that are closed.

At a low frequency, the time window between spikes is long, and most of this time is spent with channels in the closed state. Each time lidocaine binds to channels during action potential generation, this waiting time leads to the unbinding of all lidocaine molecules from the channels because of their low affinity for the closed state. Consequently, the inhibition cannot accumulate and remains nearly constant. In contrast, at a high frequency, the time window is short, and the blockers remain attached to the ion channels between spikes, leading to an accumulation of blocked channels [34, 28]. This property is well-suited to counteract hyperexcitability while having a smaller impact on normal excitability.

3.4.2 Effect on voltage-gated sodium channels

Although lidocaine inhibition is dynamic and state-dependent, net peak current inhibition provides a practical metric to compare its overall affinity, or at least efficacy, across sodium channel subtypes. Within this framework, inhibition is defined as the percentage reduction in maximal current amplitude, corresponding to a decrease in maximal conductance ($\bar{g}_j$) in conductance-based models. Both TTX-S and TTX-R channels are sensitive to lidocaine, with the TTX-R current being the most affected [35]. Quantitative inhibitions of NaV1.7, NaV1.8, and NaV1.3 are shown in Figure 3.12. NaV1.9 will not be considered because this channel type is not included in the model presented later in this thesis.

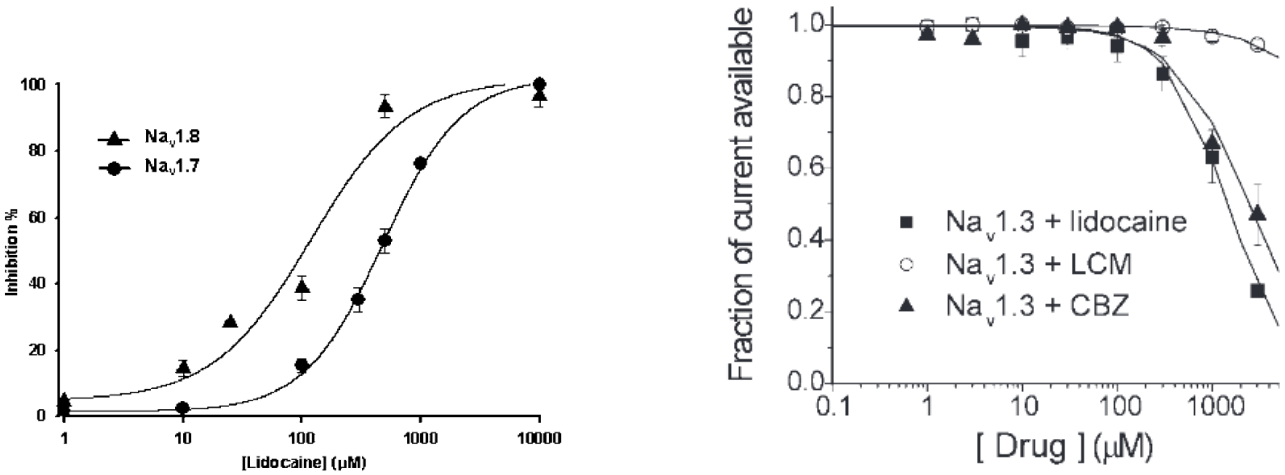

Figure 3.12: Dose-dependent block of NaV1.7 and NaV1.8 currents (left) and NaV1.3 (right) by different lidocaine concentrations. Respectively from [35] and [36].

Lidocaine effects can also be partially explained by looking at the different steady-state curves when lidocaine is present. For both NaV1.7 and NaV1.3, the fast inactivation gates are shifted toward more hyperpolarized potentials, resulting in inactivation at lower potentials. NaV1.8 also exhibits a similar shift in inactivation, but it has an additional shift in fast activation that is not present in the other two channels. This shift of activation, which is toward higher potentials, makes channel activation more difficult, requiring higher potentials to induce channel opening (see Figure 3.13) [35] [36].

These fast-inactivation modulations play a role in low-frequency signals, but they can hardly capture the use-dependent effect, since it mostly takes place on the timescale of a spike. Slow inactivation may help account for this effect, as lidocaine preferentially binds to slow-inactivated states, thereby reducing excitability. Because NaV1.8 appears to enter slow inactivation more rapidly, this aligns with a higher affinity for these states, potentially explaining why it exhibits greater lidocaine sensitivity than TTX-S channels [35, 37, 38].

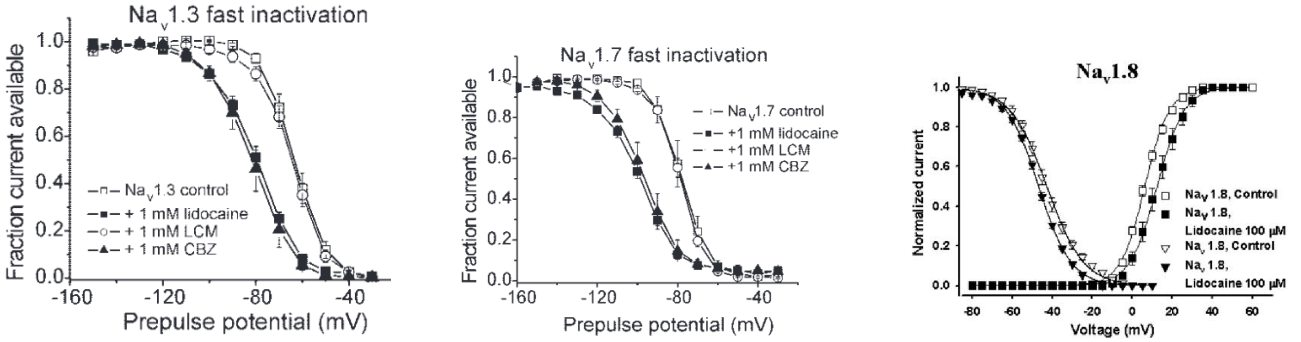

Figure 3.13: **(Left and Middle)** Effect of lidocaine on the fast steady-state inactivation curves of NaV1.3 and NaV1.7 (from [36]). **(Right)** Effect of lidocaine on the steady-state inactivation and steady-state activation curves of NaV1.8 (from [35])

3.4.3 Effect on NMDA receptors

Lidocaine blocks NMDA receptors through several distinct mechanisms. Directly, it exerts a concentration-dependent inhibition on NMDA receptors, though this requires higher concentrations than those needed to block voltage-gated sodium channels [39, 40] (Figure 3.14). Indirectly, lidocaine suppresses NMDAR-induced phosphorylation by inhibiting extracellular signal-regulated kinase (ERK), one of the key enzymes in this pathway [41]. Additionally, it reduces presynaptic glutamate release [28, 42]. Beyond NMDA receptors, lidocaine's analgesic effects in the dorsal horn may also involve interactions with other targets, such as voltage-gated calcium channels [43].

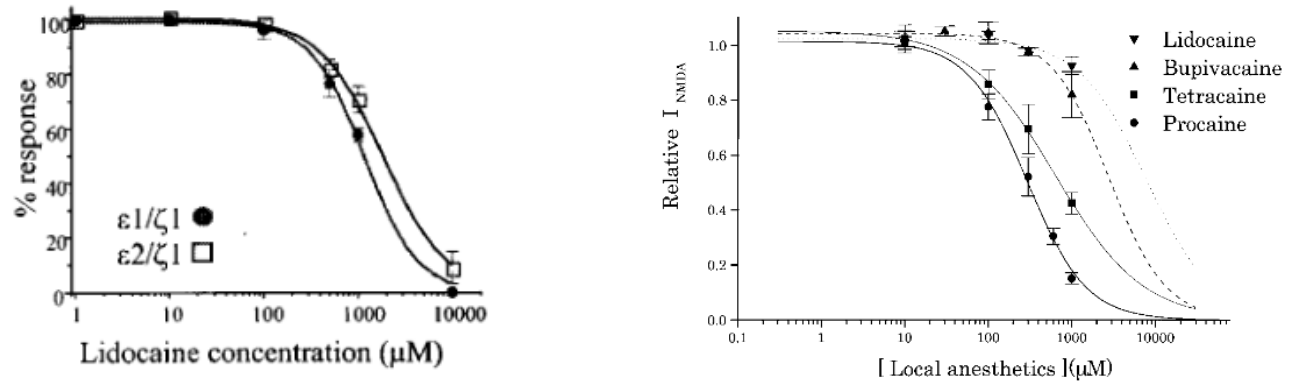

Figure 3.14: Effect of the local anesthetic lidocaine on NMDA receptor currents. **(left)** Data from [40], $\epsilon 1/\zeta 1$ and $\epsilon 2/\zeta 1$ correspond to NMDA receptor subunit families that are widely expressed in the brain. **(right)** Data from [39].

Part II

Computational model

Chapter 4

Model of a DRG neuron connected to a projection neuron

To explore the direct and indirect impacts of ion channel modulation, a three-component conductance-based model was used. The first two components represent the neurons: a dorsal root ganglion neuron (DRGN) and a projection neuron (PrjN). The third component is the synaptic interface connecting the two cells. The following sections describe each component independently, concluding with a detailed account of the specific modulations evaluated.

4.1 The first component: the dorsal root ganglion neuron

The DRGN model was established by Yu-Feng Xie et al. [27] to reproduce experimental data from cultured small rat DRG neurons across various combinations of VGSCs.

4.1.1 The context of the model

Cell cultures enable the preservation of living cells while conducting experiments or applying treatments. These cells are maintained in vitro (in a vessel outside the body), where they proliferate over time while undergoing either self-induced or targeted modulations.

In the study by Xie et al., DRG neurons were evaluated 2–8 hours post-dissociation (DIV0) and after 4–7 days in culture (DIV4–7). Between these time points, the cells undergo developmental shifts that alter their VGSC profiles. At DIV0, the sodium current is dominated by TTX-R channels (NaV1.8), with negligible contributions from TTX-S channels (NaV1.7 and NaV1.3). Conversely, by DIV4–7, TTX-S currents predominate. The authors note that this transition from DIV0 to DIV4–7 mirrors the shift from a healthy to an inflamed state, characterized notably by the upregulation of NaV1.3, which is absent under baseline healthy conditions.

4.1.2 Considered ion channels

The ionic current can be divided into seven conductances, where the currents $I_{NaV1.3}$, $I_{NaV1.7}$, and $I_{NaV1.8}$ respectively correspond to the physiological currents induced by the NaV1.3, NaV1.7, and NaV1.8 VGSCs. Except for I_{K_M}, which corresponds to potassium M-channels, the potassium and leak currents represent phenomenological currents rather than specific ion channel subtypes. For $I_{K_{dr}}$, "dr" stands for "delayed rectifier," as these currents rectify the sodium current with a delay to drive repolarization. $I_{K_{AHP}}$ stands for "afterhyperpolarization," acting primarily on the inter-spike interval rather than spike generation itself.

$$I_{ion} = I_{NaV1.3} + I_{NaV1.7} + I_{NaV1.8} + I_{K_{dr}} + I_{K_M} + I_{K_{AHP}} + I_{Leak}$$

Gate functions

During action potential generation, sodium currents activate at depolarized voltages to drive the upstroke, then inactivate as potassium currents activate to produce repolarization. The orchestration of these stages is governed by the distinct dynamics reflected in the steady-state gating functions ($p_{i,\infty}(V)$) and their corresponding time constants ($\tau_i(V)$), shown in Figure 4.1.

The depolarization phase begins when the voltage reaches the onsets of the sodium activation curves at depolarized potentials, where shorter time constants, $\tau(V)$, within the -60 to 0 mV range enable rapid activation that drives the potential toward higher values.

At these higher voltages, the processes driving the repolarization phase are rapidly established. Although potassium gates activate around -30 mV and the NaV steady-state inactivation curve is already at zero at this potential, their kinetics remain limited by larger time constants. However, these time constants decrease drastically above 0 mV, triggering rapid potassium activation and sodium channel inactivation that initiate the voltage downstroke. Subsequently, the larger time constant values that initially delayed this transition now sustain the voltage downstroke, preventing the repolarization mechanisms from extinguishing before reaching hyperpolarized values. Finally, the decline in $\tau_K(V)$ near -90 mV allows the potassium current to decay, bringing the afterhyperpolarization phase to an end. + On the other hand, K_{AHP} is characterized by slow kinetics and a high activation threshold. It activates primarily during action potentials and decays slowly, providing a small, residual outward current that persists well after spike termination.

As detailed in subsection 3.2.1, NaV1.7 features a low activation threshold and fast inactivation at high potentials, concentrating most of its activation during early depolarization. In comparison, NaV1.8 has a higher activation threshold and slower inactivation kinetics at depolarized potentials, making its primary contribution during the peak upstroke. NaV1.3 plays a role similar to NaV1.7 but exhibits a depolarized shift in steady-state inactivation, producing a more persistent current.

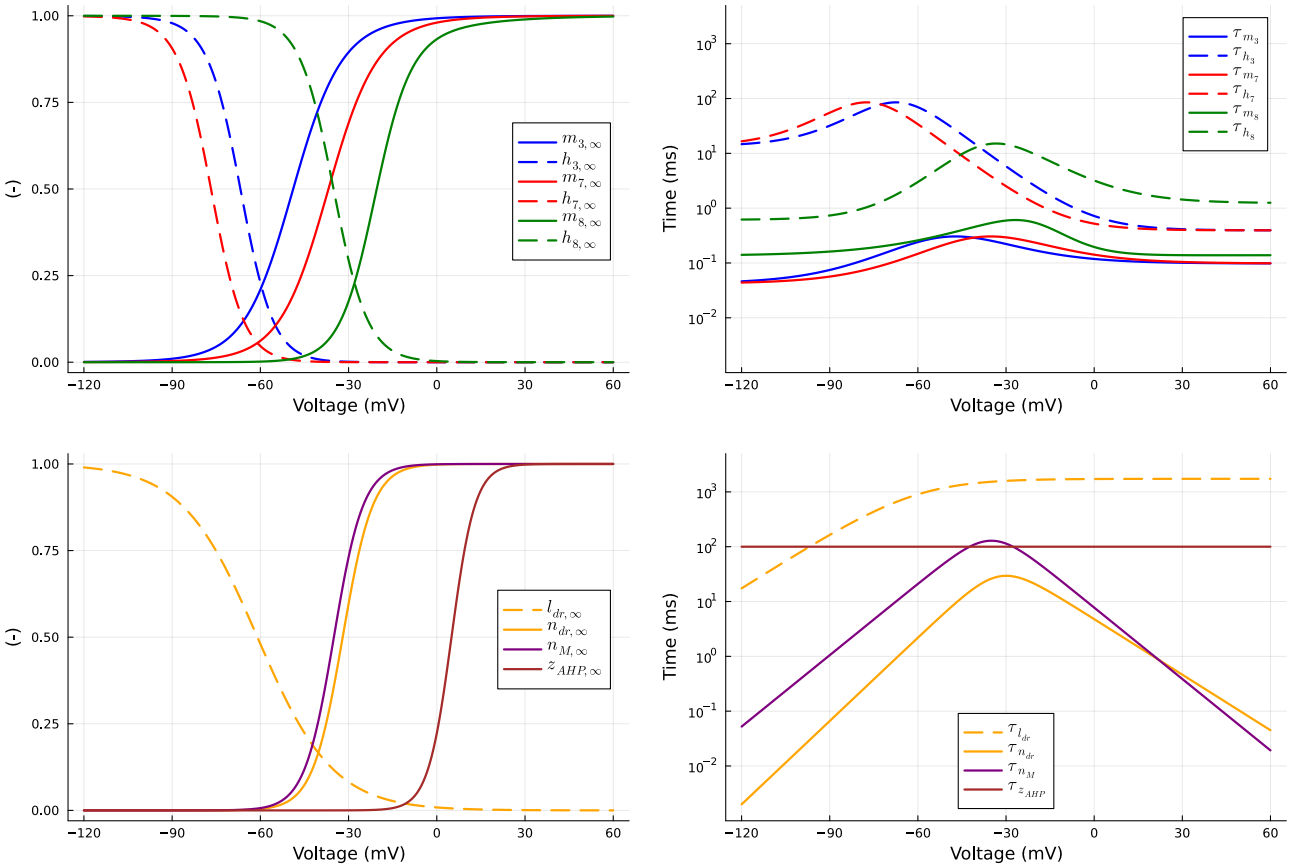

Figure 4.1: DRG neuron steady-state gating variables (left) and time constants (right) for sodium (top) and potassium (bottom) channels, with activation variables represented by solid lines and inactivation variables by dashed lines.

Origins of gate functions

Although all gating functions were implemented as described in [27], their original derivations were inspected. The NaV1.7 gating dynamics were derived from rat DRG neurons [44], whereas those for NaV1.3 were adapted directly from the NaV1.7 formulation. The NaV1.8 gating functions were characterized in rat DRG neurons by [45]. Although the K_{dr} functions are attributed to [46], the equations actually implemented in the model differ from that reference. The origins of the remaining potassium currents are unspecified and are assumed to be introduced by Yu-Feng Xie et al. The complete set of mathematical expressions for all gating functions is provided in section 10.1.

4.1.3 Two sets of parameters

Dividing the model into two experimental contexts (DIV0 and DIV4-7) yielded two distinct parameter sets. DIV0 features high $g_{NaV1.8}$, low $g_{NaV1.7}$, and zero $g_{NaV1.3}$, whereas DIV4-7 features low $g_{NaV1.8}$, high $g_{NaV1.7}$, and non-zero $g_{NaV1.3}$. The leak and K_M conductances also vary, both being larger in DIV4-7 (by up to a factor of 10 for g_{K_M}). Because the model was fitted to experimental data, parameters for cell radius (r) and specific membrane capacitance (C_r) were incorporated to reflect morphological changes in culture over time. All parameter values are listed in Table 10.1 and match those of the original model.

No noise consideration

In the original model, noise was included to enhance realism and align the simulation more closely with experimental data. For this study, however, noise was removed to ensure deterministic behavior and facilitate the reproducibility of results across a large number of simulations incorporating distinct modulations.

4.1.4 Simulation example

Figure 4.2 shows the evolution of the gating variables during single spike generation. Regarding the sodium current, it can be seen that NaV1.3 and NaV1.7 activate earlier than NaV1.8, contributing to the ramp current, whereas NaV1.8 contributes to the upstroke. At the end of the upstroke, sodium inactivation and potassium activation vary much faster due to the decrease in their time constants (τ) within this voltage range, leading to the downstroke. The difference between DIV0 and DIV4-7 will be further analyzed in the following section. Nevertheless, the difference in potassium conductance can clearly be seen: since the DIV4-7 potassium conductance is greater, less recruitment is needed to drive the repolarization.

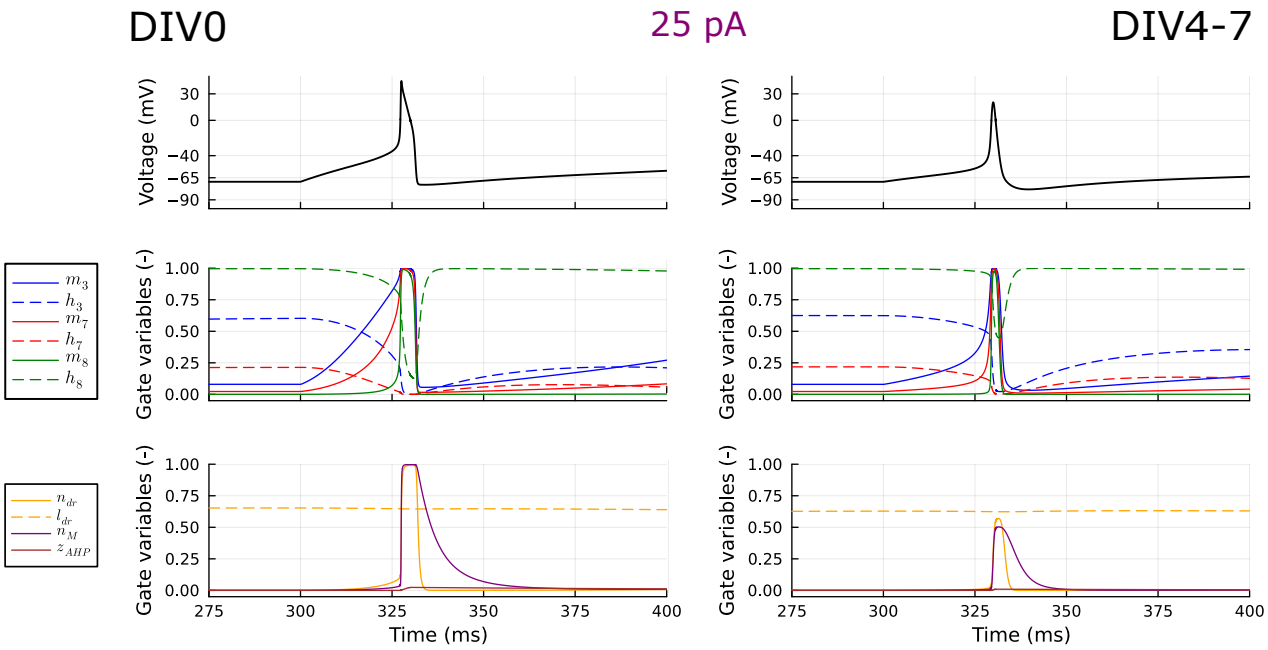

Figure 4.2: Simulation of a single spike at DIV0 and DIV4-7, showing the voltage and gating variable traces. The stimulation is a step current starting at 300 ms, with an amplitude of 25 pA.

4.2 The second component: the projection neuron

The PrjN model is adapted from Anaëlle De Worm et al. [47], who investigated how bistability can emerge and switch through the interaction between calcium and potassium channels.

4.2.1 Considered ion channels

The model incorporates five distinct ionic currents. The sodium (I_{Na}), delayed rectifier potassium ($I_{K_{dr}}$), inward rectifier potassium ($I_{K_{ir}}$), and leak (I_{Leak}) currents are phenomenological and do not directly correspond to specific biological channel subtypes. In contrast, the calcium current $I_{Ca_{Ls}}$ stems from L-type calcium channels, where "s" indicates the slow kinetics of the current.

$$I_{ion} = I_{Na} + I_{K_{dr}} + I_{K_{ir}} + I_{Ca_{Ls}} + I_{Leak}$$

In fact, the implemented model includes I_{K_M} and $I_{Ca_{Lf}}$ currents, as detailed in the Appendix. However, because their conductances/permeabilities were set to zero ($g_{K_M} = 0$ and $p_{Ca_{Lf}} = 0.0$), these currents had no functional impact and are not considered further in the main text. All parameter values and gating functions are provided in section 10.2.

Gate functions

Figure 4.3 illustrates the gating dynamics. The Na and K_{dr} channels activate at similar potentials, with the delay between depolarization and repolarization governed by the difference between $\tau_{m_{Na}}$ and both $\tau_{h_{Na}}$ and $\tau_{m_{dr}}$. Additionally, K_{ir} is active at hyperpolarized potentials, driving the final phase of repolarization and hyperpolarization. Because it does not fully deactivate at the resting membrane potential, it provides a persistent outward current that must be overcome to reach the spike threshold.

The Ca_{Ls} gating variables operate on a significantly slower timescale than those of the other currents. Given that the stimulation protocols in this work typically last 2000 ms, the inactivation variable remains nearly constant, staying largely in its deinactivated state. However, its activation variable varies dynamically, activating at membrane potentials between −40 and 0 mV to influence both depolarization and repolarization. The magnitude and nature of this influence depend directly on the intracellular calcium dynamics.

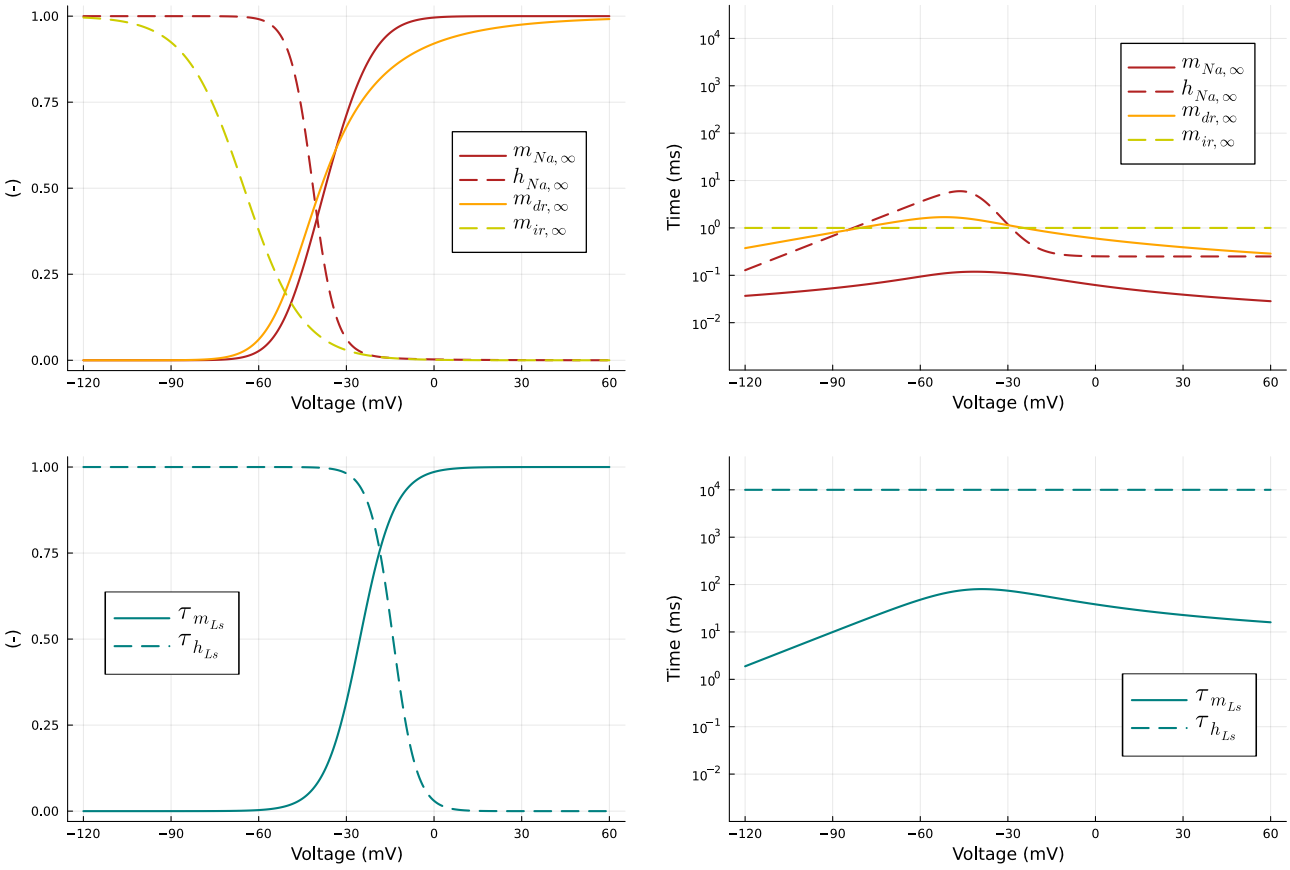

Figure 4.3: Projection neuron steady-state gating variables (left) and time constants (right) for calcium-independent (top) and calcium-dependent (bottom) channels, with activation variables represented by solid lines and inactivation variables by dashed lines.

4.2.2 Calcium dynamics

In the projection neuron, calcium dynamics are modeled by introducing an additional variable, $[Ca^{2+}]_i$, representing the intracellular calcium concentration. Its temporal evolution is governed by:

$$\frac{d[Ca^{2+}]_i}{dt} = \underbrace{-10^7 \times \frac{I_{Ca}}{10^3} \times \frac{1}{2Fd}}_{\text{Inward/Outward current}} - \underbrace{\frac{\left([Ca^{2+}]_i - [Ca^{2+}]_{i,0}\right)}{\tau_{Ca}}}_{\text{Leak}},$$

where F is the Faraday constant, d is depth of the shell beneath the membrane, τ_{Ca} is the calcium removal time constant, and $[Ca^{2+}]_{i,0}$ is the initial and baseline intracellular calcium concentration. The first term represents the concentration changes resulting from calcium influx through calcium channels ($I_{Ca} = I_{Ca_{Ls}}$). The second term functions as a clearance mechanism that continuously drives $[Ca^{2+}]_i$ back toward its resting baseline level (analogous to I_{leak} for membrane potential).

Having established the mechanism of calcium regulation, it remains essential to examine its influence on the membrane potential. This coupling arises from the formulation of the calcium currents via the Goldman–Hodgkin–Katz (GHK) formalism, where the term GHK$(V, [Ca^{2+}]_i)$ enters the expression for the calcium current:

$$I_{Ca_{Ls}} = p_{Ca_{Ls}}\, m_{Ls}\, h_{Ls}\, \text{GHK}(V, [Ca^{2+}]_i) \times 1000$$

In comparison to the canonical ionic current formulation ($I_{ion} = g\, n^i\, m^j\, (V - E)$), the parameter $p_{Ca_{Ls}}$ can be interpreted as the permeability-based analogue of conductance g (in cm/s), while the function GHK$(V, [Ca^{2+}]_i)$ serves as the analogue of the driving force $(V - E)$. The factor of 1000 converts the current density from mA/cm^2 to μA/cm^2, ensuring consistency with the other ionic currents.

While $p_{Ca_{Ls}}$ is a constant parameter, GHK$(V, [Ca^{2+}]_i)$ depends on both V and $[Ca^{2+}]_i$, along with fixed parameters such as the extracellular calcium concentration ($[Ca^{2+}]_o$), which is assumed to remain constant at 2 mM; the complete expression of GHK is provided in section 10.2.

Figure 4.4 illustrates the profile of this function: at low intracellular calcium concentrations (below 0.1 mM), GHK remains strictly negative, causing the calcium current to act purely as a depolarizing influx. At higher calcium concentrations (above 0.1 mM), the function transitions to positive values at potentials above 0 mV while maintaining comparable values at hyperpolarized potentials. As a result, the calcium current becomes repolarizing at higher voltages.In summary, at low calcium levels, the current contributes solely to depolarization, whereas at elevated calcium levels, it contributes to both depolarization and repolarization, ultimately accelerating spike generation.

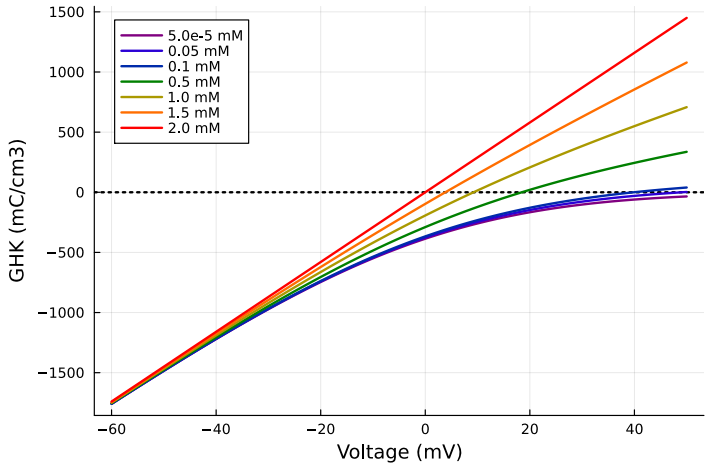

Figure 4.4: Voltage dependence of GHK$(V, [Ca^{2+}]_i)$ across various constant levels of intracellular calcium.

4.2.3 Simulation example

Figure 4.5 shows the traces of the different gating variables. The long simulation allows for observation of calcium accumulation due to its dynamics, and illustrates that the m_{Ls} slow kinetics elevate the firing frequency during stimulation. It also confirms that h_{Ls} remains in the deinactivated state.

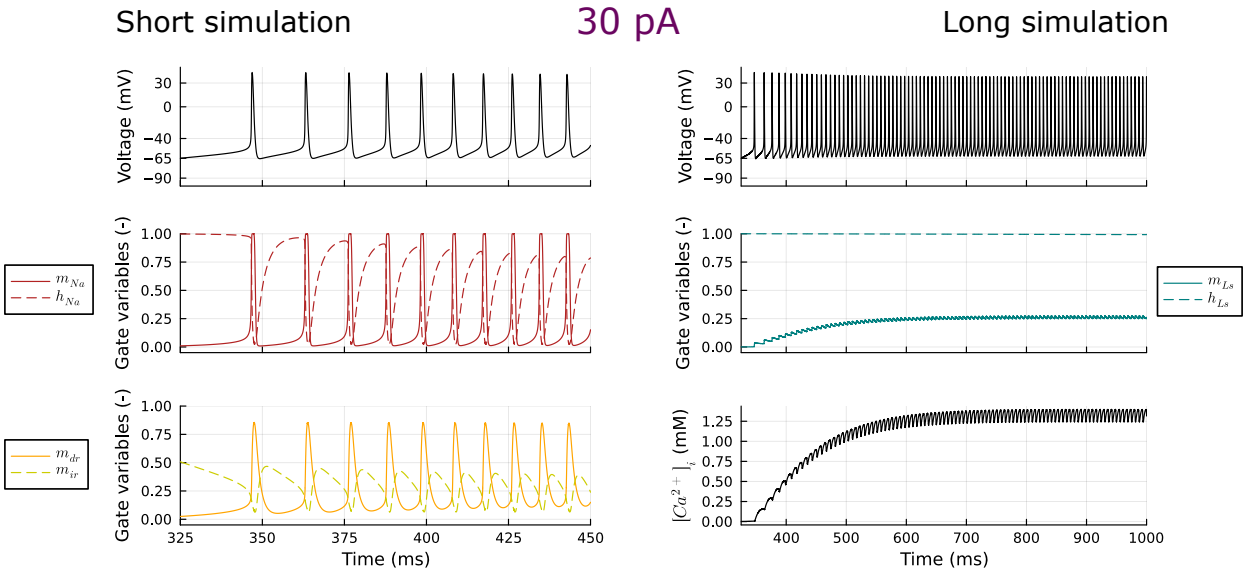

Figure 4.5: Simulations of the projection neuron with a stimulation starting at 300 ms with an amplitude of 30 pA. The simulations on the left and right are performed with the same parameters; the difference lies in which variables are shown and the total duration of the simulation.

4.3 The third component: the synapse

This section of the model originates from Aguiar et al. [22], who identified key mechanisms underlying windup generation by modeling NMDA receptors with L-Type calcium channels.

4.3.1 AMPAR and NMDAR response

Unlike the ion channels described previously, AMPA (AMPAR) and NMDA (NMDAR) receptors are not modeled using traditional gating variables. Instead, to capture their activation in response to afferent inputs, their conductance dynamics are described by dual-exponential kinetics with rise time constants τ_{rise} and decay time constants τ_{decay}. These state variables continuously decay over time and undergo a discrete step increase upon the arrival of an incoming spike. The dynamics of these two variables (A and B) are expressed as follows (where i represents either $NMDA$ or $AMPA$):

$$\tau_{rise,i}\,\frac{dA_i}{dt} = -A_i + S(t)\;R_i$$
$$\tau_{decay,i}\,\frac{dB_i}{dt} = -B_i + S(t)\;R_i(t)$$
$$S(t) = \sum_n \delta([t + delay] - t_n).$$

where $\delta(x)$ evaluates to 1 at $x = 0$ and 0 elsewhere, and t_n represents the arrival times of the afferent spikes. Thus, $S(t)$ equals 1 at each time point $t = t_n + delay$, where $delay$ accounts for synaptic transmission latency.

$R_i(t)$ represents the postsynaptic response to afferent spikes. This response depends on two state variables, $U_{SE,i}$ and P_i, which represent the amount of resources utilized and the probability of vesicle availability for release at time t, respectively. The parameters τ_{fac} and τ_{rec} are the time constants for facilitation and recovery. The dynamics of these variables and the expression for $R_i(t)$ are given by:

$$\begin{aligned} \tau_{fac,i} \frac{dU_{SE,i}}{dt} &= -U_{SE,i} + S_i(t)\,[U_{1,i}\,(1 - U_{SE,i})] \\ \tau_{rec,i} \frac{dP_i}{dt} &= (1 - P_i) - S_i(t)\,[U_{SE,i}\,P_i] \\ R_i(t) = R_i(U_{SE,i}, P_i) &= w_i\; fact_i\,[U_{SE,i}\,P_i]. \end{aligned}$$

The parameters w_i represent the synaptic weights, and $fact_i$ is a normalization factor ensuring that the maximum possible response amplitude depends solely on w_i, while the instantaneous synaptic strength is modulated by the product $U_{SE,i}P_i$. The parameter $U_{1,i}$ is a baseline constant that sets the step increase in $U_{SE,i}$. All parameter values and mathematical expressions are provided in section 10.3.

4.3.2 Distinction between AMPAR and NMDAR

In contrast to AMPA receptors, NMDA receptors are blocked by extracellular magnesium and permit calcium influx into the cell. In the model, the Mg^{2+} block is implemented as a voltage-dependent multiplicative factor in the current expression, whereas the calcium influx is accounted for by defining a fixed fraction of the total NMDAR current as a calcium current.

$$\begin{aligned} I_{AMDA} &= (B_{AMPA} - A_{AMPA})\; g_{AMPA}\,(V - E_{AMPA}) \\ I_{NMDA} &= (B_{AMPA} - A_{AMPA})\; g_{AMPA}\,(V - E_{AMPA})\; Mg_{Block}(V) \\ I_{Ca\,from\,syn} &= I_{NMDA} \times ratio \end{aligned}$$

4.3.3 Connection with the projection neuron

The connection to the projection neuron is made by incorporating the synaptic current ($I_{syn} = I_{NMDA} + I_{AMPA}$) into the total ionic current of the projection neuron. Similarly, the contribution of calcium is accounted for by adding $I_{Ca\,from\,syn}$ to I_{Ca}. The connection from the DRG neuron to the synapse is governed by $S(t)$, which depends on when spikes occur in the DRG neuron (Figure 4.6).

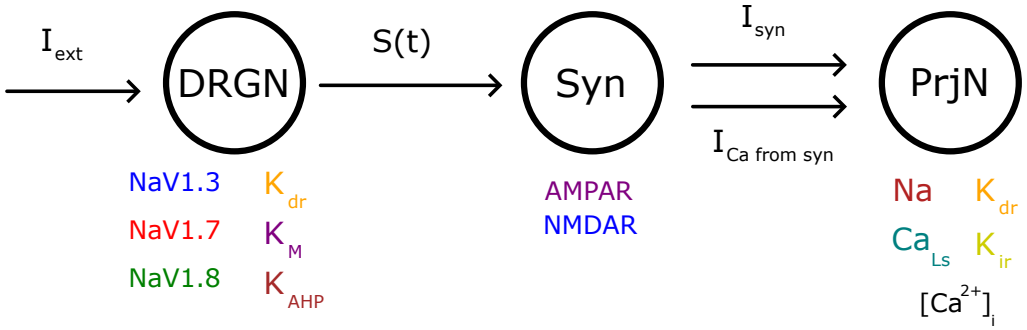

Figure 4.6: Model schematic, illustrating the distinct channels present in each component and the elements connecting them.

4.3.4 Simulation example

In Figure 4.7, AMPAR conductance briefly increases with each spike, allowing it to contribute to the ramp current driving the projection neuron toward threshold. In contrast, NMDAR conductance accumulates between spikes, leading to a greater response in which two spikes are induced. Another difference stems from the Mg^{2+} block of NMDAR, making its conductance voltage-dependent: it increases with the ramp current and reaches its peak during the spike.

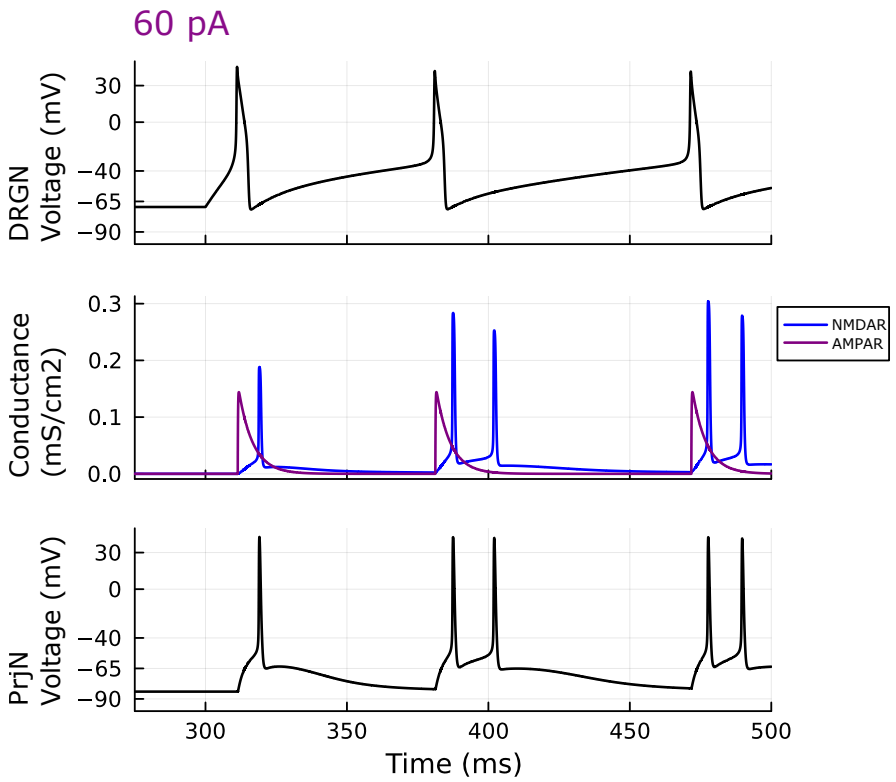

Figure 4.7: Simulation showing NMDAR and AMPAR conductance in response to several afferent spikes driving the projection neuron response.

4.4 Experimental protocol

The purpose of the experimental protocol is to investigate which specific effects of lidocaine alter neuronal excitability. These effects encompass the various inhibitions and steady-state shifts detailed in section 3.4. Rather than incorporating these values directly into the model, qualitative analyses of individual effects will be conducted independently, followed by combinations of these effects. Among these combinations, the specific set corresponding to the actual action of lidocaine will be highlighted.

Practically, the inhibition effect of lidocaine corresponds to a direct reduction in the maximum conductance ($\bar{g}_j$) of the channel; for example, an inhibition of 0.3 corresponds to a loss of 30% of the maximum conductance. Meanwhile, its steady-state gate shift effect is applied by adding an offset term to its expression, where the value is always set as positive, but the shift is toward lower potentials for inactivation and toward higher potentials for activation.

4.4.1 Highlighted lidocaine effect

To properly assess the effects of lidocaine, these parameters must first be estimated. These estimates, derived from the literature, are presented below and provided in full detail in section 10.4.

Inhibition

The inhibition curves (Figure 4.8) correspond to those presented in section 3.4. Because these curves are fitted to experimental data, they do not strictly converge to 0% inhibition at zero lidocaine concentration. To ensure consistency in the computational model at 0 μM, these fitted functions are bypassed and replaced directly with 0% inhibition.

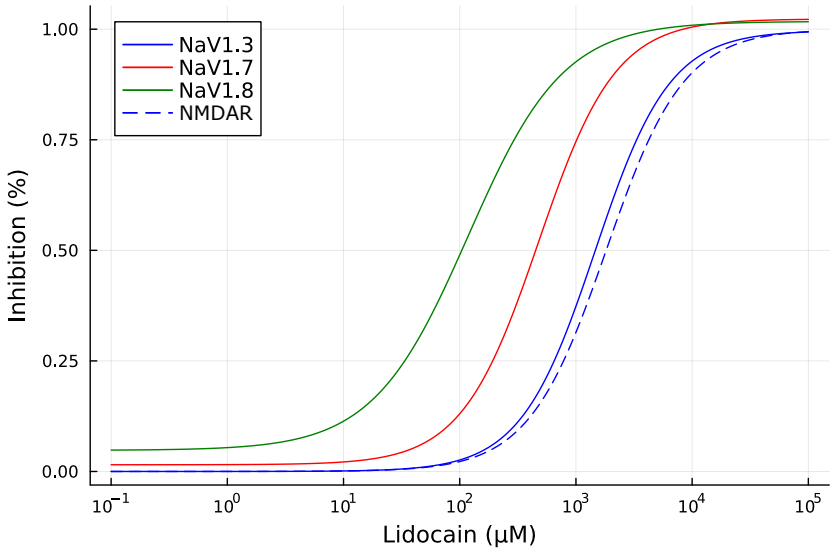

Figure 4.8: Inhibition curve of NaV channels depending on lidocaine concentration. NaV1.7 and NaV1.8 data come from rat DRG neurons [35]. NaV1.3 data also come from rats [36]. NMDAR data come from mice [39].

Shift

To generate the shift versus lidocaine curves (Figure 4.9), fitting was performed using arbitrary points (assuming no shift at low concentrations and specified values at higher concentrations) alongside literature-derived values (black points). Because the limited number of data points does not yield a unique fitted solution, these curves must be interpreted with caution. Based on reported values [35], the activation shift of NaV1.7 was considered negligible, and the shift for NaV1.3 was likewise assumed to be negligible.

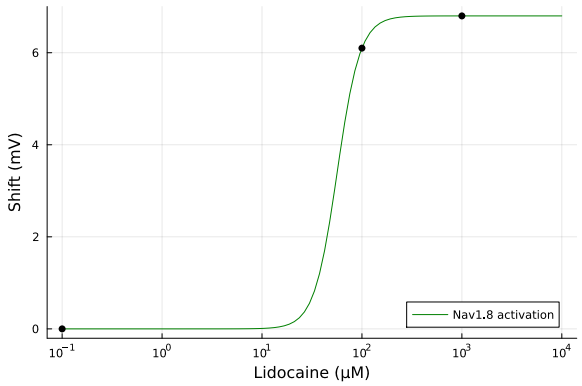

(a) Shift of NaV1.8 activation as a function of lidocaine concentration. The value at 100 μM comes from [35], and the other added points are arbitrary.

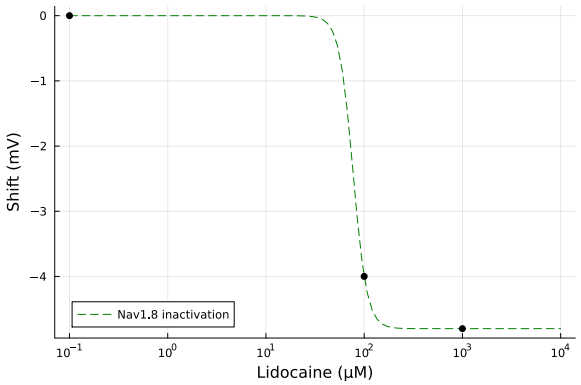

(b) Shift of NaV1.8 inactivation as a function of lidocaine concentration. The value at 100 μM comes from [35], the value at 1000 μM from [36], and the other added point is arbitrary.

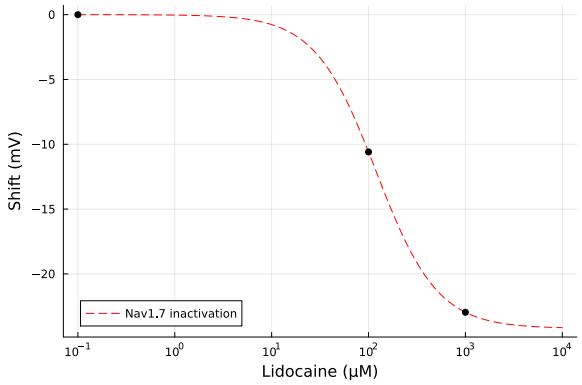

(c) Shift of NaV1.7 inactivation as a function of lidocaine concentration. The value at 100 μM comes from [35], the value at 1000 μM from [36], and the other added point is arbitrary.

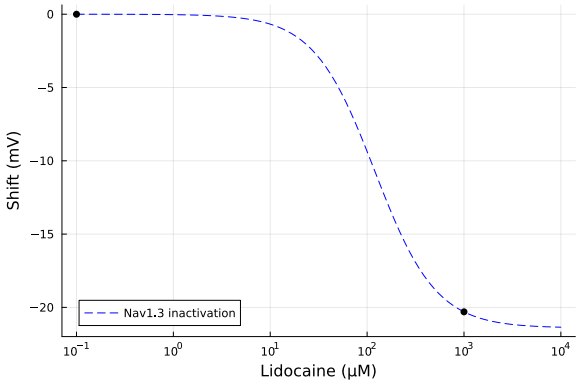

(d) Shift of NaV1.3 inactivation as a function of lidocaine concentration. Two values were found at 1000 μM from [36] and [48], around -20 mV, and the other added point is arbitrary. The estimated slope from Figure 4.9c was reused in this fitting to compensate for the missing 100 μM value.

Figure 4.9

4.4.2 Typical simulation

The simulations are conducted using a constant step current applied from 300 ms to 1700 ms, with the total simulation duration lasting until 2000 ms. The stimulation amplitude varies and is indicated in the respective figures. Any deviations from this standard protocol are explicitly highlighted where applicable.

The various tools and methodologies applied to compute key metrics, such as frequencies and firing pattern estimates, are detailed in section 10.5.

Part III

Computational experiments

Chapter 5

Unmodulated model analyses

To evaluate the consequences of these modulations, establishing a baseline with the unmodulated model is essential. This chapter analyzes the baseline model, beginning with the DRG neuron model focused on NaV channels, followed by the projection neuron focused on synaptic receptor connections and how NMDAR and Ca_{Ls} dynamics impact excitability.

5.1 The role of NaV channels in the DRG neuron

The role of NaV channels is studied across two characteristics of excitability: single-spike initiation and the overall firing pattern. For single-spike initiation, the primary metric is the rheobase (the minimum input current amplitude required to elicit a spike), whereas for the overall firing pattern, the focus is on the emergence of sustained firing.

5.1.1 Initiation of the first spike

Before analyzing spike initiation, it is worth considering cases where no spike occurs despite the presence of an external current. This occurs when the external current fails to depolarize the membrane potential to the sodium activation threshold. More specifically, for a maintained input current, one might expect a spike to eventually occur given sufficient time, as the inward current induces a positive voltage derivative that should ultimately drive the potential to threshold. However, this is not the case; if the resulting ramp current is too slow, the slow dynamics of potassium activation have sufficient time to operate, generating an opposing outward current. Consequently, the net voltage derivative becomes zero, driving the neuron into a new equilibrium state despite the ongoing current.

With the DIV0 parameter set, nearly all sodium current is carried by $I_{NaV1.8}$, which activates around -40 mV. The ramp current required to reach this NaV1.8 threshold must be provided by both the external input current (I_{ext}) and the NaV1.7 current ($I_{NaV1.7}$) (Figure 5.1).

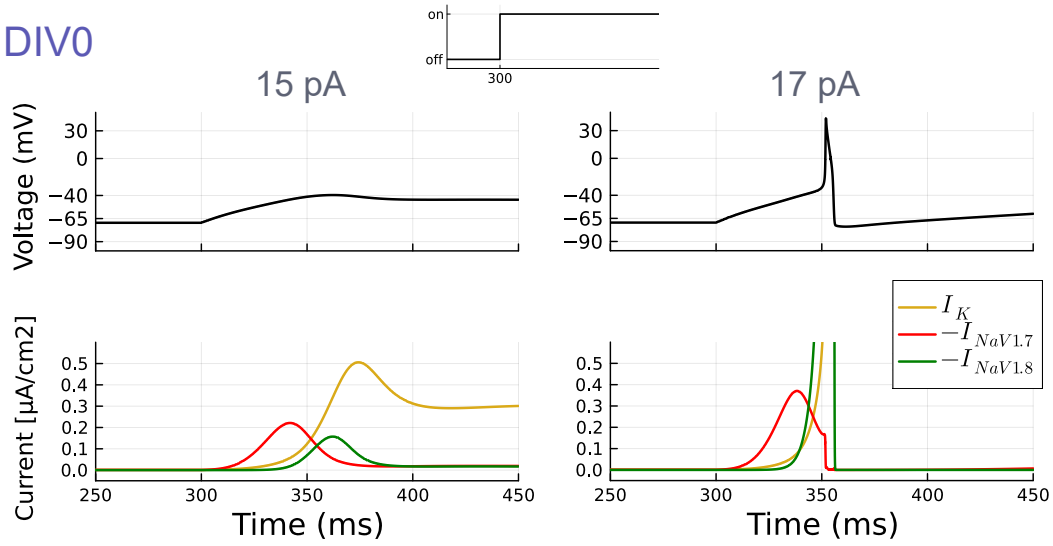

Figure 5.1: DIV0 behavior before and after the rheobase. Simulation with a step current applied at 300 ms, showing a current amplitude just below the rheobase **(Left)** and just above it **(Right)**. The NaV1.7 current operates primarily during the ramp phase, whereas NaV1.8 is mainly responsible for the spike upstroke. Note that opposite values of the sodium current are shown to facilitate the comparison with potassium currents.

In comparison, DIV4-7 possesses lower-threshold sodium currents (NaV1.3 and NaV1.7), making the ramp current less dependent on external input and thereby reducing the rheobase. However, the smaller NaV1.8 current means the spike upstroke is primarily driven by the NaV1.7 current. Because NaV1.7 inactivates at lower potentials, the sodium current could be insufficient to fully drive depolarization. This results in a reduced spike amplitude with a rounded waveform rather than a sharp action potential, where spike detection occurs simply because this peak exceeds the 0 mV detection threshold. To produce a more pronounced all-or-nothing event, $g_{NaV1.8}$ could be increased to approach a state similar to DIV0. Alternatively, increasing $g_{NaV1.3}$ or $g_{NaV1.7}$ would accelerate the ramp current, leaving less time for repolarization mechanisms to engage (Figure 5.2).

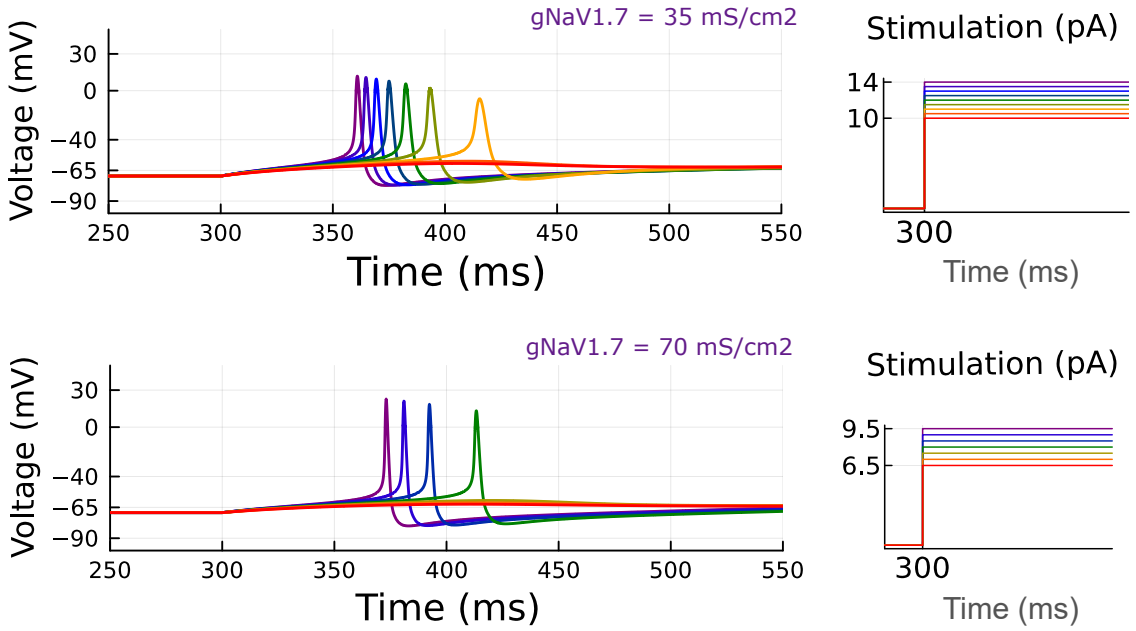

Figure 5.2: DIV4-7 rounded waveforms crossing the spike detection threshold, where sodium current compensation restores sharp spike shapes. Simulations with increasing input current amplitudes in steps of 0.5 pA (minimum and maximum amplitudes shown on the right). **(Top)** With default parameters for DIV4-7, increasing stimulation leads to a gradual rise in bump amplitude until reaching the detection threshold. **(Bottom)** DIV4-7 with a two-fold increase in $g_{NaV1.7}$, which enables rapid depolarization via the sodium current. This eliminates the smooth transition between non-spiking and spiking responses, leaving subthreshold (non-spiking) traces as completely flat curves.

5.1.2 Initiation of spiking

Eliciting an initial action potential does not guarantee sustained spiking due to the slow kinetics of potassium currents, specifically K_{AHP} activation and K_{dr} inactivation. While these slow mechanisms have negligible impact on the first spike, once they are activated, they can suppress subsequent action potentials. However, because the stimulation is a step current, I_{ext} persists after the first spike. In DIV0, this constant depolarization eventually helps the membrane potential overcome the potassium currents to reach the NaV1.8 activation threshold before its inactivation, ultimately enabling sustained spiking (Figure 5.3).

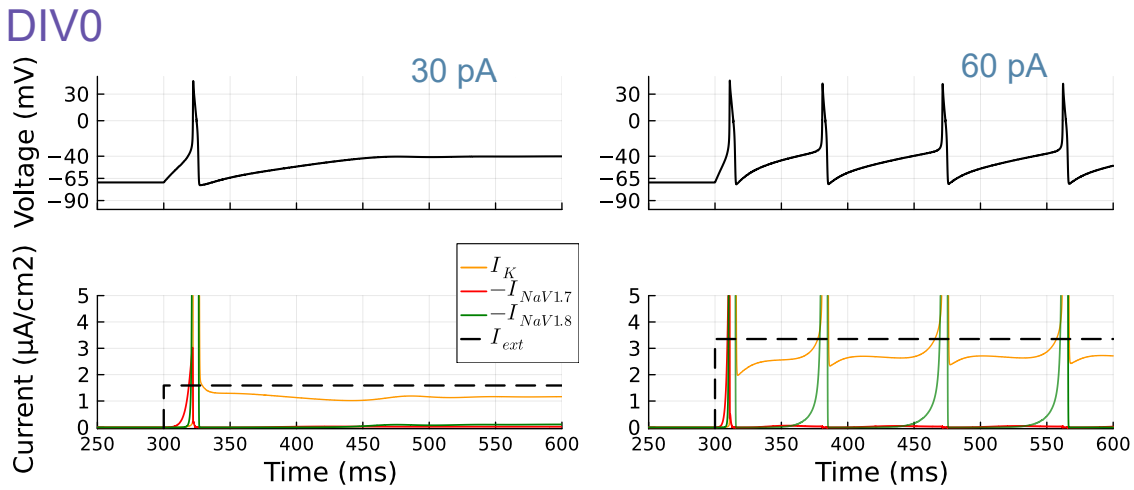

Figure 5.3: Spiking generation in DIV0. **(Left)** Absence of continuous spiking despite the emergence of an initial spike, caused by potassium currents. **(Right)** Emergence of spiking under a sufficiently high input current that counteracts the potassium currents. Note that the opposite of the sodium current is shown to enable comparison with potassium ones.

Under the original configuration from Xie [27], DIV4-7 neurons never exhibit sustained spiking and display only transient responses because the total sodium current is insufficient. Spiking can be restored, however, by upregulating any one of these sodium conductances (Figure 5.4).

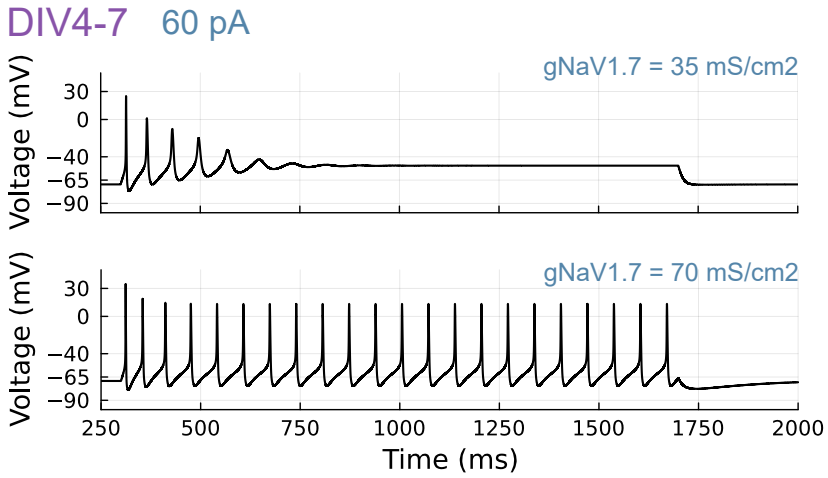

Figure 5.4: Spike generation in DIV4-7. **(Top)** Spiking never occurs at default DIV4-7 conductances, resulting in transient a firing pattern. **(Bottom)** Doubling the NaV1.7 conductance induces the emergence of repetitive spiking.

Although both TTX-S and TTX-R currents can drive spiking, the contribution of the TTX-S current becomes limited at high input currents. Indeed, Figure 5.5 shows that spiking stops for DIV4–7 at higher current values. This decline occurs because the strong input current drives the steady-state membrane potential to a highly depolarized level. At this elevated equilibrium potential, the TTX-S channels undergo complete, continuous inactivation, leading to a loss of firing. In contrast, because $Na_V1.8$ inactivation occurs at significantly more depolarized potentials, it can still support action potentials under these conditions, showing that $Na_V1.8$ is better suited to sustain spiking at high input currents. Regarding Figure 5.3, it can be seen that aside from the very first spike, the $Na_V1.7$ current does not participate in the generation of subsequent action potentials.

Given that the leak and K_M currents are higher for DIV4-7, one might assume that the loss of spiking is primarily caused by an excessive potassium current. This hypothesis was tested by applying DIV0 parameters alongside DIV4-7 Na conductances (not shown here). In reality, reducing K_M dampens membrane potential oscillations and accelerates the transition to the equilibrium state.

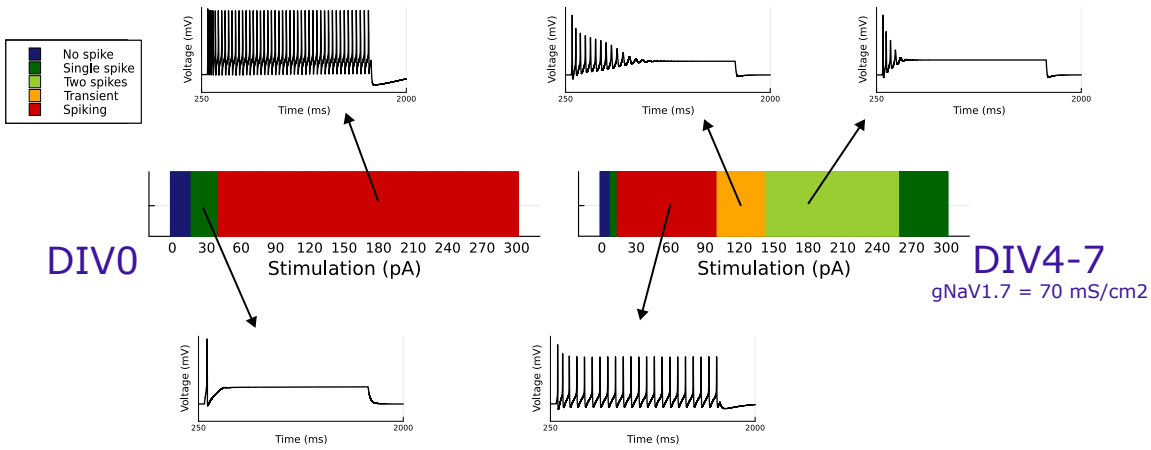

Figure 5.5: Excitability patterns of unmodulated DIV0 and DIV4-7 with doubled $g_{NaV1.7}$. Firing behaviors across different stimulation amplitudes (evaluated in 3 pA steps) are shown, with five simulations highlighted: two for DIV0 (at 60 pA and 180 pA) and three for DIV4-7 (at 60, 120, and 180 pA).

Beyond whether spiking occurs, an impactful metric is the resulting firing frequency. The FI curve illustrates how frequency varies as a function of stimulation amplitude. The displayed frequencies represent the mean instantaneous frequency[1] for each simulation. In DIV0, these frequencies correspond to spiking patterns. However, transient patterns also contain spikes and thus carry an associated frequency.

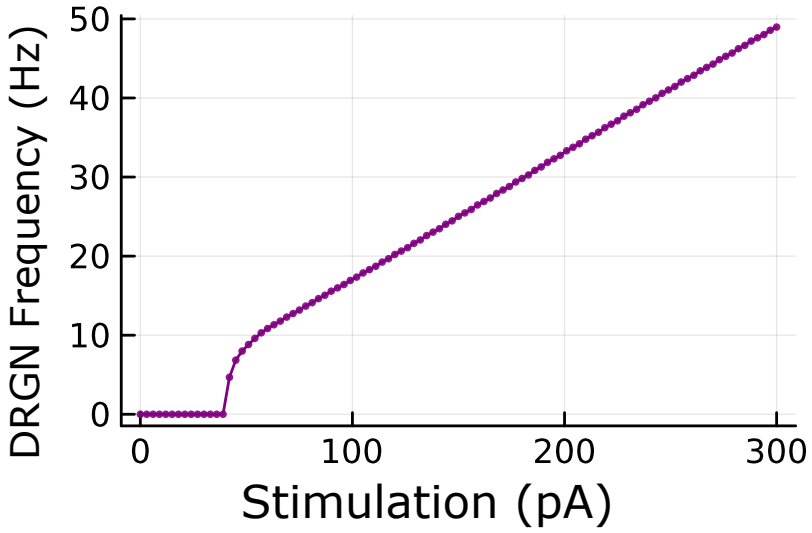

Figure 5.6: FI curve of the DRG neuron.

[1]The instantaneous frequency is the inverse of the inter-spike time interval between consecutive spikes. More details on frequency computation are available in section 10.5

5.2 The role of synaptic receptors in the response of the projection neuron

The following section explores the response of the projection neuron to single afferent spikes and repetitive firing, showing how afferent spiking frequency impacts the wind-up phenomenon induced by NMDA receptors and Ca_{Ls} dynamics. Prior to this, the baseline characteristics of the isolated projection neuron are presented.

5.2.1 Projection neuron in stand-alone

The projection neuron fires at high frequencies, spanning from 150 Hz to over 300 Hz (Figure 5.7). Compared to the DRG neuron, it exhibits a lower input current threshold: an injection of approximately 25 pA suffices to elicit spiking, whereas the DRG neuron requires at least 50 pA. Excessive current injection causes a breakdown in action potential amplitude, where depolarization yields an abnormally low peak voltage and repolarization results in an abnormally high trough voltage. Consequently, the decrease in firing frequency observed around 250 pA in the F–I curve reflects only the frequency of the initial spikes that cross 0 mV, as these are the only ones detected.

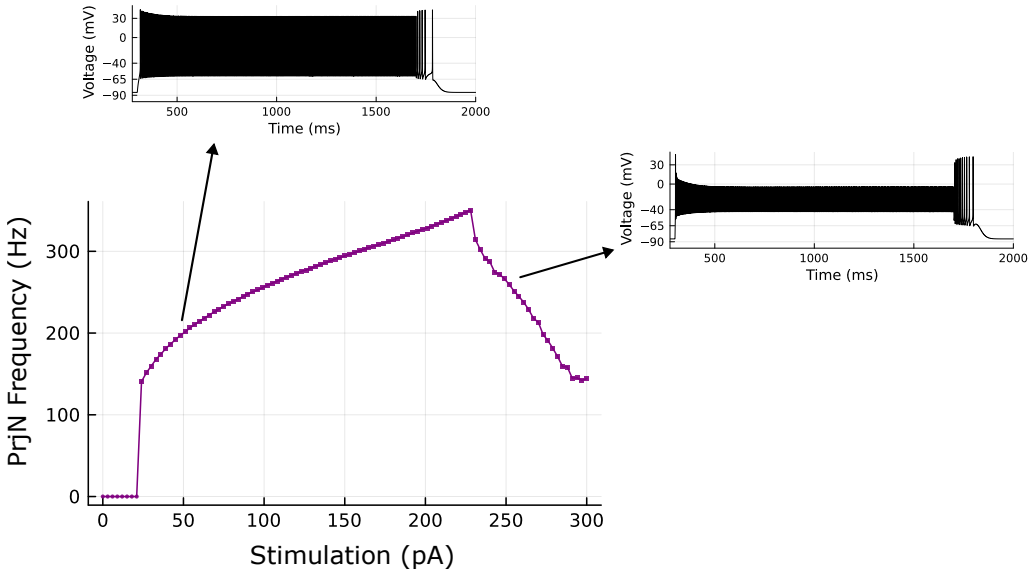

Figure 5.7: The FI curve of the projection neuron and the corresponding voltage dynamics for stimulation amplitudes of 50 pA and 250 pA are shown. Across all simulations, the stimulation pulse is applied from 300 ms to 1700 ms.

5.2.2 The response to a single afferent spike

Because the synaptic current reacts binarily to afferent input, the amplitude of the afferent action potential has no impact on the response.

In this model, a single afferent spike reliably evokes at least one postsynaptic action potential. Driven predominantly by AMPA receptors, the synaptic current provides the necessary depolarization to reach the spike threshold. This current also contributes to both the depolarization and repolarization phases, switching from inward (negative) to outward (positive) as the membrane voltage crosses zero. This behavior stems from the reversal potential of both AMPA and NMDA receptors ($E_{AMPA} = E_{NMDA} = 0$), reflecting the biological reality that these channels are permeable to both sodium and potassium ions. However, while this synaptic current is present during both the upstroke and downstroke, it is not strictly necessary for the action potential itself. This was demonstrated by substituting the synaptic current

with a brief external stimulus that serves solely to drive the membrane potential to threshold, without contributing further to the spike waveform (Figure 5.8).

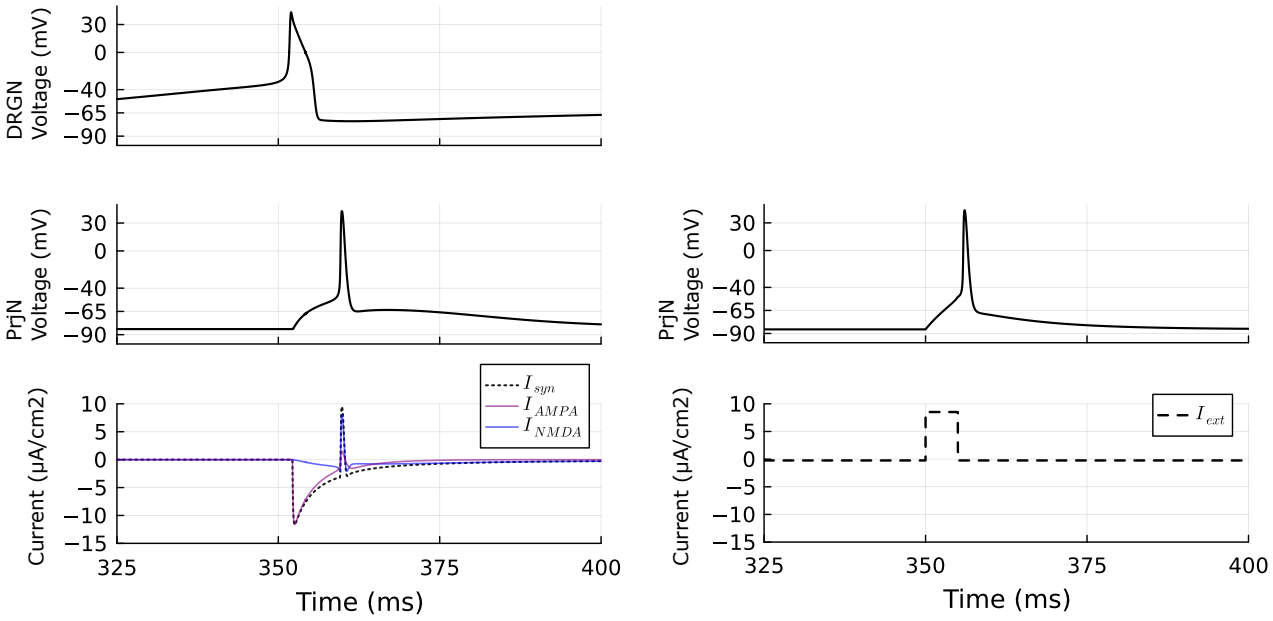

Figure 5.8: Single-spike generation in the projection neuron under afferent synaptic current and external stimulation. **(Left)** Response of the projection neuron to a single-spike afferent input. Top: Voltage trace of the DRG neuron following a 17 pA stimulus. Middle: Voltage trace of the projection neuron. Bottom: Synaptic current acting on the projection neuron. **(Right)** Response of the projection neuron to a short external stimulus (110 pA amplitude, 5 ms duration starting at 350 ms).

5.2.3 The response to afferent spiking

The response of the projection neuron depends nonlinearly on the afferent spiking frequency (Figure 5.9). Overall, the projection neuron fires at a higher frequency than the afferent input and exhibits a sharp increase in firing rate at an afferent frequency above 12 Hz. The elevated firing rate below 12 Hz can be attributed to NMDAR mechanisms, whereas the sharp increase stems from additional Ca_{Ls} activation.

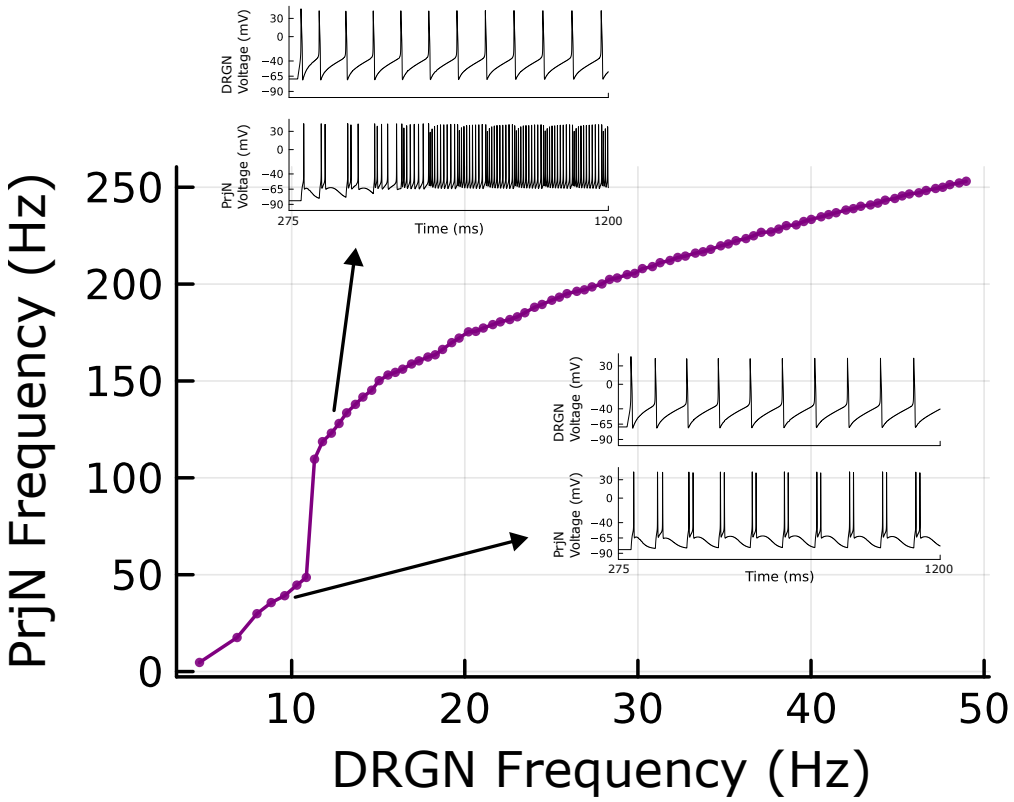

Figure 5.9: Response frequency of the projection neuron as a function of afferent DRG neuron firing frequency.

With ongoing repetitive spiking, the neuronal response amplifies through NMDA receptor dynamics, as illustrated by the heightened NMDAR current following the initial spike. This amplification corresponds to the wind-up phenomenon, an expected feature given that the model is adapted from Aguiar et al. [22]. However, this enhancement occurs only if the afferent spiking frequency is high enough to drive an accumulation of NMDA conductance. In contrast, AMPAR current remains unchanged between successive afferent spikes because AMPAR rapid decay kinetics prevent any accumulation (Figure 5.10).

At a sufficiently high afferent frequency, the postsynaptic response gradually escalates to firing rates exceeding 100 Hz. This amplification stems from Ca_{Ls} channel dynamics, specifically the gradual rise in its activation (m_{Ls}), while the NMDAR current mirrors its behavior from the previous case. Unlike NMDAR activation, which relies entirely on afferent input, Ca_{Ls} activation is intrinsically tied to the projection neuron's own spiking rate. High postsynaptic firing rates progressively open Ca_{Ls} channels, further driving up the response frequency. This creates a positive feedback loop: increased Ca_{Ls} activation boosts firing, which then drives greater Ca_{Ls} activation until the system stabilizes at a high-frequency equilibrium.

Synaptic currents play a critical role in this process. Specifically, the NMDAR response increases, allowing a single afferent spike to elicit a two-spike postsynaptic response and double the induced Ca_{Ls} opening. Furthermore, even after Ca_{Ls} activation is established, synaptic currents continue to amplify the response and remain necessary to sustain firing. Once the stimulation is turned off and DRG neuron inputs are lost, spiking briefly persists due to residual NMDAR and Ca_{Ls} currents before the neuron comes to a complete stop (Figure 5.10).

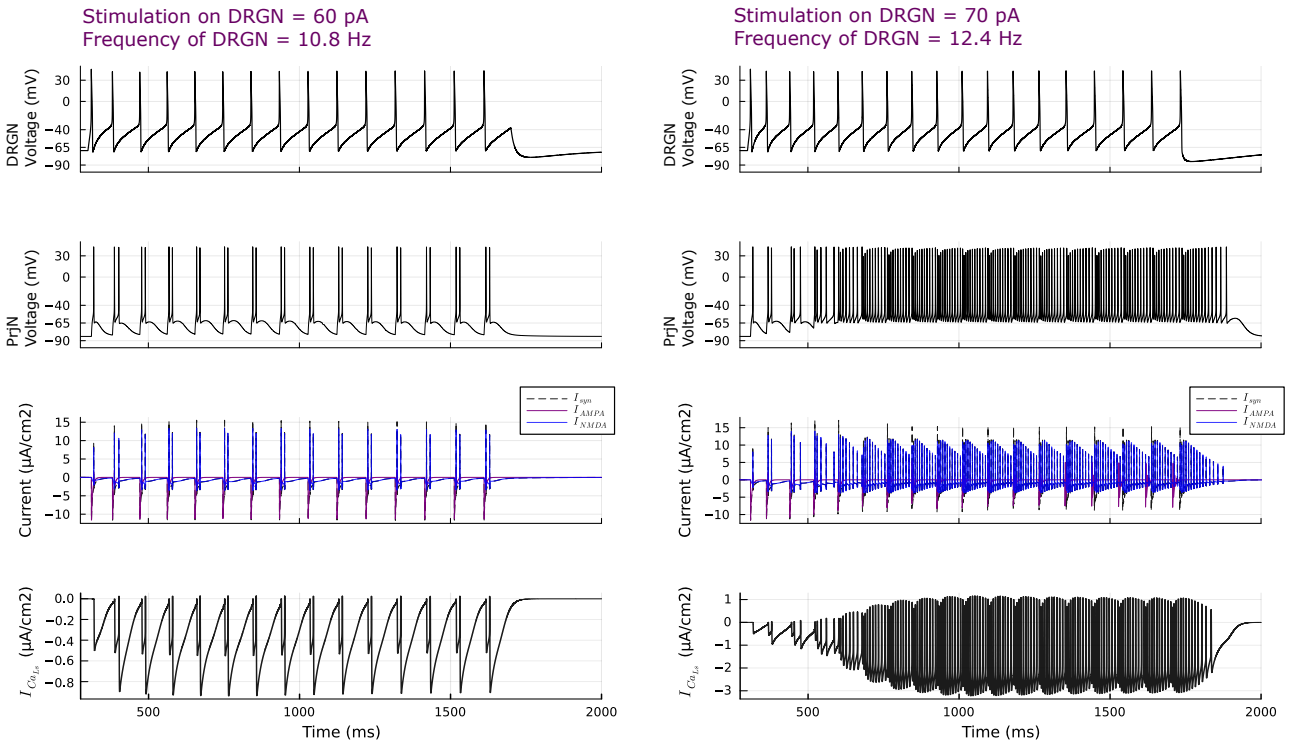

Figure 5.10: Evolution of DRG neuron voltage, projection neuron voltage, synaptic currents, and Ca_{Ls} current in response to a step input current applied to the DRG neuron.

These results visually show a gradual increase in the response frequency, consistent with the findings of [22] shown in Figure 3.7. A pronounced wind-up effect emerges due to the combined presence of NMDAR and Ca_{Ls}, and this phenomenon intensifies as the afferent frequency rises.

However, a key difference lies in the timescale: in the cited article, wind-up occurs over seconds. This discrepancy primarily reflects the input frequency, which was 1 Hz in their study, tenfold lower than the afferent input frequency used here. Since both in the present study and the original one, the NMDAR timescale is in the range of 100 ms, the 10 times higher frequency here allows NMDAR alone to produce a small cumulative effect, although it is significantly smaller than when Ca_{Ls} builds up.

Besides the afferent frequency and time constants, the NMDAR synaptic weight (w_{NMDA}) could help to modulate how fast the accumulation occurs. Increasing w_{NMDA} would cause a single afferent spike to increase the NMDAR conductance more, requiring fewer spikes to reach the same value, while decreasing it produces the opposite effect. Another impact is that if w_{NMDA} is high enough, NMDA could induce a two-spike-to-one response without any accumulation, or even lead to additional spikes if increased further.

Chapter 6

Impact of NaV channel modulations on excitability

In this chapter, qualitative experiments assess how lidocaine-mediated modulation affects DRG neuron excitability, specifically through channel inhibition or steady-state shifts. The analysis focuses primarily on rheobase, the presence or absence of spiking, and the associated firing frequency. This is evaluated on both DIV0 and DIV4-7; however, DIV4–7 is modeled using the original parameter set (with $g_{NaV1.7} = 35$ mS/cm^2) and is therefore limited to rheobase analysis, as spiking does not occur. Finally, the indirect impact of these modulations on the projection neuron response is explored.

6.1 Modulations in DIV0 context

In DIV0, NaV1.8 is the dominating sodium conductance, NaV1.7 is barely present, and NaV1.3 is absent. Consequently, the primary focus is placed on NaV1.8 modulation, though this section begins by briefly considering the loss of NaV1.7.

6.1.1 The impact of NaV1.7 loss

NaV1.7 contributes minimally to the ramp current; consequently, a lower $g_{NaV1.7}$ makes DIV0 more reliant on I_{ext}, which increases its rheobase. NaV1.7 is not strictly necessary, and higher external current can compensate for its complete inhibition Figure 6.1. Furthermore, as previously shown in Figure 5.3, NaV1.7 has a limited impact on sustained firing patterns, and its loss behaves similarly.

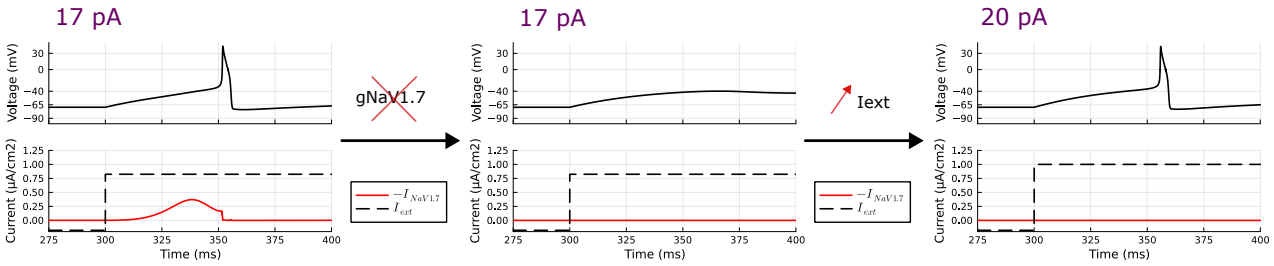

Figure 6.1: Increase in rheobase induced by the loss of NaV1.7 in DIV0. The left of the figure shows the baseline rheobase, followed by the effect of NaV1.7 total inhibition and the subsequent recovery achieved by increasing the external current.

6.1.2 Impact of modulations of NaV1.8 on the rheobase

$g_{NaV1.8}$ inhibition

Inhibition of NaV1.8 channels leads to a progressive, moderate increase in the rheobase up to an inhibition level where sharp action potentials no longer occur, giving way instead to large membrane potential oscillations Figure 6.2.

Action potential amplitude is minimally affected even under high inhibition levels, up to around 70%. Specifically, decreasing the NaV1.8 maximal conductance proportionally reduces the elicited $I_{NaV1.8}$, diminishing its contribution to $\frac{dV}{dt}$. This lowers $\frac{dV}{dt}$ and slows the voltage upstroke. Consequently, reaching the spike peak is still achievable despite the reduced maximal conductance, though the depolarization phase requires more time. Failure occurs when the upstroke becomes excessively slow, allowing repolarizing currents enough time to activate and counteract the depolarization before the peak is reached. Subthreshold oscillations arise when the combined input current and NaV1.7 current produce a ramp fast enough to initiate depolarizing upstrokes, but insufficient to complete fully formed action potentials.

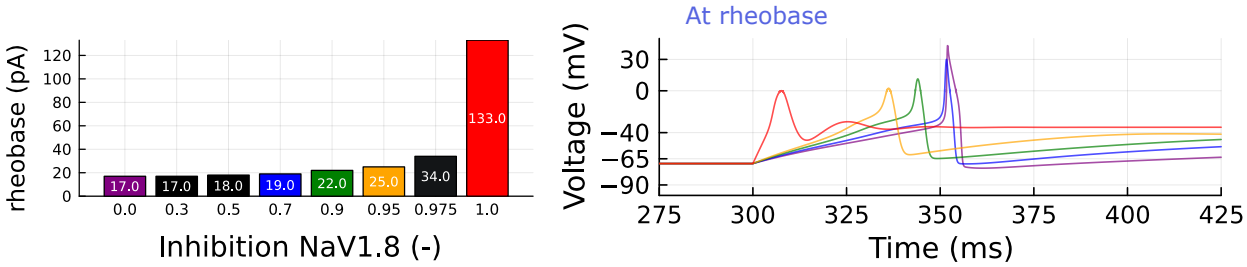

Figure 6.2: Impact of NaV1.8 inhibition on the rheobase. **(Left)** Rheobase values at different inhibition levels, with colors matching the **(Right)** simulations, which were performed using input currents equal to their respective rheobases.

Steady-state gating function shifts

For NaV1.8 channels, shifts occur in both steady-state activation and inactivation. The resulting behavior varies depending on which steady-state gating function is affected.

Moving the inactivation function toward more negative potentials can be interpreted as a mild form of inhibition, provided that the inactivation curve remains above the resting potential. In this situation, inactivation does not have sufficient time to develop before the first spike at stimulation onset, and thus exerts only a limited influence (Figure 6.3). The mild inhibition arises from the reduced h_{8_∞} at the resting potential, which lowers h_8 before stimulation onset.

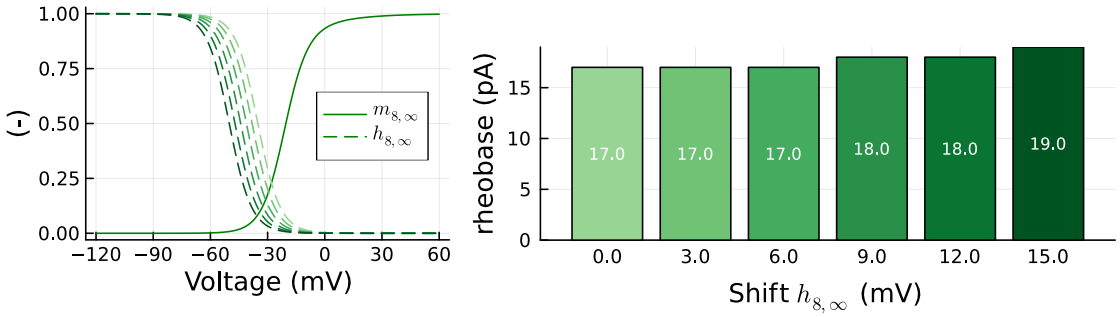

Figure 6.3: Impact of shifting NaV1.8 inactivation on the rheobase. **(Left)** Illustrations of the corresponding shifts. **(Right)** Bar plot showing rheobase values across different shift ranges.

In contrast, shifting the activation function exerts a more pronounced effect (Figure 6.4), raising the NaV1.8 threshold potential required to trigger the spike upstroke. Consequently, a larger input current is necessary to reach this elevated threshold sufficiently quickly. This difference is illustrated in Figure 6.5 by applying the same suprathreshold input current: shifting the activation function delays the action potential upstroke, whereas shifting the inactivation function has no noticeable effect on the spike.

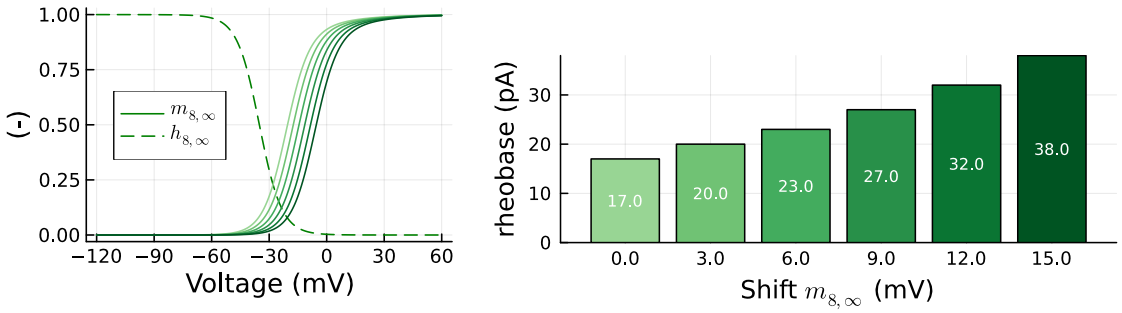

Figure 6.4: Impact of shifting NaV1.8 activation on the rheobase.**(Left)** Illustrations of the corresponding shifts. **(Right)** Bar plot showing rheobase values across different shift ranges.

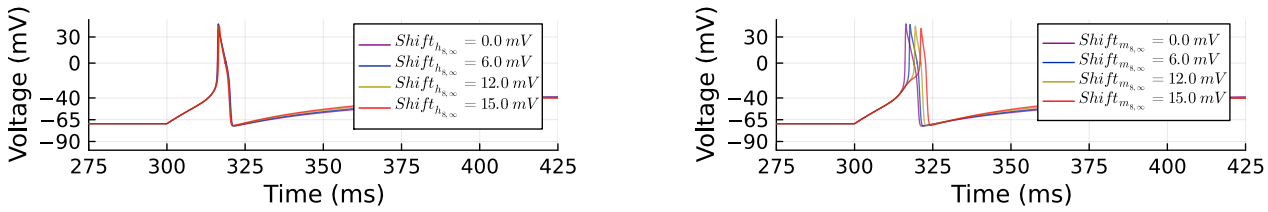

Figure 6.5: Illustration of the impact of different NaV1.8 shifts on first spike generation. Evolution of the voltage for different shift values: **(Left)** inactivation shifts, which have nearly no impact; **(Right)** activation shifts, which lead to a delay in the upstroke. All simulations were performed with an input current of 40 pA.

6.1.3 Impact of NaV1.8 modulations on spiking presence and related firing frequency

$h_{8,\infty}$ shift

Compared with its small effect on the rheobase, shifting the inactivation curve toward lower potentials significantly impacts the generated spiking pattern. This hyperpolarizing shift accelerates inactivation at lower potentials, which in turn speeds up repolarization. Consequently, the depolarization speed must increase, requiring a larger input current to compensate. However, this shift cannot suppress spiking; if the ramp current is fast enough, activation still has enough time to generate the spike depolarization before inactivation occurs, thanks to the different time constants.

It can be observed that the resulting sustained spiking visually differs: the peak amplitude decreases, while the spiking frequency increases (Figure 6.6). This increase in frequency seems counterintuitive, as earlier sodium inactivation would be expected to lead to slower spikes. However, this occurs because once spiking is well established, a lower peak combined with faster repolarization leads to less potassium channel activation. This results in a faster ramp current for the next spike, which reaches the NaV1.8 activation threshold sooner than under control conditions.

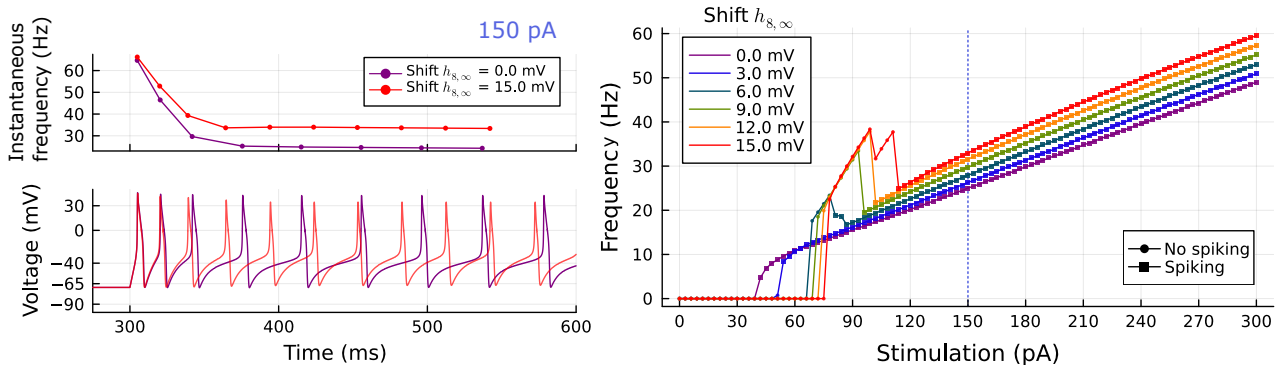

Figure 6.6: Inactivation shifting alters the sustained firing pattern and induces transient patterns. **(Left)** Simulations at 150 pA for a shift value of 15 mV compared to no shift. **(Right)** FI curves of the DRG neuron at different $h_{8,\infty}$ shift values, where increasing the shift increases the stimulation needed for spiking onset while inducing a transient pattern that corresponds to higher frequencies before spiking emerges. The location of the left simulations is highlighted by the vertical dashed line.

Besides the sustained spiking pattern, the disappearance of spiking induced by the shift can result in a transient pattern. On the FI curves, these patterns correspond to the ones before the current allows spiking, where they exhibit a higher frequency despite having only a few spikes. These elevated frequency values arise because the reported frequency reflects the mean of instantaneous frequencies, and spike trains typically begin with a high initial firing rate before settling into a lower, steady-state frequency once sodium and potassium currents reach steady-state kinetics. This initial high-frequency burst is shown in Figure 6.6 and will be further seen in the following results.

NaV1.8 inhibition and $m_{8,\infty}$ shift

Both inhibition and activation shifts can lead to a loss of spiking (Figure 6.7). In both cases, this is caused by a lack of NaV1.8 current, though for different reasons. For inhibition, this stems directly from a decrease in available NaV1.8 current, which becomes insufficient to drive the upstroke. With an activation shift, the NaV1.8 channels fail to activate, yielding no NaV1.8 current. Consequently, when activation does occur in the latter case, the delivered current is not reduced, and the spiking frequency is barely affected. In contrast, smaller peak amplitudes under inhibition lead to a higher frequency, through the same mechanism as the inactivation shift.

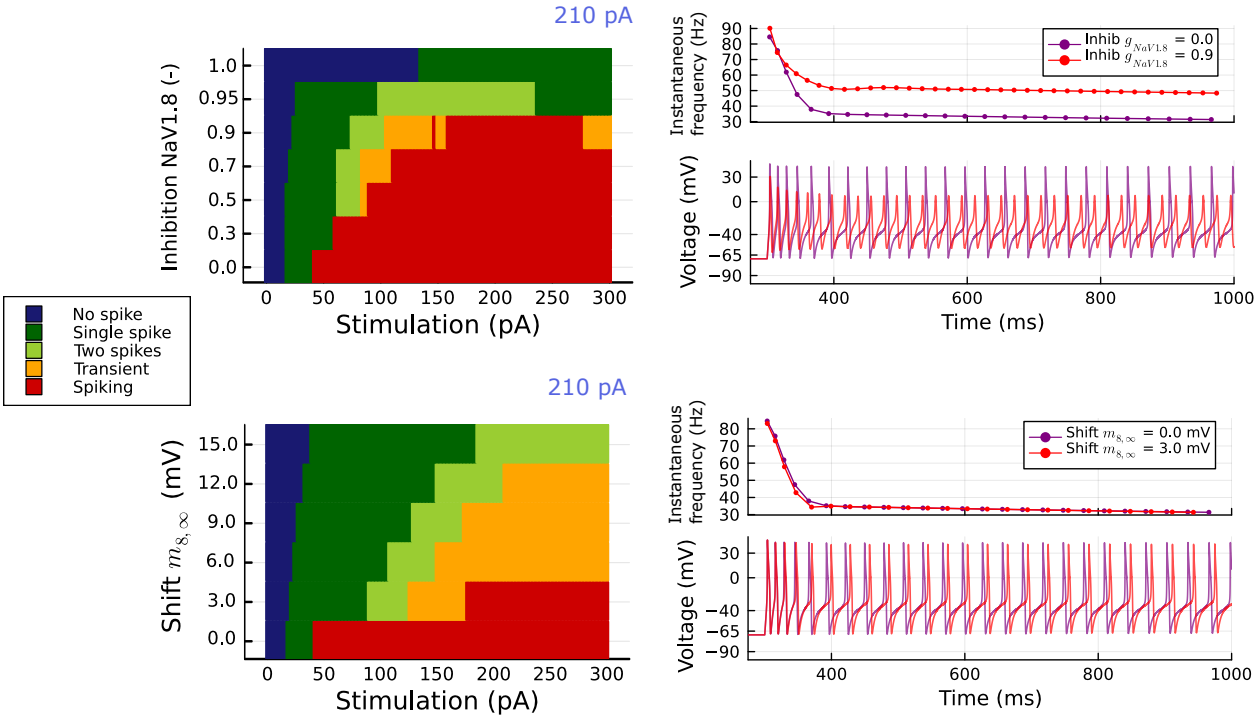

Figure 6.7: Firing patterns under NaV1.8 inhibition and $m_{8,\infty}$ activation shift. **(Top)** Effects of $g_{NaV1.8}$ conductance inhibition. **(Bottom)** Effects of $m_{8,\infty}$ curve shift. **(Left)** Firing pattern as a function of input current stimulation across different modulation values. **(Right)** Voltage traces and instantaneous frequency evolution for representative modulation values.

6.1.4 The combination of lidocaine-induced modulations on NaV1.8

The combined effects of lidocaine are illustrated using heatmaps, where the axes represent two of the previously described modulations. The specific trajectory taken by lidocaine is also depicted, following the curve presented in subsection 4.4.1. Since both NaV1.8 activation and inactivation are shifted by the drug, a fraction of the total shift value applies to either activation or inactivation. The proportion is set to 40% for inactivation and 60% for activation, as this roughly corresponds to the proportion of the lidocaine effect at 100 μM.

Regarding NaV1.8 shifting and inhibition, most of the impact of lidocaine comes from steady-state shifts. The reason is not specifically that lidocaine preferentially affects shifting, but rather that this effect is the most impactful. In Figure 6.8, the rheobase mainly increases along the shift axis; inhibition only takes effect upon reaching a critical threshold, but achieving such inhibition using lidocaine requires a concentration in the range of 1000 μM. A comparison can be made by looking at the modulation value at the 100 μM lidocaine point. Considering 50% inhibition alone (without any shift) leads to a rheobase similar to that at the origin (unmodulated baseline). In contrast, a 10 mV shift alone nearly doubles the rheobase relative to the origin.

As shown in Figure 6.9, 100 μM of lidocaine is sufficient to suppress spiking across all input current conditions. These heatmaps clearly illustrate how channel modulations change firing frequencies, with the lowest non-zero frequency situated at the origin. The highest frequencies correspond to transient firing patterns, even though higher spiking frequencies also appear due to inhibition and inactivation shifting.

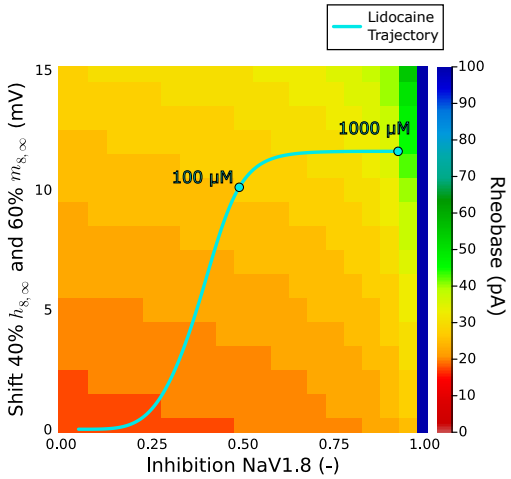

Figure 6.8: Heatmap of the NaV1.8 modulation effect on the rheobase. The colorbar corresponds to different rheobase values, and the cyan curve corresponds to the lidocaine trajectory, where the first and second points correspond to concentrations of 100 and 1000 μM, respectively.

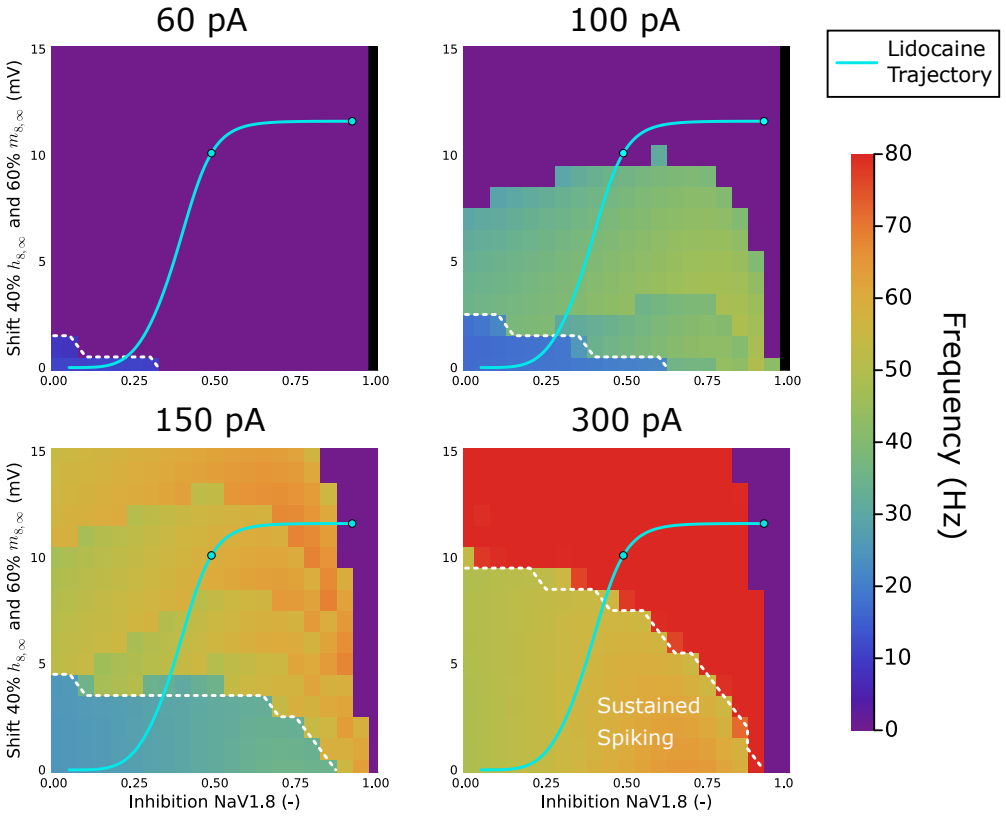

Figure 6.9: Heatmaps of the NaV1.8 modulation effect on frequency under different stimulation amplitudes. The colorbar corresponds to different frequency values of the DRG neuron and is common across all heatmaps; the cyan curve corresponds to the lidocaine trajectory, where the first and second points correspond to concentrations of 100 and 1000 μM, respectively. The white line forms the boundary between the region where continuous spiking occurs (bottom left) and the region where it does not; the non-zero frequency values in this other region originate from transient regimes. The purple corresponds to a frequency of 0 Hz (a single spike), and black to no spike at all.

6.2 Impact of DIV4–7 channel modulations on rheobase

In this section, the original parameter values for DIV4–7 are retained for the subsequent experiments ($g_{NaV1.7} = 35$ mS/cm^2). Because spiking does not occur under these baseline parameters, only the impact on rheobase is examined. Unlike in DIV0, $Na_V1.3$ is present and will be considered. After briefly assessing the contribution of $Na_V1.8$, the individual modulations of $Na_V1.3$ and $Na_V1.7$ will be explored, as well as their combined effects.

6.2.1 The negligible contribution of NaV1.8

NaV1.8 at DIV4–7 has a very small maximal conductance. Its contribution is even smaller than that of NaV1.7 at DIV0. Total loss of NaV1.8 leads to a barely noticeable reduction in spike amplitude, with no impact on the rheobase.

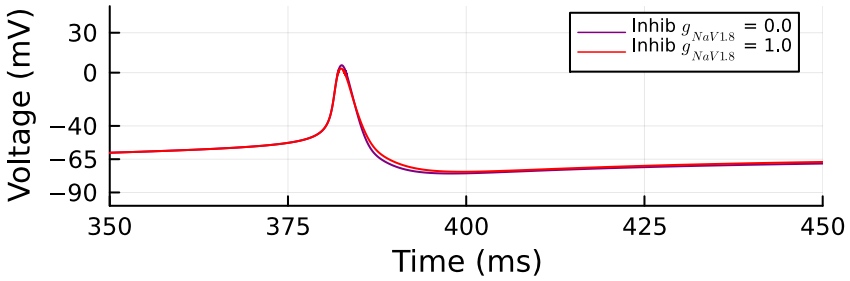

Figure 6.10: Comparison of voltage trace with and without NaV1.8 current at DIV4-7 rheobase (12 pA)

6.2.2 Impact of NaV1.3 modulation

NaV1.3 can be thought of as an input booster that operates close to the resting potential. Inhibiting this channel progressively increases the rheobase by slowing the ramp current, requiring additional input current to compensate for the missing NaV1.3 boost. This can be seen in Figure 6.11, where the same suprathreshold current is given, and those with less NaV1.3 have a delayed spike upstroke. Since NaV1.3 has only a limited impact on the upstroke, its total inhibition does not lead to a loss of spike, as most of the sodium current upstroke is carried by NaV1.7.

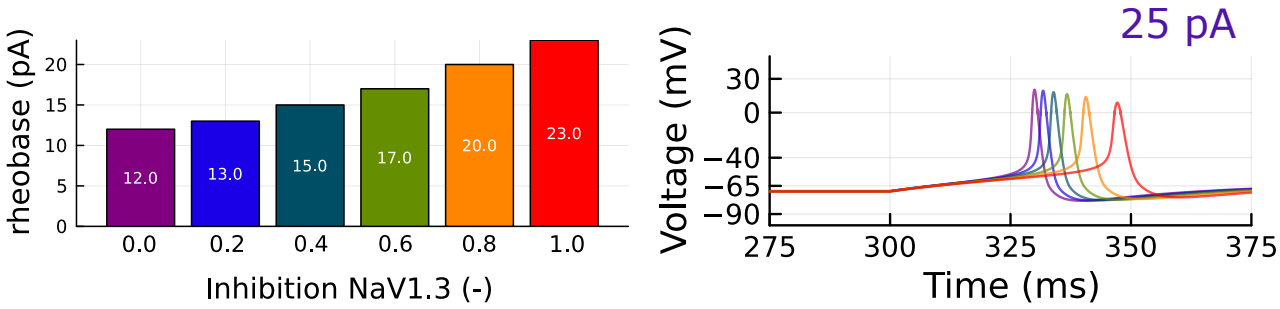

Figure 6.11: Impact of NaV1.3 inhibition on the rheobase. **(Left)** Rheobase values corresponding to different levels of inhibition, with colors matched to the curves on the **(Right)**, which show how this inhibition induces a slowing of the ramp current, ultimately delaying the upstroke.

Unlike NaV1.8 in DIV0, NaV1.3 inactivation shift has a visible effect even on the first spike. This occurs because the NaV1.3 inactivation midpoint is near the resting potential, meaning that shifting the inactivation gate significantly decreases the $h_{3,\infty}$ value at rest. Consequently, h_3 decreases in the same manner during the 300 ms before stimulation, resulting in a progression similar to pure inhibition, where a large shift (22.5 mV) leads to nearly constant inactivation (Figure 6.12).

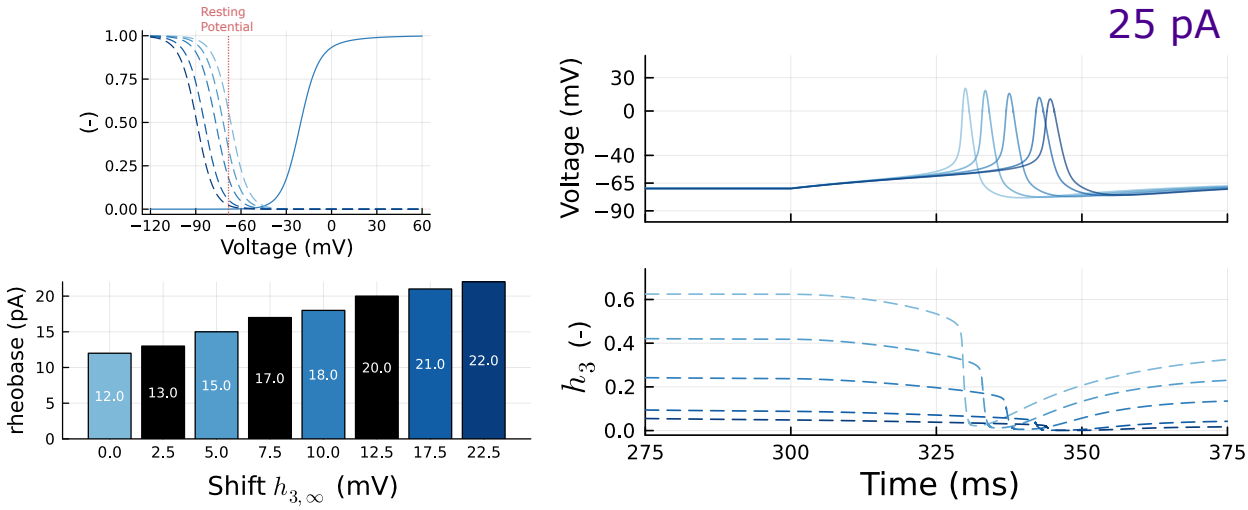

Figure 6.12: Impact of NaV1.3 inactivation shifting on the rheobase. **(Left)** Bar plot showing rheobase variation across different shift values illustrated above, where the black bars represent shifts that are not explicitly shown. **(Right)** Simulations with an input current of 25 pA, displaying voltage evolution above and h_3 gate evolution below.

6.2.3 Impact of NaV1.7 modulation

As with NaV1.8 in DIV0, inhibiting NaV1.7 gradually increases the rheobase up to a critical value. Beyond this value, further inhibition leads to the loss of single spikes and a steep rise in rheobase, culminating in large-amplitude oscillations that reach the peak detection threshold (Figure 6.13). However, this critical threshold is reached for an earlier inhibition value than in DIV0; the primary reason is that potassium currents are significantly larger in DIV4-7, making them harder to overcome when using the stimulation as the primary depolarizing current.

Inactivation shifting of NaV1.7 has an effect similar to inhibition. The reasons are the same as for NaV1.3, with h_7 at the resting potential becoming smaller, directly decreasing NaV1.7 availability (Figure 6.14).

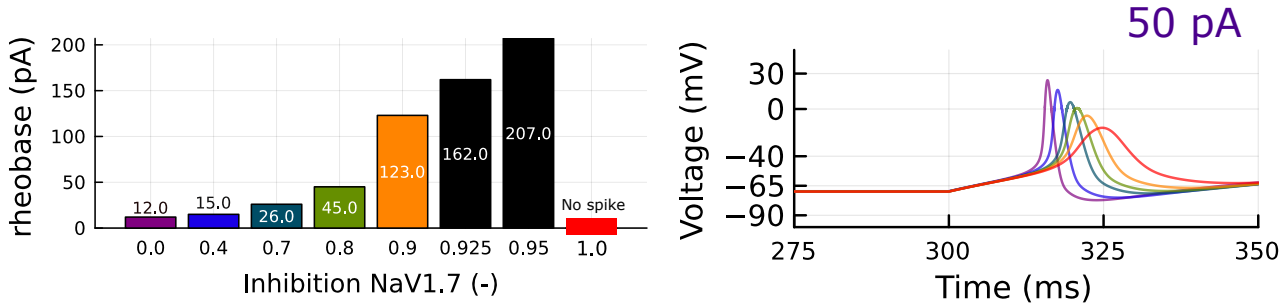

Figure 6.13: Impact of NaV1.7 inhibition on the rheobase. **(Left)** Rheobase values corresponding to different levels of inhibition, with color-coding matching the curves on the **(Right)**, which shows how this inhibition alters the induced spike by decreasing spike amplitude, eventually leading to a rounded subthreshold bump at high inhibition levels.

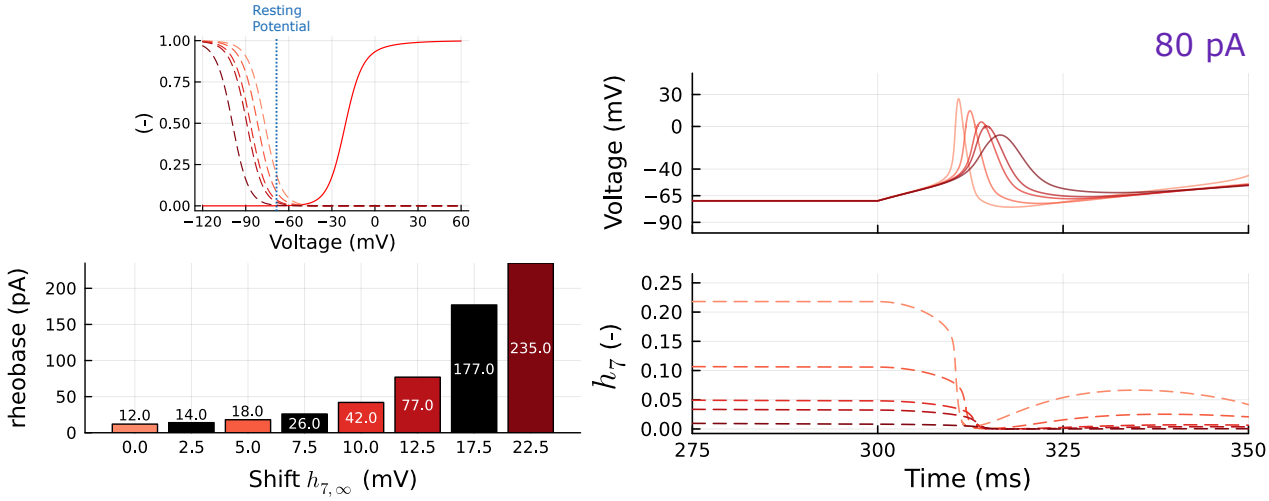

Figure 6.14: Impact of NaV1.7 inactivation shifting on the rheobase. **(Left)** Bar plot showing rheobase variation across different shift values illustrated above, where the black bars represent shifts that are not explicitly shown. **(Right)** Simulations with an input current of 80 pA, displaying voltage evolution above and h_7 gate evolution below.

6.2.4 Combined effect

Because NaV1.7 is the dominant sodium current, modulation of NaV1.7 affects the rheobase the most. Consequently, most of the rheobase variations appear along axes that modulate NaV1.7 (Figure 6.15). Nevertheless, this trend reduces with greater NaV1.7 inhibition; as the NaV1.7 contribution diminishes, the proportion of sodium current coming from NaV1.3 increases, so that inhibition of NaV1.3 induces bigger changes at high levels of NaV1.7 inhibition than at low ones.

Regarding the lidocaine trajectory, lidocaine exerts a stronger modulation on NaV1.8 than on NaV1.7; however, DIV4–7 is more strongly affected. Considering NaV1.7 alone, 100 μM leads to a rheobase of 55 pA, whereas this state is reached in DIV0 at a concentration of 1000 μM. In DIV4-7, a concentration of 1000 μM leads to a loss of spikes [1].

[1] As a reminder, in large input current, the detected spike corresponds to a large oscillation.

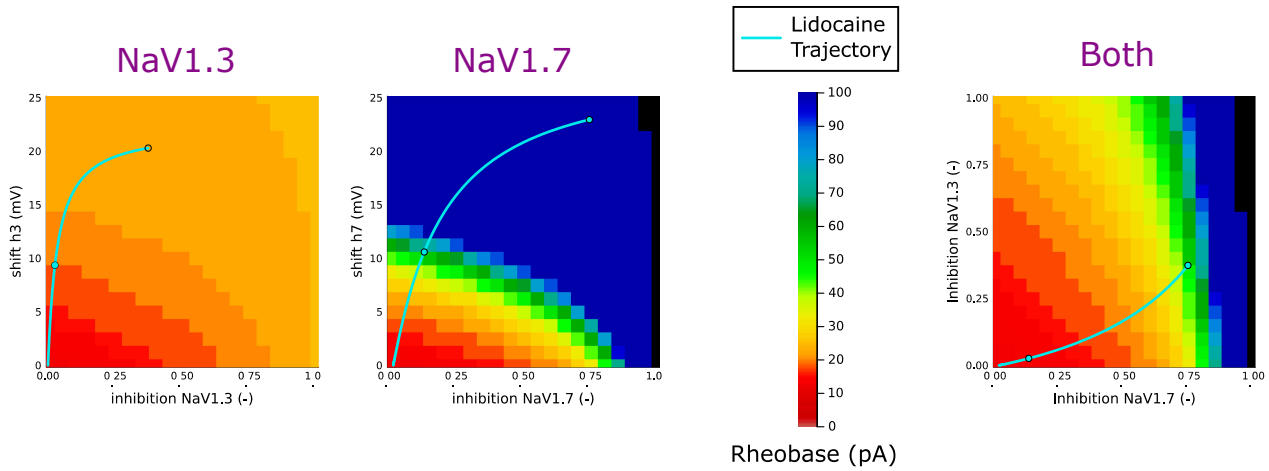

Figure 6.15: Heatmaps of the NaV1.3 and NaV1.7 modulation effects on the rheobase. The colorbar corresponds to different rheobase values, and the cyan curve corresponds to the lidocaine trajectory, where the first and second points correspond to concentrations of 100 and 1000 μM, respectively.

6.3 Indirect impact of the modulation on projection neuron

This section covers the consequences of DRG neuron modulation on the response of the projection neuron. Specifically, it investigates how the pattern and frequency of afferent input influence the output intensity of the projection neuron, beginning with continuous spiking and progressing to the effects of transient firing patterns.

The case of the rheobase is omitted because its consequences are straightforward: an afferent spike arriving at a resting projection neuron induces at least one action potential, and a higher rheobase in the DRG neuron directly causes the first projection neuron's response to appear for this higher input current value. Furthermore, unmodulated DIV4–7 neurons fire at most two successive spikes; because of this transient firing pattern, the subsequent sections focus exclusively on modulation in DIV0.

6.3.1 Afferent frequency in case of a spiking pattern

In the DRG neuron, shifting the steady-state activation of NaV1.8 increases the needed external current for the onset of sustained spiking without altering the firing frequency once initiated. In the projection neuron, this translates directly into a corresponding shift in the response generation, with no further effects.

Conversely, both inhibition and shifts of the inactivation increase the firing frequency of the DRG neuron. Because projection neuron firing rates are highly sensitive to NMDAR and Ca_{Ls} dynamics, higher afferent frequencies might be expected to facilitate NMDAR and m_{Ls} buildup at lower stimulus amplitudes relative to baseline. In practice, however, this does not occur. Because initiating sustained spiking requires a higher I_{ext} amplitude under NaV1.8 inhibition, the baseline firing rate still reaches hundreds of Hz at a lower stimulation amplitude. This can be seen by examining the frequency response as a function of stimulus amplitude applied to the DRG (Figure 6.16), which reveals that the unmodulated baseline condition reaches 100 Hz at a lower stimulus amplitude than the inhibited condition. Nevertheless, once spiking is initiated under inhibition, its elevated firing rate yields a stronger overall output. Consequently, non-extreme NaV1.8 inhibition produces a more dual response profile in the projection neuron, resulting in either a complete absence of activity or a high-frequency discharge.

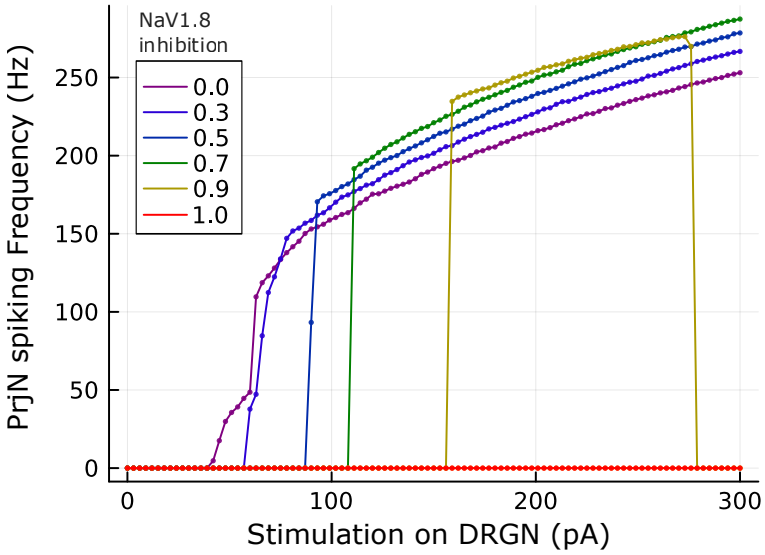

Figure 6.16: Projection neuron frequency response as a function of the stimulation applied to the DRG neuron under different levels of NaV1.8 inhibition. Firing frequencies are non-zero only when spiking occurs (transient responses are set to 0 Hz).

Combination heatmaps of the projection neuron response exhibit the same overall profiles as those for the DRG neuron, albeit at higher frequencies (Figure 6.17). However, the location of the peak frequency differs: while transient firing yields higher frequencies in the DRG neuron (Figure 6.9), peak frequency in the projection neuron is driven by sustained spiking. Specifically, sustained spiking induces responses in the 200 Hz range, whereas transient firing reaches only around 100 Hz. The mechanisms underlying these divergent response patterns are addressed below.

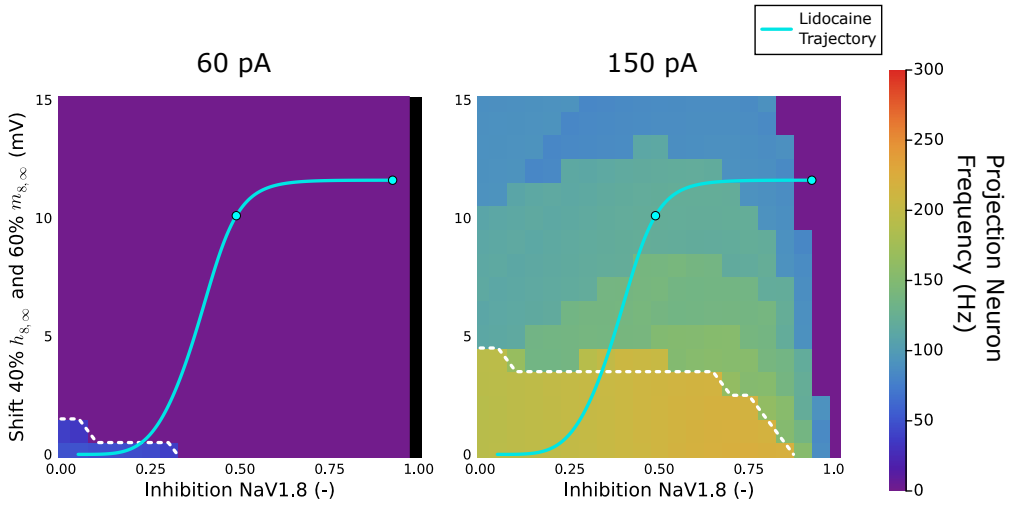

Figure 6.17: Heatmaps of the NaV1.8 modulation effect on frequency under different stimulation amplitudes acting on the DRG. The colorbar corresponds to different frequency values of the projection neuron and is common across all heatmaps; the cyan curve corresponds to the lidocaine trajectory, where the first and second points correspond to concentrations of 100 and 1000 μM, respectively. The white line forms the boundary between the region where continuous spiking occurs for the DRG neuron (bottom left of the heatmaps) and the region where it does not; the non-zero frequency values in this other region originate from transient regimes. The purple corresponds to a frequency of 0 Hz (a single spike), and black to no spike at all.

6.3.2 Responses to afferent transient versus sustained spiking patterns

The DRG exhibits high transient frequencies that represent the maximum values in the DRG heatmap, whereas the maximum frequencies in the projection neuron heatmap correspond to sustained spiking patterns. This key difference results from NMDAR and Ca_{Ls} dynamics. These mechanisms enable a progressive increase in output frequency over successive spikes. Consequently, although an afferent transient pattern may exhibit a higher initial frequency, its short duration limits accumulation.

Figure 6.18 illustrates how shifts in NaV1.8 activation reduce the projection neuron response by converting sustained spiking patterns into transient ones, reflecting how the firing pattern of the PrjN neuron mirrors that of the DRG neuron. Notably, sustained spiking induces stronger overall responses even at lower frequencies, highlighting that the firing pattern itself plays a critical role in shaping output intensity.

When considering transient patterns alone, the response is significantly reduced compared to sustained spiking. Nonetheless, the projection neuron still responds to a few afferent spikes with a high-frequency burst. The duration and intensity of this burst depend primarily on the number of afferent spikes, increasing further with higher firing frequencies. In Figure 6.18, the distinct lines within the transient cluster represent different counts of incoming spikes, starting at two. A larger spike count enables greater m_{Ls} and NMDAR-mediated accumulation, which then decays as the burst dissipates.

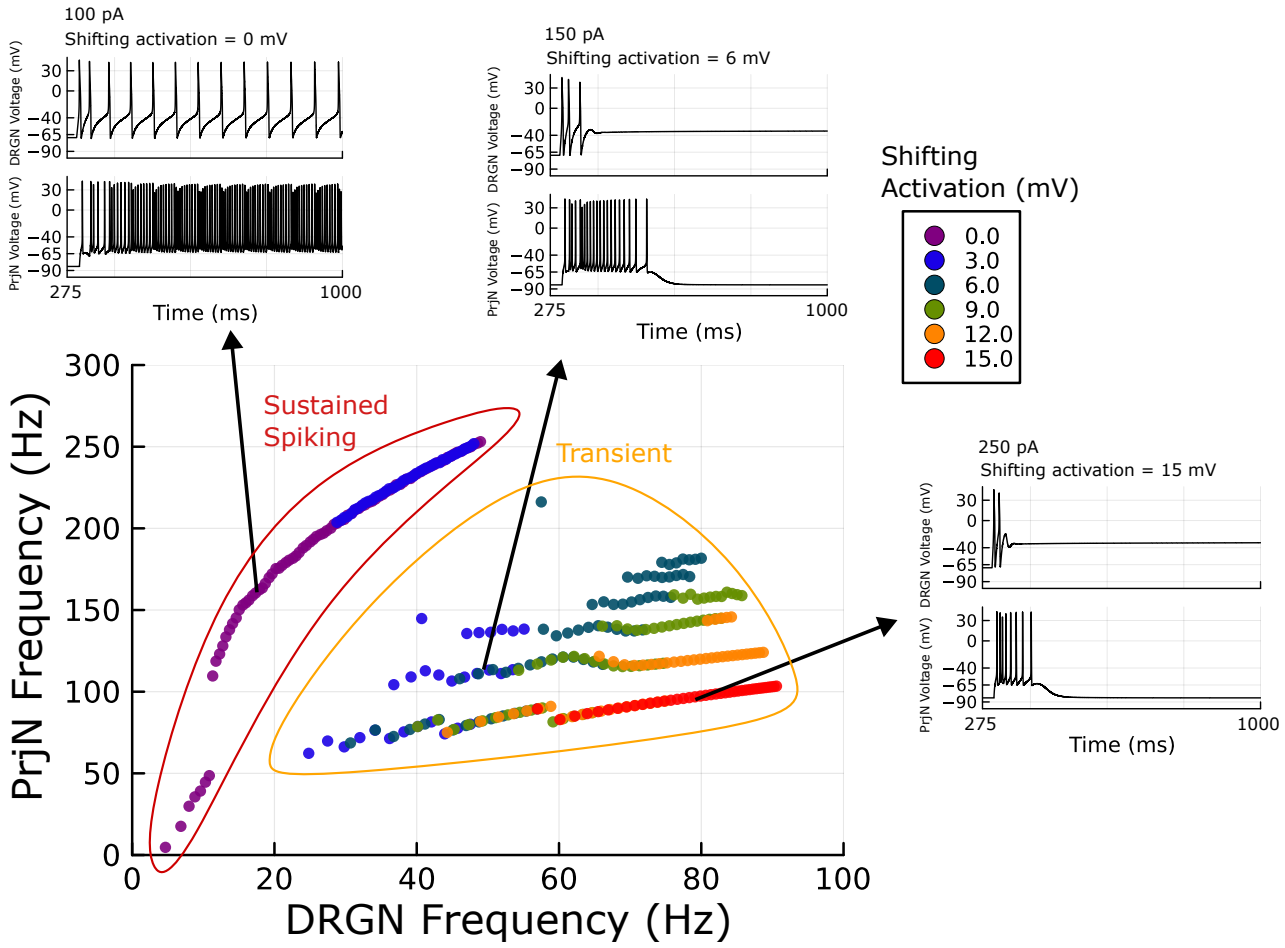

Figure 6.18: Projection neuron frequency response as a function of DRG neuron frequency across different activation gate shifts of NaV1.8. All data points correspond to distinct shifting values and fall into two isolated clusters: one representing sustained afferent spiking and the other representing transient firing. Three representative simulation cases are highlighted: one corresponding to sustained afferent spiking and two transient cases elicited by different input current amplitudes.

Chapter 7

Effect of NMDA receptor inhibition

This chapter explores how inhibiting the NMDAR maximal conductance affects the exhibited response of the projection neuron. It begins by studying the effect of this modulation alone, and then examines how it combines with afferent modulation of NaV1.8 in the context of DIV0.

7.1 NMDAR inhibition alone

NMDAR dynamics induce an increase in synaptic current due to the accumulation of available NMDA receptors. If this synaptic current is sufficiently large, it enhances the response of the projection neuron, potentially triggering Ca_{Ls} opening that further amplifies the neuronal response.

Inhibiting the NMDAR conductance makes it harder to trigger Ca_{Ls} activation, so that reaching more than 100 Hz requires a higher DRG neuron frequency. Besides, when Ca_{Ls} activation is established, inhibition also alters the exhibited frequencies; however, this alteration acts differently before and after Ca_{Ls} activation builds up.

Without Ca_{Ls}, NMDAR inhibition has a two-fold impact. If the NMDAR current is big enough, one afferent spike will lead to a two-spike response (as previously shown in Figure 5.10); if not, it will be a one-to-one response (Figure 7.1 with 70% inhibition). This means that inhibiting NMDA receptor conductance requires a larger build-up of NMDAR current before a significant postsynaptic effect is recovered. In other words, a higher afferent firing frequency is necessary to compensate for conductance loss and achieve an equivalent response. This can be seen on the different response curves (Figure 7.1): below a PrjN frequency of 50 Hz, all curves either follow the same line, which matches the afferent frequency, or detach from this trajectory to form a two-spike response. This behavior continues until the frequency is sufficiently high to rapidly trigger Ca_{Ls} channel activation. This threshold frequency corresponds roughly to 50 Hz.

With Ca_{Ls}, the frequency response is impacted in a continuous way: a higher level of inhibition will induce a lower frequency. In Figure 7.1, the PrjN frequencies differ between inhibition levels for a DRG neuron frequency of 40 Hz. Furthermore, it can be seen that reaching a significant Ca_{Ls} activation is possible even with 100 % NMDAR inhibition.

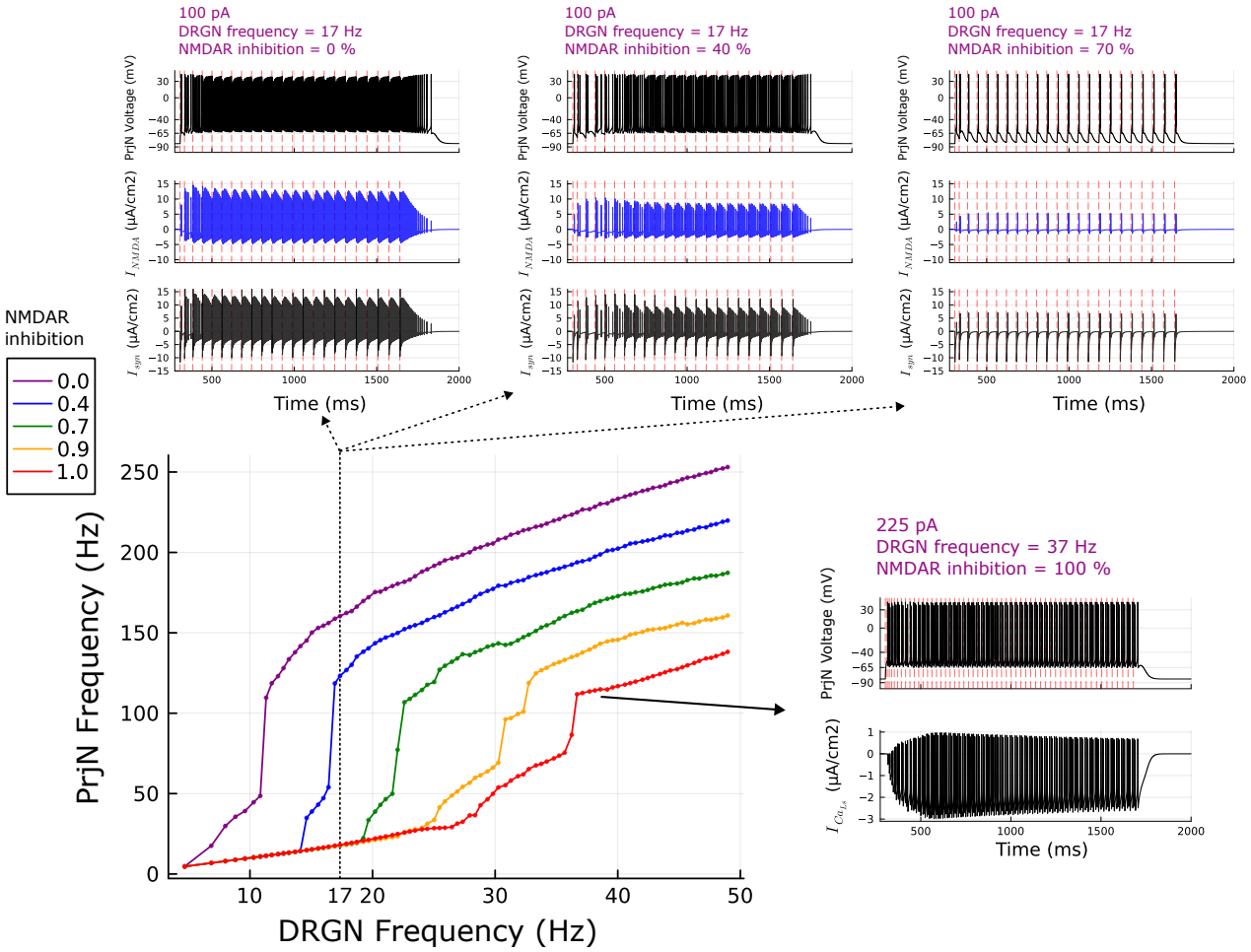

Figure 7.1: Frequency response curves of the projection neuron with different levels of NMDAR inhibition. Highlighted simulations on the top correspond to a DRG neuron stimulation of 100 pA under different levels of NMDAR inhibition: the top trace is the PrjN voltage, the middle trace is the NMDAR current, and the bottom trace is the total synaptic current. On the bottom right, Ca_{Ls} current without any NMDAR current is shown. In all simulations, the vertical red dashed lines correspond to the timings of afferent spikes.

Another way to visualize the effect of NMDAR inhibition is by making an analogy between I_{syn} and I_{ext} on the projection neuron. Looking at Figure 5.7, NMDAR inhibition can be viewed as a reduction in stimulation, which corresponds to moving leftward on the FI curve and thereby reducing the projection neuron firing frequency.

7.2 Combination with NaV1.8 modulation

7.2.1 Functional combination with NaV1.8 inhibition during afferent spiking

Individually, both NaV1.8 and NMDAR inhibition increase the minimum external current required to induce a response above 100 Hz. NaV1.8 accomplishes this by hindering the appearance of afferent spiking, and NMDAR by increasing the required afferent frequency (and thus stimulation) to induce a significant NMDAR build-up.

Together, the elevated stimulation requirement driven by NaV1.8 persists and is unaffected by NMDAR, since this elevation primarily involves the DRG neuron. However, the side effect of NaV1.8 inhibition that induces an increase in spiking frequency acts in opposition to the purpose of NMDAR inhibition. Considering a stimulation high enough to exhibit sustained DRG neuron spiking, the same stimulation will lead to a higher frequency and will therefore require a higher level of NMDAR inhibition to achieve an equivalent reduction of the NMDAR current.

Regarding Figure 7.2, at 100 pA, with no NaV1.8 inhibition, reaching a frequency around 50 Hz (in blue) is achieved with an NMDAR inhibition of 0.5. In comparison, with a 0.5 NaV1.8 inhibition, the same result is achieved with an NMDAR inhibition of 0.7. Yet, lower concentrations of lidocaine mainly act on NaV1.8, and then on NMDAR at higher concentrations. Consequently, lidocaine trajectory bypasses the state space where both modulations interact to demand supplementary NMDAR inhibition; thus, the observed response reduction stems primarily from the suppression of afferent spiking.

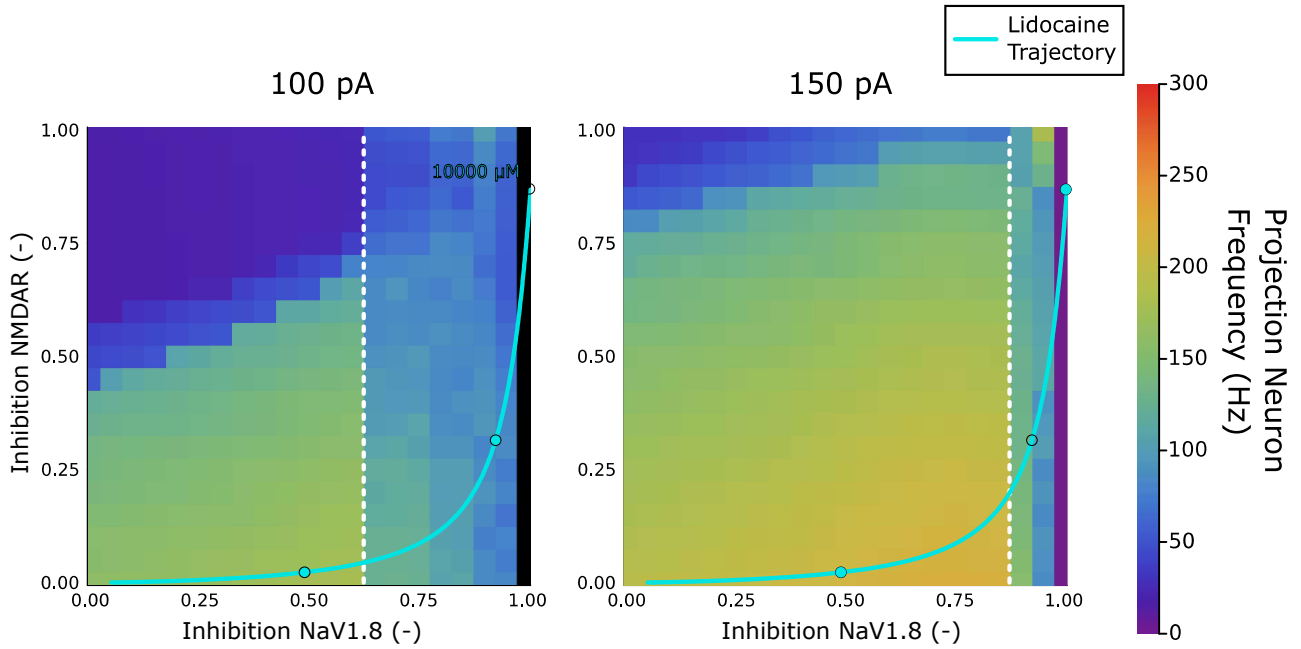

Figure 7.2: Heatmaps of the NaV1.8 and NMDAR modulation effect on frequency under different stimulation amplitudes acting on the DRG. The colorbar corresponds to different frequency values of the projection neuron and is common across all heatmaps; the cyan curve corresponds to the lidocaine trajectory, where the first, second and third points correspond to concentrations of 100, 1000, and 10000 μM, respectively. The white line forms the boundary between the region where continuous spiking occurs for the DRG neuron (bottom left of the heatmaps) and the region where it does not; the non-zero frequency values in this other region originate from transient regimes. The purple corresponds to a frequency of 0 Hz (a single spike), and black to no spike at all.

7.2.2 NMDAR inhibition reduces response bursts

In subsection 6.3.2, it was shown that even an afferent transient pattern can lead to more pronounced bursts. The intensity of these bursts depends mainly on the number of spikes, inducing larger NMDAR and Ca_{Ls} conductance. More than the burst itself, these accumulations lead to significant afterdischarges[1].

NMDAR inhibition allows for a reduction in burst frequency as well as the length of the afterdischarge; indeed, it is a key channel for this behavior, where complete inhibition leads to its total loss. Figure 7.3 illustrates the impact of inhibition on the number of spikes, reflecting the length of the afterdischarge and, more generally, the overall intensity of the response. Combining an afferent modulation that produces transient behaviors (such as the $m_{8,\infty}$ shift) with NMDAR inhibition allows for further mitigation: where two afferent spikes would previously lead to a burst of 9 spikes, NMDAR total inhibition reduces it to just 2 spikes.

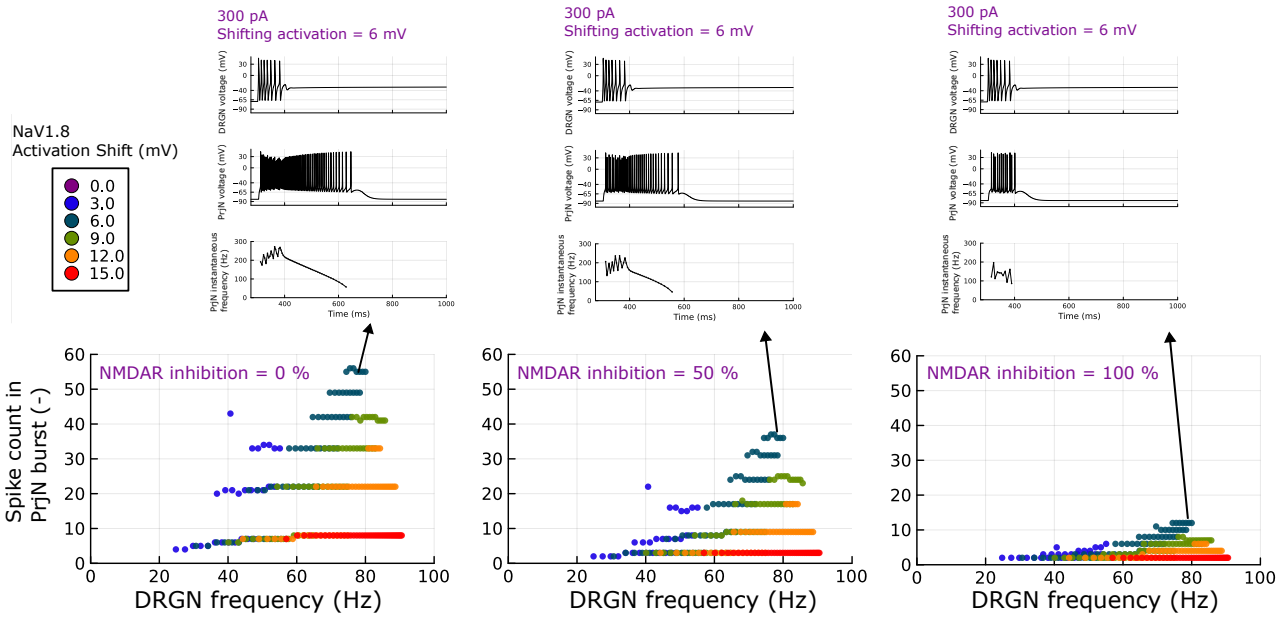

Figure 7.3: Total spike count in response to varying afferent frequencies across different shifts of the $m_{8,\infty}$ activation gate, shown without NMDAR conductance inhibition, with 50% inhibition, and with 100% inhibition. All points correspond to an afferent transient pattern. The same point is shown across the 3 levels of inhibition, where the top panel is the voltage of the DRG neuron, the middle panel is the voltage of the projection neuron, and the bottom panel is the instantaneous frequency of the projection neuron.

[1]Spikes that continue to fire even after the stimulation stops. In this case, this corresponds to the period when there are no further afferent spikes, yet the projection neuron is still firing.

Part IV

Synthesis and Outlook

Chapter 8

Discussion, Limitations, and Perspectives

8.1 Discussion

8.1.1 Excitability differences between DIV0 and DIV4–7

Xie et al. [27] report that DIV0 and DIV4–7 neurons exhibit equivalent excitability, defining equivalence by the shared capacity of both parameter sets to generate spiking or transient response patterns. While this observation holds, the two conditions yield distinct physiological properties that align with their respective biological contexts, namely, the non-inflamed state (DIV0) and the inflamed state (DIV4–7).

Regarding Figure 5.5, DIV0 represents a normal DRG neuron under physiological conditions, exhibiting robust spiking in response to high-amplitude stimulation alongside a higher rheobase, making it well-suited to drive nociceptive pain. In contrast, DIV4-7 models a hyperexcitable state associated with inflammatory pain, characterized by a lower rheobase and, upon NaV1.7 upregulation, sustained spiking at significantly reduced input currents (.

Another key distinction lies in the action potential morphology: a predominant TTX-R sodium current generates a sharp, prominent upstroke, whereas a predominant TTX-S current produces a broader, bump-like trajectory. In the former, depolarization occurs in two distinct phases, initiated primarily by the external stimulus and subsequently driven by the high-threshold NaV1.8 current. In the latter, depolarization is driven continuously by a combined contribution of sodium and external currents from onset to peak. Beyond spike shape, this mechanistic difference dictates the stimulus dependence of depolarization: while DIV0 neurons require sustained stimulation to reach their higher firing threshold, the lower threshold in DIV4–7 neurons allows brief stimuli to trigger spiking. In other words, DIV4–7 neurons are significantly more sensitive to stimulation.

Although noise is not explicitly included in the current models, it can be hypothesized to act as an unpredictable, low-amplitude stimulation. Under this assumption, the heightened sensitivity of DIV4–7 neurons emerges as a primary driver of spontaneous spiking. From a rheobase perspective, a low rheobase comparable in magnitude to these hypothetical low-amplitude inputs would allow such stimuli to induce a spike. In this context, "noise" encompasses two distinct sources of low-amplitude stimulation: microscopic, continuous fluctuations comparable to white noise arising from permanent molecular interactions, which align less directly with this hypothesis, and unpredictable macroscopic inputs, such as a t-shirt brushing against the skin, which present as sporadic, small stimulation. Still, this analogy between noise and low-amplitude stimulation was not tested here and remains a valuable point for future investigation.

This sensitivity depends not only on the predominant NaV subtype, but also on its maximal conductance. Depending on the NaV1.7 conductance value, the induced depolarization can manifest either as a sharp upstroke or as a large subthreshold oscillation (Figure 5.2). Given that action potentials are defined by an all-or-none criterion, baseline DIV4–7 neurons might not strictly qualify as generating full-amplitude spikes. Nevertheless, the underlying mechanisms of spike modulation remain valid.

8.1.2 Contribution of the different NaV modulations

The therapeutic purpose of these modulations

The purpose of these modulations is to reduce unwanted peripheral hyperexcitability that could induce non-protective pain, such as in neuropathic pain. In the context of this work, this is equivalent to either increasing the rheobase or increasing the stimulation amplitude for the onset of sustained spiking.

Considering DIV0 as the healthy state brings up the question regarding the relevance of modulating NaV1.8, since normal nociceptive behaviors are desirable and necessary. A first reason comes from degeneracy, which still makes it valuable to investigate all VGSCs that could be involved. A second reason is that specifically knowing how a drug interacts with the healthy state is as important as, or even more important than, its effect on a pathological state to avoid unwanted side effects. Finally, even if the nociceptor itself is healthy, modulating afferent excitability during phenomena such as central sensitization could help reduce spinal hyperexcitability, which will be discussed further below.

The increase in rheobase is capped by the loss of spike generation

Inhibition of the major VGSC increases the rheobase until spike generation fails entirely. In DIV0, the rheobase increase is fairly limited, with most variation restricted to a narrow range; significant changes occur only between 90% and 100% inhibition. In contrast, DIV4-7 shows a more gradual increase across a broader window, spanning from 40% to 80% inhibition.

In DIV0, targeting maximal conductance is not the most suitable strategy. The main purpose of the external input is to reach the NaV1.8 activation threshold, after which NaV1.8 current is either sufficient to drive a spike or not. Inhibiting NaV1.8 does not alter its voltage threshold. Consequently, the input current needs to be large enough to reach this same activation threshold, explaining why its magnitude does not need to increase significantly. In contrast, shifting NaV1.8 steady-state activation shifts this threshold to more depolarized voltages, requiring a higher input current to reach it and leading to a more effective, gradual increase in the rheobase.

In DIV4-7, shifting steady-state inactivation produces an effect similar to direct channel inhibition. While inhibition directly reduces the maximum conductance, a hyperpolarizing shift in inactivation reduces the dynamic conductance by increasing baseline channel inactivation at resting potential. However, this equivalence depends on these channels being low-threshold; in contrast, the NaV1.8 inactivation curve lies far from the resting potential and barely affects h_8 at rest.

On the other hand, examining the lidocaine trajectory effect reveals that although lidocaine quantitatively exerts a stronger overall modulation on DIV0 neurons than on DIV4–7 neurons, these modulations produce a greater increase in the rheobase of DIV4–7 neurons than in DIV0 neurons. In other words, a given concentration of lidocaine produces a smaller rheobase shift in the healthy DIV0 state compared to the pathological DIV4–7 state, showing its suitability to mitigate unwanted hyperexcitability while preserving healthy excitability.

All NaV1.8 modulations hinder the onset of sustained spiking

The three modulations independently hinder the sustained firing onset. The steady-state activation shift produces the greatest impact, followed by direct inhibition, and finally the steady-state inactivation shift. Furthermore, both direct inhibition and the activation shift can cause a complete loss of spiking. In contrast, direct inhibition and the inactivation shift reduce spike amplitude, which yields a higher firing frequency for the same stimulus amplitude.

Targeting multiple VGSCs

In the two-parameter set, the sodium current was predominantly carried by a single NaV subtype (NaV1.8 in DIV0 and NaV1.7 in DIV4-7). This reflects the core design objective of the original DRG neuron model [27]. This functional polarization means that modulating this predominant subtype leads to the most impactful changes. In the presented results, combined modulations of VGSCs were explored exclusively in Figure 6.15, confirming that most of the overall effect remains driven by the dominant channel subtype (NaV1.7 in this instance). However, inhibiting NaV1.3 still produced a significant impact on the rheobase, particularly when NaV1.7 was concurrently inhibited.

The lidocaine trajectory

The various lidocaine trajectories rely on empirical data that were not strictly derived, as the shift curves were constructed using only two data points, with some points chosen arbitrarily. Nonetheless, these curves are intended to illustrate how drug-induced modulations alter neuronal excitability, using lidocaine as a representative example. Conversely, if the relative conductances in a cell are known or estimated, model-generated heatmaps could help identify which drug (or combination of drugs) is best suited to target a specific excitability profile. In this framework, the distinct modulation trajectories of individual drugs could be combined into a single targeting vector aimed directly at the desired outcome.

8.1.3 The impact of the afferent firing pattern on the postsynaptic response

NMDAR and Ca_{Ls} dynamics heighten the sensitivity of projection neurons to small shifts in afferent frequency

The synaptic component was designed so that each presynaptic spike triggers at least one postsynaptic spike, driven primarily by AMPAR current. This ensures that projection neurons register all afferent input, while NMDAR currents enable frequency-dependent modulation of synaptic strength, and Ca_{Ls} provides further frequency-dependent adaptation in the projection neuron. This adaptation is clearly evident in the sharp transition from firing frequencies around 50 Hz to over 100 Hz, triggered by a subtle increase in afferent input from 11 Hz to 12 Hz (corresponding to a 10 pA stimulation increment at DIV0). At firing rates below 50 Hz, responses exhibit either a single spike transmission mediated by AMPAR or a two-spike output supported by NMDAR accumulation. In contrast, higher firing rates rely on additional m_{Ls} build-up.

Biologically, this illustrates the wind-up phenomenon, showing how afferent frequency and NMDAR/Ca_{Ls} dynamics interact to produce a response that gradually ramps up to output frequencies four times higher than the input. NMDAR accumulation is the faster mechanism, where a single spike drives a significant increase in synaptic strength, whereas m_{Ls} requires more time to build up. However, the decay times for both mechanisms are on the order of hundreds of milliseconds, with the resulting afterdischarge durations operating in a similar time range. Consequently, the wind-up modeled here is short-term compared to that reported by Aguiar et al. [22], which incorporates long-term currents. Nevertheless, because the afferent firing frequency in this model is tenfold higher, these long-term currents are not necessary to elicit the wind-up effect.

The impact on the projection response to pass from afferent spiking to transient

For both NMDAR and m_{Ls} accumulation, the instantaneous firing frequencies in the DRG and projection neurons play a critical role. The firing rate must remain sufficiently high to prevent the complete decay of NMDAR or m_{Ls} between action potentials. Furthermore, because each spike contributes only a limited amount, these elevated frequencies must persist over a sufficiently long duration to drive cumulative activation.

Consequently, a short transient afferent pattern yields far less NMDAR accumulation than sustained spiking. This, in turn, indirectly reduces m_{Ls} accumulation by lowering the overall response frequency. This illustrates how peripheral sensitization, by facilitating sustained spiking, plays a central role in indirectly modulating projection neuron excitability and driving central sensitization. In other words, mitigating afferent spiking by shifting firing from sustained to transient patterns can, in turn, help attenuate projection neuron responses. Still, transient patterns do induce both NMDAR and Ca_{Ls} current accumulation and trigger bursts, with the duration of these bursts depending directly on the extent of that accumulation.

8.1.4 Contribution of NMDAR inhibition

Pharmacological inhibition of NMDA receptors prevents and attenuates central sensitization.

Inhibiting the NMDAR current increases the minimum DRG neuron firing frequency required to trigger NMDAR accumulation and, indirectly, m_{Ls} accumulation, with the effects of this inhibition differing depending on the presence of $I_{Ca_{Ls}}$ (Figure 7.1). Consequently, NMDAR inhibition provides an effective strategy to substantially reduce central sensitization without completely silencing projection neuron responses.

Results show that reducing NMDAR current decreases firing frequency even in the presence of Ca_{Ls} current. This indicates that NMDAR is not merely an initiator of central sensitization, but also actively participates in its maintenance once established. Consequently, inhibiting this channel remains effective even after central sensitization has developed.

Regarding the transient afferent pattern, this modulation significantly reduces both the frequency and duration of the generated burst, with the NMDAR current serving as a necessary component to sustain long afterdischarges (Figure 7.3). This highlights the utility of NMDAR inhibition when combined synergistically with DRG modulations that leave a residual transient pattern.

The side effects of NaV1.8 modulations can induce the need for NMDAR extra inhibition

Individually, both NMDAR inhibition and NaV1.8 inhibition increase the required external current for the onset of high projection neuron responses. However, combining them does not produce a greater effect and actually results in an extra compensation. The remaining elevation of external current corresponds to that induced by NaV1.8 inhibition alone, driven by the absence of DRG spiking. This compensation stems from the higher firing frequency induced by NaV1.8 inhibition, which requires additional NMDAR inhibition to achieve the same degree of suppression. This observation likewise extends to shifts in NaV1.8 steady-state inactivation that produce a similar side effect.

If the primary goal of the treatment is to shift the minimal stimulation required for central sensitization onset upward, dual administration may not be useful, since this will only come from NaV1.8 inhibition, or, if the shift induced by NMDAR is larger, the side effect frequency will decrease its benefit. From another perspective, however, NMDAR inhibition can act as a mitigator for the frequency-increase side effect observed at high stimulation, thereby allowing this combination to simultaneously reduce both peripheral and central excitability.

8.2 Limitations

8.2.1 The omitted modulations

This work focused on NaV channel and NMDA receptor inhibition, as well as shifts in steady-state activation and inactivation kinetics. However, these are not the only gating properties that can be affected. For instance, voltage-dependent time constants ($\tau(V)$) could also undergo shifts, which would drastically alter the gating kinetics and dynamic response of the affected variables.

Another omitted target is potassium channels, which could also undergo inhibition. Regarding lidocaine, neglecting potassium channels at concentrations around 1000 μM remains reasonable, as lidocaine preferentially targets VGSCs. However, at higher concentration ranges such as 10000 μM (where NMDA receptor modulation occurs) potassium currents are almost certainly impacted as well.

8.2.2 The complexity of quantifying drug effects

Quantifying the distinct modulations induced by a drug can be challenging. For instance, in our model, a shift in NaV1.7 steady-state inactivation produces behavioral changes similar to direct channel inhibition. Researchers seeking to evaluate both mechanisms separately risk double-counting the shift effect, as its influence is already implicitly accounted for in the net inhibition.

Furthermore, the net trajectory resulting from multiple drugs cannot be calculated by simply summing individual drug effects. In reality, key drug–drug interactions complicate the overall outcome, and the number of parameters modulated in vivo can be vastly higher than the two or three modulation dimensions examined here.

8.2.3 A qualitative study

The stimulation amplitudes and durations were selected specifically to showcase key behaviors of the neuron model rather than to mimic physiological stimulation protocols. Consequently, the modeled neuron's quantitative response characteristics do not necessarily match those that would be observed in reality.

8.3 Perspective

8.3.1 Exploring other combinations of VGSCs

Although in vivo inflammatory changes produce a transition similar to the one from DIV0 to DIV4-7, a clear distinction remains between a generic TTX-S-dominant current and a NaV1.7-dominant current. This limitation stems partly from the small number of ion channels modeled here. For example, in DIV0, NaV1.8 is the only TTX-R channel present, forcing all TTX-R currents to depend entirely on it.

Using the same DRG neuron model, alternative ion channel combinations could be evaluated to explore how baseline channel expression shapes modulation outcomes. For instance, creating a DIV4-7 equivalent with elevated NaV1.3 expression or increased NaV1.7 conductance would allow examination of effects of modulations on sustained spiking. Another promising direction would be incorporating additional NaV isoforms, such as NaV1.9.

8.3.2 Adding other modulations

Unexamined modulation parameters, such as voltage-dependent time constants, could also be incorporated into future models. Additional phenomenological modulations could also be introduced, such as relieving the Mg^{2+} block and enhancing calcium dynamics, to simulate projection neurons under sustained central sensitization. Finally, incorporating noise would allow for a direct investigation into its consequences on spontaneous spiking.

8.3.3 Constructing several multi-drug trajectories and evaluating their potential combinations

Further experiments could be performed to collect more rigorous data on lidocaine, as well as on other candidate drugs and their combinations. These empirical findings could then be synthesized to evaluate how specific drug combinations could be tailored to achieve precise targets in channel modulation and excitability.

8.3.4 Bifurcation and bistability analyses

To enable a more quantitative and rigorous analysis of modulation effects, bifurcation diagrams and other dynamical systems tools could be employed. In fact, bifurcation analyses were performed, but they were excluded because they fell outside the scope of this work.

Chapter 9

Conclusions

This thesis investigates lidocaine-mediated modulations of DRG neurons and projection neurons to treat their hyperexcitability, specifically through targeting voltage-gated sodium channels and NMDA receptors. Where hyperexcitability is a state in which neurons fire excessively, characterized by a low rheobase and a sustained spiking response to an abnormally small stimulus.

To increase the rheobase, the results show that lidocaine-induced modulation is more effective on DIV4-7 than on DIV0. Inhibiting the maximum conductance of NaV1.7, NaV1.3, or both leads to a gradual increase in the rheobase, whereas inhibiting NaV1.8 has almost no effect until neuron excitability is completely shut down. Regarding the inactivation gates, shifting them toward lower potentials for NaV1.7 and NaV1.3 acts similarly to conductance inhibition by inducing stronger inactivation at the resting state; in comparison, NaV1.8 is barely affected. However, shifting NaV1.8 activation toward higher voltages gradually increases the rheobase by elevating its activation threshold. More generally, lower lidocaine concentrations are required to affect DIV4-7 than DIV0, which is promising for treating inflamed states without excessively interfering with healthy states.

The three modulations of NaV1.8 increase the minimal stimulation amplitude required to induce spiking, with conductance inhibition and activation shifting even leading to a complete loss of sustained spiking without necessarily abolishing the neuron's ability to produce single spikes. However, both conductance inhibition and inactivation shifting reduce spike amplitude, which increases firing frequency when spiking occurs. These three modulations also induce transient firing patterns. Nevertheless, the model shows that sustained afferent spiking triggers a significantly higher projection neuron response than transient patterns due to the occurrence of wind-up. This illustrates the impact of peripheral sensitization on central sensitization and shows that treating the DRG neuron can help mitigate projection neuron hyperexcitability.

More specifically, inhibiting the maximal conductance of NMDAR, one of the primary mediators of wind-up, hinders the occurrence of wind-up. When NMDA receptors are inhibited, projection neurons exhibit lower firing frequency, requiring higher afferent frequencies to drive significant NMDAR accumulation. Additionally, this inhibition helps mitigate the burst response induced by transient afferent patterns. However, the results show that when afferent spiking still occurs, NaV1.8 conductance inhibition and inactivation shifting necessitate additional NMDAR inhibition. The side effect of increased firing frequency can lead to higher frequencies for the same stimulation, meaning that further NMDAR inhibition is necessary to achieve results comparable to those without this afferent modulation.

The present work aimed to capture the lidocaine trajectory within the modulation space of NaV and NMDAR. However, few studies to date provide data on channel modulation under lidocaine action. Additional data on these channel modulations and other possible types of modulations would be required to comprehensively capture lidocaine's effects on the dorsal horn network.

Part V

Appendix

Chapter 10

Appendix

10.1 Dorsal root ganglion neuron model

Gate functions

NaV1.3

$$\alpha_{m_3} = \frac{10.22}{1+\exp\frac{V-(-19.19-4.2)}{-15.43}} \qquad \alpha_{h_3} = \frac{0.0744}{1+\exp\frac{V-(-89.76-4.2)}{11.07}}$$
$$\beta_{m_3} = \frac{23.76}{1+\exp\frac{V-(-82.37-4.2)}{14.53}} \qquad \beta_{h_3} = \frac{2.54}{1+\exp\frac{V-(2.2-4.2)}{-10.68}}$$

NaV1.7

$$\alpha_{m_7} = \frac{10.22}{1+\exp\frac{V-(-7.19-4.2)}{-15.43}} \qquad \alpha_{h_7} = \frac{0.0744}{1+\exp\frac{V-(-99.76-4.2)}{11.07}}$$
$$\beta_{m_7} = \frac{23.76}{1+\exp\frac{V-(-70.37-4.2)}{14.53}} \qquad \beta_{h_7} = \frac{2.54}{1+\exp\frac{V-(-7.8-4.2)}{-10.68}}$$

NaV1.8

$$\alpha_{m_8} = \frac{7.21}{1+\exp\frac{V-(0.063-5.3)}{-7.86}} \qquad \alpha_{h_8} = \frac{1.63}{1+\exp\frac{V-(-68.3-5.3)}{10.01}}$$
$$\beta_{m_8} = \frac{7.4}{1+\exp\frac{V-(-53.06-5.3)}{19.34}} \qquad \beta_{h_8} = \frac{0.81}{1+\exp\frac{V-(11.44-5.3)}{-13.12}}$$

K_{dr}

$$n_{dr,\infty} = \frac{1}{1+\exp\frac{V+32}{-5.14}} \qquad l_{dr,\infty} = \frac{1}{1+\exp\frac{V+61}{12.85}}$$
$$\tau_{n_{dr}} = \frac{57.735\exp\frac{V+32}{-12.85}}{1+\exp\frac{V+32}{-5.14}} \qquad \tau_{l_{dr}} = \frac{1732.05\exp\frac{V+61}{12.85}}{1+\exp\frac{V+61}{12.85}}$$

K_M

$$n_{M,\infty} = \frac{1}{1 + \exp\frac{V-(-35)}{5}}$$
$$\tau_{n_M} = \frac{1000}{3.3\exp\frac{V-(-35)}{10}} + \frac{\exp\frac{-(V+35)}{10}}{3^{0.15}}$$

K_{AHP}

$$z_{AHP,\infty} = \frac{1}{1 + \exp\frac{5-V}{4}}$$
$$\tau_{z_{AHP}} = 100$$

Ionic Currents

$$I_{NaV1.3} = g_{NaV1.3}\ {m_3}^3\ h_3\ (V - E_{Na})$$
$$I_{NaV1.7} = g_{NaV1.7}\ {m_7}^3\ h_7\ (V - E_{Na})$$
$$I_{NaV1.8} = g_{NaV1.8}\ {m_8}^3\ h_8\ (V - E_{Na})$$
$$I_{K_{dr}} = g_{K_{dr}}\ {n_{dr}}^3\ l_{dr}\ (V - E_K)$$
$$I_{K_M} = g_{K_M}\ n_M\ (V - E_K)$$
$$I_{K_{AHP}} = g_{K_{AHP}}\ z_{AHP}\ (V - E_K)$$
$$I_{Leak} = g_{Leak}\ (V - E_{Leak})$$

Differential System

$$\frac{dV_m}{dt} = \frac{I_{ext} - I_{NaV1.3} - I_{NaV1.7} - I_{NaV1.8} - I_{K_{dr}} - I_{K_M} - I_{K_{AHP}} - I_{Leak}}{C_m}$$
$$\frac{dp_i}{dt} = \frac{p_{i,\infty} - p_i}{\tau_i}$$

Parameters

	DIV0	DIV4-7	Unity
$g_{NaV1.3}$	0.0	0.35	mS/cm^2
$g_{NaV1.7}$	3.0	35.0	
$g_{NaV1.8}$	30.0	0.2	
g_{Leak}	0.025	0.035	
$g_{K_{dr}}$	3.5		
g_{K_M}	0.05	0.5	
$g_{K_{AHP}}$	2.5		
E_{Na}	50.0		mV
E_K	-90.0		
E_{Leak}	-62.5	-70.0	
r	11.63	18.13	μm
C_r	17.0	41.3	pF
I_{hold}	-3	0	pA

Table 10.1: Dorsal root ganglion neuron parameters

$$CellArea = 4\pi r^2 \qquad [\mu m^2]$$

$$C_m = 100 \times \frac{C_r}{CellArea} \qquad [\mu F/cm^2]$$

$$I_0 = \frac{I_{hold} \times 10^{-6}}{CellArea \times 10^{-8}} \qquad [\mu A/cm^2]$$

$$Excitation = \frac{Amp \times 10^{-6}}{CellArea \times 10^{-8}} \qquad [\mu A/cm^2]$$

$$I_{ext}(t) = \begin{cases} I_0 & \text{if not during stimulation} \\ I_0 + Excitation & \text{if during stimulation} \end{cases}$$

10.2 Projection neuron model

Gate functions

Na

$$m_{Na,\infty} = \frac{0.32 \times \frac{76-V}{exp(\frac{76-V}{4})-1}}{0.32 \times \frac{76-V}{exp(\frac{76-V}{4})-1} + 0.28 \times \frac{V-103}{exp(\frac{V-103}{5})-1}}$$

$$\tau_{m_{Na}} = \frac{1}{0.32 \times \frac{76-V}{exp(\frac{76-V}{4})-1} + 0.28 \times \frac{V-103}{exp(\frac{V-103}{5})-1}}$$

$$h_{Na,\infty} = \frac{0.128 \times \exp\left(\frac{80-V}{18}\right)}{0.128 \times \exp\left(\frac{80-V}{18}\right) + \frac{4}{1+\exp\left(\frac{103-V}{5}\right)}}$$
$$\tau_{h_{Na}} = \frac{1}{0.128 \times \exp\left(\frac{80-V}{18}\right) + \frac{4}{1+\exp\left(\frac{103-V}{5}\right)}}$$

K_{dr}

$$m_{dr,\infty} = \frac{0.032 \times \frac{78-V}{exp\left(\frac{78-V}{5}\right)-1}}{0.032 \times \frac{78-V}{exp\left(\frac{78-V}{5}\right)-1} + 0.5 \times \frac{73-V}{40}}$$
$$\tau_{m_{dr}} = \frac{1}{0.032 \times \frac{78-V}{exp\left(\frac{78-V}{5}\right)-1} + 0.5 \times \frac{73-V}{40}}$$

K_{ir}

$$m_{ir,\infty} = \frac{1}{1 + \exp\left(\frac{V+65}{10}\right)}$$
$$\tau_{m_{ir}} = 1$$

K_M

$$m_{M,\infty} = \frac{1}{1 + \exp\left(\frac{-V-76.1}{25.7}\right)}$$
$$\tau_{m_M} = 103$$

Ca_{Lf}

$$m_{Lf,\infty} = \frac{1}{1 + \exp -\frac{V+17.5}{4.3}} \qquad h_{Lf,\infty} = \frac{1}{1 + \exp\left(\frac{V+14}{4.03}\right)}$$
$$\tau_{m_{Lf}} = \frac{0.5}{\frac{0.1(-V-40)}{exp(0.1(-V-40))-1} + 4\exp\left(-\frac{-(V+65)}{18}\right)} \qquad \tau_{h_{Lf}} = 1500$$

Ca_{Ls}

$$m_{Ls,\infty} = \frac{1}{1 + \exp\left(-\frac{V+25.4}{6}\right)} \qquad h_{Ls,\infty} = \frac{1}{1 + \exp\left(\frac{V+14}{4.03}\right)}$$
$$\tau_{m_{Ls}} = \frac{160}{\frac{0.1(-V-40)}{exp(0.1(-V-40))-1} + 4\exp\left(-\frac{-(V+65)}{18}\right)} \qquad \tau_{h_{Ls}} = 10000$$

Ionic Currents

The "×1000" for the calcium current allows it to pass from (mA/cm^2) to $(\mu A/cm^2)$

$$
\begin{aligned}
I_{Na} &= g_{Na}\ {m_{Na}}^3\ h_{Na}\ (V - E_{Na}) \\
I_{K_{dr}} &= g_{K_{dr}}\ {m_{dr}}^4\ (V - E_K) \\
I_{K_{ir}} &= g_{K_{ir}}\ m_{ir}\ (V - E_K) \\
I_{K_M} &= g_{K_M}\ m_M\ (V - E_K) \\
I_{Ca_{Lf}} &= p_{Ca_{Lf}}\ {m_{Lf}}^2\ h_{Lf}\ \mathrm{GHK}(V, [Ca^{2+}]_i) \times 1000 \\
I_{Ca_{Ls}} &= p_{Ca_{Ls}}\ m_{Ls}\ h_{Ls}\ \mathrm{GHK}(V, [Ca^{2+}]_i) \times 1000 \\
I_{Leak} &= g_{Leak}\ (V - E_{Leak})
\end{aligned}
$$

with

$$
\begin{aligned}
z &= 10^{-3} \times V \times \frac{2F}{RT} \\
\mathrm{GHK}(V, [Ca^{2+}]_i) &= 10^{-3} \times 2F \times \left([Ca^{2+}]_i \times \frac{-z}{e^{-z} - 1} - [Ca^{2+}]_o \times \frac{z}{e^{z} - 1} \right)
\end{aligned}
$$

Differential System

I_{ext} is non-zero if the projection neuron is simulated in a stand-alone model, whereas I_{syn} is non-zero if the projection neuron is simulated together with the DRG neuron model. The value of I_{ext} is calculated equivalently as with the DRG neuron, and the value of I_{syn} (and $I_{Ca\,from\,syn}$) is provided in the synapse section. $\frac{I_{Ca}}{10^3}$ is made to pass from $(\mu A/cm^2)$ to (mA/cm^2).

$$
\begin{aligned}
\frac{dV_m}{dt} &= \frac{I_{ext} - I_{Na} - I_{K_{dr}} - I_{K_{ir}} - I_{K_M} - I_{Ca_{Lf}} - I_{Ca_{Ls}} - I_{Leak} - I_{syn}}{C_m} \\
\frac{dp_i}{dt} &= \frac{p_{i,\infty} - p_i}{\tau_i} \\
\frac{d[Ca^{2+}]_i}{dt} &= -10^7 \times \frac{I_{Ca}}{10^3} \times \frac{1}{2Fd} - \frac{\left([Ca^{2+}]_i - [Ca^{2+}]_{i,0}\right)}{\tau_{Ca}}
\end{aligned}
$$

with

$$
I_{Ca} = I_{Ca_{Lf}} + I_{Ca_{Ls}} + I_{Ca\,from\,syn}
$$

Parameters

	PN	Unity
g_{Na}	30.0	mS/cm^2
$g_{K_{dr}}$	4.0	
$g_{K_{ir}}$	0.15	
g_{K_M}	0.0	
g_{Leak}	0.03268	
p_{Lf}	0.0	$cm\ s^{-1}$
p_{Ls}	0.75×10^{-5}	
$[Ca^{2+}]_o$	2.0	mM
τ_{Ca}	10.0	ms
E_{Na}	50.0	mV
E_K	-90.0	
E_{Leak}	-60.1	
F	96520.0	C/mol
T	309.15	K
$CellArea$	1256.64	μm^2
C_m	1.0	$\mu F/cm^2$
d	1.0	nm
I_{hold}	0.0	pA

Table 10.2: Projection neuron parameters

10.3 Synapse

Ionic Currents

$$
\begin{aligned}
I_{AMDA} &= (B_{AMPA} - A_{AMPA})\, g_{AMPA}\, (V - E_{AMPA}) \\
I_{NMDA} &= (B_{AMPA} - A_{AMPA})\, g_{AMPA}\, (V - E_{AMPA})\, Mg_{Block}(V) \\
I_{syn} &= I_{AMDA} + I_{NMDA} \\
I_{Ca\,from\,syn} &= I_{NMDA} \times ratio
\end{aligned}
$$

with

$$
\begin{aligned}
Mg_o &= 1.0 \qquad\qquad [mM] \\
Mg_{Block}(V) &= \frac{1}{1 + \exp\left(-0.062\, V\right) \frac{Mg_o}{3.57}}
\end{aligned}
$$

Differential System

$$\begin{aligned}
\tau_{rise,i}\ \frac{dA_i}{dt} &= -A_i + S_i(t)\ [w_i\ fact_i\ (U_{SE,i}\ P_i)] \\
\tau_{decay,i}\ \frac{dB_i}{dt} &= -B_i + S_i(t)\ [w_i\ fact_i\ (U_{SE,i}\ P_i)] \\
\tau_{fac,i}\ \frac{dU_{SE,i}}{dt} &= -U_{SE,i} + S_i(t)\ [U_{1,i}\ (1 - U_{SE,i})] \\
\tau_{rec,i}\ \frac{dP_i}{dt} &= (1 - P_i) - S_i(t)\ [U_{SE,i}\ P_i]
\end{aligned}$$

with t_n corresponds to the n afferent spike time.

$$\begin{aligned}
tp_i &= \frac{\tau_{decay,i}\ \tau_{rise,i}}{\tau_{decay,i} - \tau_{rise,i}} \log\left(\frac{\tau_{decay,i}}{\tau_{rise,i}}\right) \\
fact_i &= \frac{1}{\exp\left(\frac{-tp_i}{\tau_{decay,i}}\right) - \exp\left(\frac{-tp_i}{\tau_{rise,i}}\right)} \\
S_i(t) &= \sum_n \delta([t + delay_i] - t_n)
\end{aligned}$$

Parameters

	AMPA	NMDA	Unity
g	1.0		mS/cm^2
E	0.0		mV
w	0.144	0.192	-
τ_{rise}	0.1	2.0	ms
τ_{decay}	5.0	100.0	
τ_{fac}	0.1		
τ_{rec}	0.1		
U_1	1.0		-
$delay$	0.5		ms
$ratio$	-	0.1	-

Table 10.3: Synapse parameters

Initial Condition

$V_0 \equiv V$ at the initial condition.

	DIV0	DIV4-7
V	-69.5	-70.0
m_3	0.0	0.0
h_3	0.0	0.7191
m_7	0.0	0.0219
h_7	0.0	0.2579
m_8	0.0	0.0
h_8	0.9952	0.9964
n_{dr}	0.0	0.0
l_{dr}	0.6487	0.6058
n_M	0.0014	0.0
z_{AHP}	0.0	0.0

PN	
V	-85.0
m_{Na}	$m_{Na,\infty}(V_0)$
h_{Na}	$h_{Na,\infty}(V_0)$
m_{dr}	$m_{dr,\infty}(V_0)$
m_{ir}	$m_{ir,\infty}(V_0)$
m_M	$m_{M,\infty}(V_0)$
m_{Ls}	$m_{Ls,\infty}(V_0)$
h_{Ls}	$h_{Ls,\infty}(V_0)$
m_{Lf}	$m_{Lf,\infty}(V_0)$
h_{Lf}	$h_{Lf,\infty}(V_0)$
$Ca_{i,0}$	5.0×10^{-5}

Synapse	
A_{NMDA}	0.0
B_{NMDA}	0.0
$U_{SE,NMDA}$	0.0
P_{NMDA}	1.0
A_{AMPA}	0.0
B_{AMPA}	0.0
$U_{SE,AMPA}$	0.0
P_{AMPA}	1.0

Table 10.4: Initial conditions

10.4 Lidocaine

Lidocaine inhibition

$$hill(C_{lido}) = y_0 + \frac{f_{max} \times C_{lido}^h}{IC_{50}^h + C_{lido}^h}$$

$$\text{Inhibition}_{NaV1.3}(C_{lido}) = \frac{0.997 \times C_{lido}^{0.48}}{284^{0.48} + C_{lido}^{0.48}} \quad [35]$$

$$\text{Inhibition}_{NaV1.7}(C_{lido}) = 0.0152 + \frac{1.0079 \times C_{lido}^{1.31}}{477.1^{1.31} + C_{lido}^{1.31}} \quad [35]$$

$$\text{Inhibition}_{NaV1.8}(C_{lido}) = 0.0478 + \frac{0.9698 \times C_{lido}^{1.06}}{118.31^{1.06} + C_{lido}^{1.06}} \quad [36]$$

$$\text{Inhibition}_{NMDA}(C_{lido}) = \frac{C_{lido}^{1.3}}{1821^{1.3} + C_{lido}^{1.3}} \quad [39]$$

Lidocaine steady state shift

Where $\log \equiv \log_{10}$

NaV1.3

$$\text{Shift}_{h_{3,\infty}}(C_{lido}) = -\left[\frac{-21.4}{1 + \exp\left(3.17 \times (\log C_{lido} - \log 120)\right)} + 21.4\right]$$

NaV1.7

$$\text{Shift}_{h_{7,\infty}}(C_{lido}) = -\left[\frac{-24.2}{1 + \exp\left(3.17 \times (\log C_{lido} - \log 120)\right)} + 24.2\right]$$

NaV1.8

$$\text{Shift}_{m_{8,\infty}}(C_{lido}) = \frac{-6.8}{1 + \exp\left(8.732 \times (\log C_{lido} - \log 56.5)\right)} + 6.8$$
$$\text{Shift}_{h_{8,\infty}}(C_{lido}) = -\left[\frac{4.8}{1 + \exp\left(-14.16 \times (\log C_{lido} - \log 77)\right)}\right]$$

10.5 Numerical tools

The computational experiments were implemented in Julia. The code is available on GitHub: `https://github.com/Thopag/TFE`

10.5.1 Solver

The computational experiments were performed using the SDEproblem and solve functions from the `DifferentialEquations` package. Default parameters were used for both, with the exception of the one directly related to the ODE system and `dtmax`, which was set to 0.01.

The SDEproblem was used instead of the ODEproblem because noise was initially integrated into the model to reproduce the results from [27]. This solver was then retained even though noise is set to zero for the simulations conducted in this thesis.

10.5.2 Spike detection

Spikes are detected using the solver's built-in event infrastructure. Specifically, a spike event is triggered whenever the voltage trace crosses 0 mV from below.

10.5.3 Instantaneous frequency and global frequency

The instantaneous frequency is calculated between consecutive spikes; specifically, it is the inverse of the inter-spike time interval.

The global frequency resulting from a simulation is defined as the mean of all instantaneous frequencies. For simulations with zero or only a single spike, instantaneous frequencies cannot be computed; in these cases, the frequency is set to 0.

10.5.4 Pattern distinction

Five distinct firing patterns are identified: "No Spike", "Single Spike", "Two spikes"[1], "Transient", and "Spiking". The first three patterns are categorized strictly by total spike count: corresponding to zero, one, or two spikes, respectively. "Spiking" denotes sustained firing throughout the stimulus; this is determined by checking whether the final detected spike falls within the time interval of the last calculated instantaneous frequency[2] right before stimulus termination. Finally, "Transient" encompasses any response that does not meet the criteria for the other categories.

[1] The "two-spike" response is in fact a subtype of transient pattern and is grouped with transient responses in transient-only plots.

[2] In the implementation, this value is multiplied by 1.2 to increase tolerance

Utilization of AI

Report Writing: Gemini was used to rephrase and refine the text, as well as to assist in finding specific LaTeX packages.

Implementation in Julia: Gemini helped identify relevant Julia packages, functions, and their official documentation.

References

[1] Eric R. Kandel et al., eds. *Principles of neural science*. Sixth edition. New York: McGraw Hill, 2021. 1646 pp.

[2] Fernanda C Cardoso and Richard J Lewis. "Sodium channels and pain: from toxins to therapies". In: *British Journal of Pharmacology* 175.12 (June 2018), pp. 2138–2157. doi: 10.1111/bph.13962.

[3] Frank H Yu and William A Catterall. "Overview of the voltage-gated sodium channel family". In: *Genome Biology* (2003).

[4] A. L. Hodgkin and A. F. Huxley. "A quantitative description of membrane current and its application to conduction and excitation in nerve". In: *The Journal of Physiology* 117.4 (Aug. 28, 1952), pp. 500–544. doi: 10.1113/jphysiol.1952.sp004764.

[5] Guillaume Drion. *Principles of neuroengineering (GNEU0001-1), University of Liège*. 2025.

[6] Clifford J. Woolf. "What is this thing called pain?" In: *Journal of Clinical Investigation* 120.11 (Nov. 1, 2010), pp. 3742–3744. doi: 10.1172/JCI45178.

[7] Stéphanie Ratté and Steven A Prescott. "Afferent hyperexcitability in neuropathic pain and the inconvenient truth about its degeneracy". In: *Current Opinion in Neurobiology* 36 (Feb. 2016), pp. 31–37. doi: 10.1016/j.conb.2015.08.007.

[8] Gary J. Bennett. "What Is Spontaneous Pain and Who Has It?" In: *The Journal of Pain* 13.10 (Oct. 2012), pp. 921–929. doi: 10.1016/j.jpain.2012.05.008.

[9] Shuang Liu and Leigh Kelliher. "Physiology of pain—a narrative review on the pain pathway and its application in the pain management". In: *Digestive Medicine Research* 5 (Dec. 2022), pp. 56–56. doi: 10.21037/dmr-21-100.

[10] R. Jason Yong et al., eds. *Pain Medicine: An Essential Review*. Cham: Springer International Publishing, 2017. doi: 10.1007/978-3-319-43133-8.

[11] Clifford J. Woolf. "Pain amplification—A perspective on the how, why, when, and where of central sensitization". In: *Journal of Applied Biobehavioral Research* 23.2 (June 2018), e12124. doi: 10.1111/jabr.12124.

[12] Clifford J. Woolf. "Central sensitization: Implications for the diagnosis and treatment of pain". In: *Pain* 152.3 (Mar. 2011), S2–S15. doi: 10.1016/j.pain.2010.09.030.

[13] Alban Latremoliere and Clifford J. Woolf. "Central Sensitization: A Generator of Pain Hypersensitivity by Central Neural Plasticity". In: *The Journal of Pain* 10.9 (Sept. 2009), pp. 895–926. doi: 10.1016/j.jpain.2009.06.012.

[14] Stephen G Waxman and Gerald W Zamponi. "Regulating excitability of peripheral afferents: emerging ion channel targets". In: *Nature Neuroscience* 17.2 (Feb. 2014), pp. 153–163. doi: 10.1038/nn.3602.

[15] Adélaïde Le Franc, Alexandre Da Silva, and Sinda Lepetre-Mouelhi. "Nanomedicine and voltage-gated sodium channel blockers in pain management: a game changer or a lost cause?" In: *Drug Delivery and Translational Research* 14.8 (Aug. 2024), pp. 2112–2145. doi: 10.1007/s13346-024-01615-9.

[16] Rabia Bouali-Benazzouz et al. “Neuropathic pain modeling: Focus on synaptic and ion channel mechanisms”. In: *Progress in Neurobiology* 201 (June 2021), p. 102030. doi: 10.1016/j.pneurobio.2021.102030.

[17] Renee Siu Yu Ma et al. “Voltage gated sodium channels as therapeutic targets for chronic pain”. In: *Journal of Pain Research* Volume 12 (Sept. 2019), pp. 2709–2722. doi: 10.2147/JPR.S207610.

[18] Anthony M. Rush, Theodore R. Cummins, and Stephen G. Waxman. “Multiple sodium channels and their roles in electrogenesis within dorsal root ganglion neurons”. In: *The Journal of Physiology* 579.1 (Feb. 15, 2007), pp. 1–14. doi: 10.1113/jphysiol.2006.121483.

[19] Andrei B. Petrenko et al. “The Role of N-Methyl-d-Aspartate (NMDA) Receptors in Pain: A Review:” in: *Anesthesia & Analgesia* (Oct. 2003), pp. 1108–1116. doi: 10.1213/01.ANE.0000081061.12235.55.

[20] Elif Karabacak. “Why are NMDA Receptors and Ligands Important in Treating Neuropathic Pain?” In: *Akdeniz Medical Journal* 12.1 (May 6, 2026). doi: 10.53394/akd.1568440.

[21] Xi-Yue Li et al. “NMDA Receptors in Neuropathic Pain: From Mechanisms to Therapeutic Strategies”. In: (2026).

[22] P. Aguiar, M. Sousa, and D. Lima. “NMDA Channels Together With L-Type Calcium Currents and Calcium-Activated Nonspecific Cationic Currents Are Sufficient to Generate Windup in WDR Neurons”. In: *Journal of Neurophysiology* 104.2 (Aug. 2010), pp. 1155–1166. doi: 10.1152/jn.00834.2009.

[23] Jean-Marc Goaillard and Martial A Dufour. “The pros and cons of degeneracy”. In: *eLife* 3 (Apr. 1, 2014), e02615. doi: 10.7554/eLife.02615.

[24] Jean-Marc Goaillard and Eve Marder. “Ion Channel Degeneracy, Variability, and Covariation in Neuron and Circuit Resilience”. In: *Annual Review of Neuroscience* 44.1 (July 8, 2021), pp. 335–357. doi: 10.1146/annurev-neuro-092920-121538.

[25] Mohammad Amin Kamaleddin. “Degeneracy in the nervous system: from neuronal excitability to neural coding”. In: *BioEssays* 44.1 (Jan. 2022), p. 2100148. doi: 10.1002/bies.202100148.

[26] Stéphanie Ratté et al. “Criticality and degeneracy in injury-induced changes in primary afferent excitability and the implications for neuropathic pain”. In: *eLife* 3 (Apr. 1, 2014), e02370. doi: 10.7554/eLife.02370.

[27] Yu-Feng Xie et al. *Equivalent excitability through different sodium channels and implications for the analgesic efficacy of selective drugs*. Apr. 8, 2024. doi: 10.7554/eLife.90960.2.

[28] Xi Yang et al. “A review of the mechanism of the central analgesic effect of lidocaine”. In: *Medicine* 99.17 (Apr. 2020), e19898. doi: 10.1097/MD.0000000000019898.

[29] Kanupriya Kumar et al. “A Review of Opioid-Sparing Modalities in Perioperative Pain Management: Methods to Decrease Opioid Use Postoperatively”. In: *Anesthesia & Analgesia* 125.5 (Nov. 2017), pp. 1749–1760. doi: 10.1213/ANE.0000000000002497.

[30] Michael E BrZiu, Werner Vogel, and Gunter Hempelmann. “Fundamental Properties of local Anesthetics: Half-Maximal Blocking Concentrations for Tonic Block of Na+ and K+ Channels in Peripheral Nerve”. In: (1998).

[31] Jean-Pierre Estebe. “Intravenous lidocaine”. In: *Best Practice & Research Clinical Anaesthesiology* 31.4 (Dec. 2017), pp. 513–521. doi: 10.1016/j.bpa.2017.05.005.

[32] Elizabeth C. Wick, Michael C. Grant, and Christopher L. Wu. “Postoperative Multimodal Analgesia Pain Management With Nonopioid Analgesics and Techniques: A Review”. In: *JAMA Surgery* 152.7 (July 1, 2017), p. 691. doi: 10.1001/jamasurg.2017.0898.

[33] Marion Voute, Véronique Morel, and Gisèle Pickering. "Topical Lidocaine for Chronic Pain Treatment". In: *Drug Design, Development and Therapy* Volume 15 (Sept. 2021), pp. 4091–4103. doi: 10.2147/DDDT.S328228.

[34] Vasanth Vedantham and Stephen C. Cannon. "The Position of the Fast-Inactivation Gate during Lidocaine Block of Voltage-gated Na+ Channels". In: *The Journal of General Physiology* 113.1 (Jan. 1, 1999), pp. 7–16. doi: 10.1085/jgp.113.1.7.

[35] P Chevrier, K Vijayaragavan, and M Chahine. "Differential modulation of Na_v 1.7 and Na_v 1.8 peripheral nerve sodium channels by the local anesthetic lidocaine". In: *British Journal of Pharmacology* 142.3 (June 2004), pp. 576–584. doi: 10.1038/sj.bjp.0705796.

[36] Patrick L. Sheets et al. "Differential Block of Sensory Neuronal Voltage-Gated Sodium Channels by Lacosamide [(2 R)-2-(Acetylamino)-N-benzyl-3-methoxypropanamide], Lidocaine, and Carbamazepine". In: *The Journal of Pharmacology and Experimental Therapeutics* 326.1 (July 2008), pp. 89–99. doi: 10.1124/jpet.107.133413.

[37] Patrick L Sheets, Brian W Jarecki, and Theodore R Cummins. "Lidocaine reduces the transition to slow inactivation in Na_v 1.7 voltage-gated sodium channels". In: *British Journal of Pharmacology* 164.2 (Sept. 2, 2011), pp. 719–730. doi: 10.1111/j.1476-5381.2011.01209.x.

[38] Andreas Leffler et al. "Use-Dependent Block by Lidocaine but Not Amitriptyline Is More Pronounced in Tetrodotoxin (TTX)-Resistant Nav1.8 Than in TTX-Sensitive Na+ Channels". In: *The Journal of Pharmacology and Experimental Therapeutics* 320.1 (Jan. 2007), pp. 354–364. doi: 10.1124/jpet.106.109025.

[39] Nobuyasu Nishizawa et al. "The Inhibition of the N-Methyl-D-Aspartate Receptor Channel by Local Anesthetics in Mouse CA1 Pyramidal Neurons". In: (2002).

[40] Masahiro Sugimoto, Ichiro Uchida, and Takashi Mashimo. "Local anaesthetics have different mechanisms and sites of action at the recombinant N-methyl-D-aspartate (NMDA) receptors". In: *British Journal of Pharmacology* 138.5 (Mar. 2003), pp. 876–882. doi: 10.1038/sj.bjp.0705107.

[41] Lianxi Zhang et al. "Different effects of local anesthetics on extracellular signal-regulated kinase phosphorylation in rat dorsal horn neurons". In: *European Journal of Pharmacology* 734 (July 2014), pp. 132–136. doi: 10.1016/j.ejphar.2014.03.048.

[42] Henning Hermanns et al. "Molecular mechanisms of action of systemic lidocaine in acute and chronic pain: a narrative review". In: *British Journal of Anaesthesia* 123.3 (Sept. 2019), pp. 335–349. doi: 10.1016/j.bja.2019.06.014.

[43] Miyuki Kurabe, Hidemasa Furue, and Tatsuro Kohno. "Intravenous administration of lidocaine directly acts on spinal dorsal horn and produces analgesic effect: An in vivo patch-clamp analysis". In: *Scientific Reports* 6.1 (May 18, 2016), p. 26253. doi: 10.1038/srep26253.

[44] Dmytro V. Vasylyev et al. "Dynamic-clamp analysis of wild-type human Na_v 1.7 and erythromelalgia mutant channel L858H". In: *Journal of Neurophysiology* 111.7 (Apr. 1, 2014), pp. 1429–1443. doi: 10.1152/jn.00763.2013.

[45] Chongyang Han et al. "Human Na_v 1.8: enhanced persistent and ramp currents contribute to distinct firing properties of human DRG neurons". In: *Journal of Neurophysiology* 113.9 (May 2015), pp. 3172–3185. doi: 10.1152/jn.00113.2015.

[46] Danielle Sundt, Nikita Gamper, and David B. Jaffe. "Spike propagation through the dorsal root ganglia in an unmyelinated sensory neuron: a modeling study". In: *Journal of Neurophysiology* 114.6 (Dec. 1, 2015), pp. 3140–3153. doi: 10.1152/jn.00226.2015.

[47] Anaëlle De Worm, Guillaume Drion, and Pierre Sacré. "Inward rectifier potassium channels interact with calcium channels to promote robust and physiological bistability". In: *PLOS Computational Biology* 22.7 (July 28, 2026). Ed. by Hermann Cuntz, e1014549. doi: 10.1371/journal.pcbi.1014549.

[48] Paul W Lenkowski et al. “Lidocaine block of neonatal Nav1.3 is differentially modulated by co-expression of β1 and β3 subunits”. In: *European Journal of Pharmacology* 467.1 (Apr. 2003), pp. 23–30. doi: 10.1016/S0014-2999(03)01595-4.